UNIVERSITY OF SOUTHAMPTON

Faculty of Engineering and Physical Sciences
School of Engineering

Organic and Inorganic Perovskite Solar Cells: Design, Fabrication and Performance Analysis

DOI: 10.1002/0470841559.ch1

Volume n of m

by

Selma Durak

MSc

ORCiD: 0000-0002-1010-7747

A thesis for the degree of
Doctor of Philosophy

November 2023

University of Southampton

Abstract

Faculty of Engineering and Physical Sciences
School of Engineering

Doctor of Philosophy

Organic and Inorganic Perovskite Solar Cells: Design, Fabrication and Performance Analysis

by Selma Durak

This project investigated organic and inorganic perovskite solar cells in terms of their design, fabrication, and photovoltaic performance using computational and experimental methods. Bismuth-based perovskites were theoretically explored by employing density functional theory through the Cambridge Serial Total Energy Package software. Perdew-Burke-Ernzerhof exchange-correlation functional for solids was employed to examine structural, electronic, and optical properties of Bi-based perovskites. The crystal structure of Bi-based perovskites was simulated using Jmol and VESTA. Electronic density of states, joint density of states and absorption coefficients were performed using OptaDOS.

Additionally, Bi-based perovskite solar cells were fabricated to analyse their photovoltaic performance. The precursor materials were produced using the wet-chemical synthesis method. Diffuse reflectance and transmittance spectroscopy were used to obtain spectral properties of Bi-based perovskites. The energy band gaps of the perovskites were estimated using Tauc plots with the Kubelka-Munk function. The layers of Bi-based perovskite solar cells were structured using spin-coating and sputter-coating methods.

Furthermore, degradation and recovery investigations were conducted using lead-based perovskites with titanate nanotubes. The ion-exchange method was utilised for producing lead titanate nanotubes. Pb-based perovskite solar cells with titanate nanotubes were fabricated using the doctor-blading method. Diffuse reflectance and Fourier-transform infrared spectroscopy were used to show the influence of methanamine hydroiodide treatment on degraded perovskites.

First principles density functional theory calculations showed that the crystal structure of Bi-based perovskites, which were $Cs_3Bi_2I_9$, $Cs_3Bi_2Br_9$ and $Cs_3Bi_2Br_3I_6$, crystallised in the hexagonal space group. The electronic band structure of $Cs_3Bi_2I_9$ estimated 1.99 eV of $Cs_3Bi_2I_9$ band gap energy, which was compatible with 2.00 eV band gap energy from Tauc plots. The energy band gap of $Cs_3Bi_2Br_9$ was determined

as 2.42 eV and 2.68 eV from the computational and experimental studies, respectively.

The current density-voltage characteristics of the $Cs_3Bi_2Br_xI_{9-x}$ solar cells demonstrated that the perovskite solar cell with $Cs_3Bi_2Br_3I_6$ achieved the highest PCE of 0.067% compared to the other Bi-based cells. The degradation and recovery study revealed that methanamine hydroiodide treatment significantly restored the diffuse absorbance response of $MAPbI_3$/Tint and the current density-voltage characteristics of the $MAPbI_3$/Tint solar cells.

Contents

List of Figures vii

List of Tables xi

Declaration of Authorship xiii

Acknowledgements xv

Definitions and Abbreviations xix

1 Introduction 1
- 1.1 Introduction . . . 1
  - 1.1.1 Issues with Perovskites . . . 3
  - 1.1.2 Aim and Objectives . . . 4
- 1.2 Perovskite Solar Cells . . . 4
- 1.3 Density Functional Theory . . . 6
- 1.4 Fundamentals of Solar Cells . . . 7
  - 1.4.1 Nature of Solar Radiation . . . 7
  - 1.4.2 Fundamentals of Semiconductors . . . 9
    - 1.4.2.1 Energy Bands . . . 9
    - 1.4.2.2 Semiconductors under Illumination . . . 9
    - 1.4.2.3 Doping in Semiconductors . . . 12
    - 1.4.2.4 Current-Voltage Characteristics of Solar Cells . . . 14
  - 1.4.3 Charge Carrier Statistics . . . 17
    - 1.4.3.1 Density of Carriers . . . 17
    - 1.4.3.2 Chemical Potential . . . 19
    - 1.4.3.3 Mass Action Law . . . 20
  - 1.4.4 Carrier Transport, Generation and Recombination . . . 22
    - 1.4.4.1 Carrier Transport . . . 22
    - 1.4.4.2 Carrier Generation . . . 23
    - 1.4.4.3 Carrier Recombination . . . 26

2 Literature Review 29
- 2.1 Architecture of Perovskite Solar Cells . . . 29
  - 2.1.1 Electron Transport Layer . . . 30
  - 2.1.2 Hole Transport Layer . . . 31
- 2.2 Preparation Methods of Perovskite Solar Cells . . . 32
- 2.3 Perovskites with Varied Chemical Structure . . . 33

2.3.1 Dual Metal Perovskites . . . 33
2.3.2 Mixed Perovskites . . . 36
2.4 Perovskite Studies with DFT . . . 40
2.5 Degradation Issue of Perovskite Solar Cells . . . 42

3 Methodology **45**
3.1 The First-principle Calculations for $\mathbf{Cs_3Bi_2I_9}$ and $\mathbf{Cs_3Bi_2Br_9}$ . . . 45
3.2 Production of $\mathbf{Cs_3Bi_2Br_xI_{9-x}}$ Solar Cells . . . 45
3.2.1 Synthesis of the bi-based perovskites . . . 46
3.2.2 Synthesis of the ETM . . . 47
3.2.3 Synthesis of the HTM . . . 50
3.2.4 Production of the Bi-based perovskite solar cells . . . 51
3.3 Production of $\mathbf{MAPbI_3/Tint}$ Solar Cells . . . 54
3.3.1 Preparation of the lead-based perovskites . . . 54
3.3.2 Production of the lead-based perovskite solar cells . . . 57
3.4 Characterisation of the Perovskite Solar Cells . . . 57

4 First Principle Calculations on Structural, Electronic and Optical Properties of $\mathbf{Cs_3Bi_2X_9}$ (X=Br,I) **59**
4.1 Crystal Structure . . . 60
4.2 Electronic Structure . . . 61
4.3 Optical Properties . . . 61
4.4 Discussion . . . 62
4.5 Conclusion . . . 63

5 Photovoltaic Characteristics of $\mathbf{Cs_3Bi_2Br_xI_{9-x}}$ Perovskite Solar Cells **71**
5.1 Spectral Response . . . 72
5.2 Current Density-Voltage Characteristics . . . 75
5.3 Discussion . . . 77
5.4 Conclusion . . . 78

6 Degradation Study of $\mathbf{MAPbI_3/Tint}$ Perovskite Solar Cells **79**
6.1 Spectral Response . . . 80
6.2 Current Density-Voltage Characteristics . . . 85
6.2.1 $\mathbf{MAPbI_3/Tint}$ Perovskite Solar Cells . . . 85
6.2.2 $\mathbf{PbI_2/Tint}$ Solar Cells . . . 89
6.3 Discussion . . . 91
6.4 Conclusion . . . 92

7 Conclusion **93**
7.1 Publication Plan . . . 94
7.2 Future Work . . . 95

References **97**

List of Figures

1.1 ABX_3 perovskite structure [29]. 5
1.2 Perovskite cell structure [32]. 5
1.3 a) Solar radiation in the atmosphere b) Air mass 8
1.4 Schematic energy band diagram of a) conductors, b) semiconductors, and c) insulators 9
1.5 Creation of electron-hole pairs in semiconductors under illumination by following the process of (a) light absorption, (b) thermalisation and (c) creation of the pairs 10
1.6 The crystal structure of diamond 12
1.7 Schematic diagram of silicon a) with a group five impurity b) with a group three impurity 13
1.8 Schematic diagrams of a) combination of p-type and n-type semiconductors b) construction of depletion region c) band structure of p-n junction d) band structure of p-n junction under applied voltage 14
1.9 I-V characteristics of diodes in dark (black) and under illumination (red) 15
1.10 I-V curve and corresponding power characteristic of typical solar cells . 16
1.11 Energy band diagram of p-n junction in equilibrium (left hand-side) and under excitation (right hand-side) 21
1.12 Schematic diagram of energy-momentum relationship in a) direct-band-gap b) indirect-band-gap semiconductors 25
1.13 Schematic diagram of a) radiative recombination b) Auger recombination c) defect-assisted (SHR) recombination d) Surface recombination . . 26

2.1 Schematics of architectures of perovskite solar cells in n-i-p and p-i-n configurations [57]. 29
2.2 a) XRD patterns and b) XPS spectra of $CH_3NH_3Sn_xPb_{(1-x)}I_3$ coated on porous TiO_2 [75]. 34
2.3 Energy diagrams of $CH_3NH_3Sn_xPb_{(1-x)}I_3$, titania, P3HT, spiro-OMeTAD [75]. 34
2.4 Conductivity, Seebeck coefficients, energy band gap and resistivity figures of $CH_3NH_3Sn_{1-x}Pb_xI_3$ solid solutions [76]. 35
2.5 Photocurrent density-voltage characteristics and corresponding IPCE spectra for $CH_3NH_3Sn_{1-x}Pb_xI_3$ solar cells [76]. 36
2.6 a) PCE values for $(FAPbI_3)_{1-x}(MAPbBr_3)_x$ perovskite devices annealed at 100 ^{o}C for 10 min and b) DSC and thermogravimetric curves of yellow $FAPbI_3$ [77]. 37

2.7 a) Current-voltage curves of TiO_2 and SnO_2-based mixed perovskite solar cells measured from backward (black) and forward (red) scan b) Normalised transient photocurrents obtained from V_{oc} to the maximum power point voltage for both cells c) Scan rate characteristics of the SnO_2 and d) TiO_2-based cells [78]. 38
2.8 A) Power conversion efficiencies as a function of different iodide concentrations B) J-V curves for the control and target devices [79]. 39
2.9 A) Deep-level transient spectroscopy spectra for the control and target perovskite layers B) Time-resolved photoluminescence decay curves for the control and target layers emitted at $\lambda = 825\ nm$ with the biexponential fitting [79]. 40

3.1 The solutions of $Cs_3Bi_2I_9$, $Cs_3Bi_2Br_9$, BiI_3 and $BiBr_3$ at 20 mmol/L and 10 mmol/L concentrations. 46
3.2 The images of $Cs_3Bi_2Br_xI_{9-x}$ solutions in order of x changing from 1 (the darkest red bottle) to 8 (the lightest yellow bottle). 47
3.3 Microscope images of c-TiO_2 from recipe-1 (a) and recipe-2 (b) on ITO-glass substrates 48
3.4 Microscope images of the two-layers c-TiO_2 from recipe-1 (a), from recipe-2 (c), and the three-layers c-TiO_2 from recipe-1 (b), from recipe-2 (d) . . . 49
3.5 Microscope images of the spiro-MeOTAD layer produced using 2000 rpm (a), 3000 rpm (b), 4000 rpm (c), and 4000 rpm heated at 120 ^{o}C (d). . 50
3.6 Microscope images of the spiro-MeOTAD edges cleaned with a cotton bud (a) and taped (b). 51
3.7 Schematic diagram of pre-patterned ITO-glass substrates 52
3.8 Microscope images of perovskite layers from the solutions of a) $Cs_3Bi_2Br_9$ at room temperature, b) $Cs_3Bi_2Br_9$ at 70 ^{o}C, c) $Cs_3Bi_2I_9$ at room temperature, d) $Cs_3Bi_2I_9$ at 70 ^{o}C. 53
3.9 Microscope images of perovskite layers coated with a) $Cs_3Bi_2Br_9$ solution at 70 ^{o}C, b) $Cs_3Bi_2I_9$ solution at 70 ^{o}C. The ITO-glass substrates were heated at 120 ^{o}C before coating. 54
3.10 Left-hand side image shows the bi-based perovskite solar cells produced using $Cs_3Bi_2I_9$ (orange) and $Cs_3Bi_2Br_9$ (yellow), while the right-hand side image shows the schematic diagram of the solar cells. 55
3.11 Images of the precursor powders produced using different molar ratios between Pb^{2+} and Tint, where Pb/Tint powders (left top image), PbI_2/Tint (right top image) and $MAPbI_3$/Tint (bottom image) 56
3.12 Images of a $MAPbI_3$/Tint perovskite solar cell from ITO-glass side (left) and schematic diagram (right). 57

4.1 Crystal structure of $Cs_3Bi_2I_9$ simulated by Jmol (top) and VESTA (bottom). In the unit cell from Jmol, Cs, Bi and I are shown in violet, purple and magenta, respectively. In the unit cell from VESTA, Cs, Bi and I are represented in blue, red, and yellow, respectively. Cell parameters of the unit cell are given at the top left corner of the figure. 64

4.2 Crystal structure of $Cs_3Bi_2Br_9$ obtained by Jmol (top) and VESTA (bottom). Cs, Bi and Br atoms are presented in violet, purple and red, respectively, in the unit cell from Jmol. Additionally, in the crystal structure obtained from VESTA, Cs, Bi and Br atoms are presented in blue, red, and green, respectively. Cell parameters are given at the left corner of the figure. 65
4.3 Crystal structure of $Cs_3Bi_2Br_3I_6$ obtained by Jmol (top) and VESTA (bottom). Cs, Bi, Br and I atoms are presented in violet, purple, red and magenta, respectively, in the unit cell from Jmol, whereas Cs, Bi, Br and I atoms are presented in blue, red, green and yellow, respectively, in the unit cell from VESTA. Cell parameters are given at the left corner of the figure. 66
4.4 Calculated electronic band structure (a) and density of states (b) of $Cs_3Bi_2I_9$. Dashed lines represent Fermi energy level, which was set to zero. 67
4.5 Calculated electronic band structure (a) and density of states (b) of $Cs_3Bi_2Br_9$. Dashed lines represent Fermi energy level, which was set to zero. 67
4.6 Calculated electronic band structure (a) and density of states (b) of $Cs_3Bi_2Br_3I_6$. Dashed lines represent Fermi energy level, which were set to zero. . . . 68
4.7 (a) Electronic density of states and (b) joint density of states of $Cs_3Bi_2I_9$, which were calculated using OptaDOS. 68
4.8 (a) Electronic density of states and (b) joint density of states of $Cs_3Bi_2Br_9$, which were calculated using OptaDOS. 68
4.9 (a) Electronic density of states and (b) joint density of states of $Cs_3Bi_2Br_3I_6$, which were calculated using OptaDOS. 69
4.10 Calculated absorption coefficients of (a) $Cs_3Bi_2I_9$ and (b) $Cs_3Bi_2Br_9$, which are obtained by OptaDOS. 69
4.11 Calculated absorption coefficients of $Cs_3Bi_2Br_3I_6$ obtained by OptaDOS. 69

5.1 (a) Absorption spectra of the precursor solutions of $Cs_3Bi_2I_9$, $Cs_3Bi_2Br_9$, $BiBr_3$ and BiI_3 obtained from transmittance spectroscopy. (b) Absorption spectra of perovskite thin films from DRS and transmittance spectroscopy. 72
5.2 Tauc plots of (a) $Cs_3Bi_2I_9$ and (b) $Cs_3Bi_2Br_9$ using Kubelka-Munk function. 73
5.3 Absorbance spectra of (a) $Cs_3Bi_2I_9$ and (b) $Cs_3Bi_2Br_9$ with different layers 73
5.4 Absorbance spectra of $Cs_3Bi_2Br_xI_{9-x}$ where x varies from 0 to 9. 74
5.5 Tauc plots of $Cs_3Bi_2Br_xI_{9-x}$ where x is varying from 0 to 9. 74
5.6 J-V characteristic of $Cs_3Bi_2I_9$ perovskite solar cells prepared using c-TiO_2 with recipe 1 and recipe 2. 76
5.7 J-V curves of $Cs_3Bi_2Br_xI_{9-x}$ perovskite solar cells. 77

6.1 Absorption spectra of (a) Tint and Pb/Tint, (b) PbI_2/Tint, and (c) $MAPbI_3$/Tint. 81
6.2 (a) Absorption spectra of Tint, (1) Pb/Tint, (1) PbI_2/Tint and (1) $MAPbI_3$/Tint, (b) Tauc plot of (1) $MAPbI_3$/Tint. 82
6.3 Absorption spectra of fresh-, old-, degraded-, treated-(1) $MAPbI_3$/Tint. . 82
6.4 FTIR spectra of (a) Tint and Pb/Tint, and (b) PbI_2/Tint. 83
6.5 FTIR spectra of (a) $MAPbI_3$/Tint, and (b) MAI. 83
6.6 FTIR spectra of (a) Tint, (1) Pb/Tint, (1) PbI_2/Tint and (1) $MAPbI_3$/Tint, and (b) fresh-(1) $MAPbI_3$/Tint in addition to its degraded and treated versions. 84

6.7 J-V characteristics of the perovskite solar cell with (1) $MAPbI_3$/Tint. . . 85
6.8 J-V characteristics of the perovskite solar cells with (a) (1) $MAPbI_3$/Tint and (b) (3) $MAPbI_3$/Tint measured at several minutely intervals under illumination. 86
6.9 J-V characteristics of (1) $MAPbI_3$/Tint perovskite solar cells (a) in the absence and (b) in the presence of *c*-TiO_2 layer. 86
6.10 J-V characteristics of the perovskite solar cells with (a) D-(1) $MAPbI_3$/Tint and (b) T-(1) $MAPbI_3$/Tint. 87
6.11 J-V characteristics of the D-(1) $MAPbI_3$/Tint solar cell exposed to higher voltage. 88
6.12 J-V characteristics of the (1) $MAPbI_3$/Tint solar cells with (a) Cu and (b) Ni as the counter electrode. 88
6.13 J-V characteristics of (1) PbI_2/Tint solar cells (a) immediately measured after the preparation and (b) hourly measured under illumination. . . . 89
6.14 J-V characteristics of the solar cells with (a) degraded-(1) PbI_2/Tint and (b) treated-(1) PbI_2/Tint. 90
6.15 J-V characteristics of the degraded-(1) PbI_2/Tint solar cell exposed to higher voltage. 90

List of Tables

3.1 The amounts of the components to produce Bi-halide salts and $Cs_3Bi_2Br_xI_{9-x}$ perovskites in DMF. 47
3.2 The amounts for preparing ETMs with two different recipes. 48

5.1 Energy band gaps of $Cs_3Bi_2Br_xI_{9-x}$ perovskites from Tauc plots 75
5.2 J-V characteristics of $Cs_3Bi_2Br_xI_{9-x}$ perovskite solar cells 76

Declaration of Authorship

I declare that this thesis and the work presented in it is my own and has been generated by me as the result of my own original research.

I confirm that:

1. This work was done wholly or mainly while in candidature for a research degree at this University;
2. Where any part of this thesis has previously been submitted for a degree or any other qualification at this University or any other institution, this has been clearly stated;
3. Where I have consulted the published work of others, this is always clearly attributed;
4. Where I have quoted from the work of others, the source is always given. With the exception of such quotations, this thesis is entirely my own work;
5. I have acknowledged all main sources of help;
6. Where the thesis is based on work done by myself jointly with others, I have made clear exactly what was done by others and what I have contributed myself;
7. Parts of this work have been published as:

Signed:..... Date:.....

Acknowledgements

I want to state my deepest gratitude to my supervisor Assoc. Prof. Dr Dmitry Bavykin for giving me excellent support to complete this thesis. I am thankful for his precious guidance, extraordinary contributions, innovative recommendations, vital support, and endless patience throughout this study. I thank Prof. Tom Markvart for his valuable help as my second supervisor. Thanks to both, I have gained precious academic experience under their supervision.

I thank my precious, wonderful, and lovely family consisting of my father (Ömer), my mother (Fatma), my sisters (Merve and Esra), and my brothers (Ahmet and Süleyman). I am grateful to each of them for their paramount support and infinite love.

I am grateful to the Ministry of Education of the Republic of Turkey for its financial support throughout my PhD study.

To . . .

Definitions and Abbreviations

α	Absorption coefficient
ε	Electric field
η	Efficiency
κ	Octahedral factor
λ	Wavelength
μ	Chemical potential
μ_e	Chemical potential on n-side
μ_h	Chemical potential on p-side
ν	Frequency of radiation
ρ	Resistivity
σ	Conductivity
ϕ	Spectral photon flux density
Φ	Photon flux density
τ	Minority-carrier lifetime
φ	Electrostatic potential
ϱ	Momentum of photon
ϑ_n	Electron mobility
ϑ_p	Hole mobility
A	Area
c	Speed of light in vacuum
D	Proportionality constant
D_n	Diffusion coefficient of electrons
D_p	Diffusion coefficient of holes
e_E	Spectral irradiance
E	Energy
E_c	Lowest energy level of conduction band
$E_c(r)$	Position-dependent energy of conduction band edge
E_g	Energy band gap
E_t	Defect energy
E_v	Highest energy level of valence band
$E_v(r)$	Position-dependent energy of valence band edge
f	Probability of occupation

g	Generation rate
G	Irradiance
h	Plancks constant
I	Current
I_0	Current at thermal equilibrium
I_l	Photogenerated current
I_{mp}	Maximum current
I_{sc}	Short circuit current
j	Diffusion current density
J	Current density
J_d	Drift current density
J_n	Diffusion current density of electrons
J_p	Diffusion current density of holes
J_s	Recombination current density
J_{tn}	Total electrical current density
J_{tp}	Total hole current density
$J-V$	Current density-voltage
k_B	Boltzmann constant
l_n	Drift length of electron
l_p	Drift length of hole
m	Mass of electron
m_e^*	Effective mass of electrons
m_p^*	Effective mass of holes
n	Electron density
n_0	Electron concentration in thermal equilibrium
n_i	Electron and hole concentration in intrinsic semiconductor
N	Density of states
N_c	Density of states in conduction band
$N_c(T)$	Effective density of states in conduction band
N_v	Density of states in valence band
$N_v(T)$	Effective density of states in valence band
p	Hole density
p_0	Hole concentration in thermal equilibrium
P	Power
P_{max}	Maximum power
r_{rad}	Radiative recombination rate
r_{SHR}	Defect recombination rate
r_{surf}	Surface recombination function
R	Reflection coefficient
R_A	Ionic radius of cation A
R_B	Ionic radius of cation B

R_s	Series resistant
R_sh	Shunt resistant
S	Surface recombination velocity
q	Electron charge
Q_E	External quantum efficiency
t	Goldschmidt tolerance factor
T	Absolute temperature
V	Voltage
V_{mp}	Maximum voltage
V_{oc}	Open circuit voltage
ALD	Atomic layer deposition
AM	Air mass
$AM1.5G$	Air mass 1.5 global
AVA	Aminovaleric acid
$CASTEP$	Cambridge serial total energy package
CB	Conduction band
CBM	Conduction band minimum
$c-TiO_2$	Compact-TiO_2
CuI	Copper (I) iodide
$CuSCN$	Copper (I) thiocyanate
DFT	Density functional theory
$DLTS$	Deep-level transient spectroscopy
DMF	N,n-dimethylformamide
$DMSO$	Dimethyl sulfoxide
DRS	Diffuse reflectance spectroscopy
DSC	Differential scanning calorimetry
EDS	Energy-dispersive x-ray spectroscopy
$EELS$	Electron-energy loss spectra
EQE	External quantum efficiency
ESL	Electron selective layer
ETL	Electron transport layer
ETM	Electron transport material
FF	Fill factor
$FTIR$	Fourier-transform infrared
FTO	Fluorine-doped tin oxide
GBL	γ-butyrolactone
GGA	Generalised gradient approximation
$GIWAXS$	Glazing-incidence wide-angle x-ray scattering
HI	Hydroiodic acid
HSE	Heyd-Scuseria-Ernzerhof
HTL	Hole transport layer

HTM	Hole transport material
INS	Inelastic neutron scattering
$IPCE$	Incident photon to current efficiency
IR	Infrared
ITO	Indium tin oxide
LDA	Local density approximation
MA	Methylammonium
$MACl$	Methanamine hydrochloride
MAI	Methanamine hydroiodide
MP	Monkhurst-pack
NMP	N-methyl-2-pyrrolidone
NMR	Nuclear magnetic resonance
$P3HT$	Poly-3-hexylthiophene
PAW	Projector augmented-wave
PB	Photobleach
PBE	Perdew, Becke and Ernzerhof
$PBESOL$	Perdew-Burke-Ernzerhof formalism for solids
$PCDTBT$	Poly-[[9-(1-octylnonyl)-9H-carbazole-2,7-diyl]-2,5-thiophenediyl-2,1, 3-benzothiadiazole-4,7-diyl-2,5-thioph- enediyl]
PCE	Power conversion efficiency
$PCPDTBT$	Poly-[2,1,3-benzothiadiazole-4,7-diyl[4,4-bis(2-ethylhexyl)-4H-cyclopenta [2,1-b:3,4-$b^{'}$]dithiophene-2,6-diyl]]
$PDOS$	Partial density of states
$PEDOT:PSS$	Poly(3,4-ethylenedioxythiophene) polystyrene sulphonate
$PEIE$	Polyethyleneimine ethoxylated
PET	Poly-(ethylene terephthalate)
PL	Photoluminescence
PSC	Perovskite solar cell
$PTAA$	Poly-triarylamine
PV	Photovoltaic
SEM	Scanning electron microscopy
SOC	Spin-orbital coupling
$spiro-MeOTAD$	$2^{'}$,7,$7^{'}$-tetrakis(N,N-pdimethoxyphenylamino)-9,$9^{'}$-spirobifluorene
TA	Femtosecond transient absorption
$Tint$	Titanate nanotubes
UPS	Ultraviolet photo-electron spectroscopy
$UV-vis$	Ultraviolet-visible
$VASP$	Vienna Ab initio simulation package
VB	Valence band
VBM	Valance band maximum
$VESTA$	Visualisation for electronic and structural analysis

XC	Exchange-correlation
XRD	X-ray diffaction
XPS	X-ray photoelectron spectroscopy
$Y - TiO_2$	Yttrium-doped TiO_2

Chapter 1

Introduction

1.1 Introduction

The production of electrical energy is a crucial issue because the energy demand is significantly increasing due to technological improvements. The energy sources to fulfil the demand can be separated into three groups, which are fossil fuels, nuclear energy, and renewable energy [1]. In 2020, the global energy demand was mainly fulfilled by conventional methods, which were oil at 33.6%, coal at 27.2%, natural gas at 23.9% and nuclear at 4.4%, whereas renewable energy provided 10.8% of energy need [2]. However, the usage of fossil fuels has raised concerns about their environmental damage because they cause an increase in the CO_2 amount in the atmosphere by emitting the carbon absorbed millions of years ago [3]. Therefore, renewable energy sources have gained great interest as they provide not only clean and sustainable energy [4].

Renewable energy sources consist of solar, wind, hydro, geothermal, ocean thermal energy conversion and biomass [5]. The energy generation by renewable sources is considerably provided by hydropower (44.4%), wind energy (25.26%) and solar energy (24.23%), while biomass and geothermal energy contribute 5.37% and 0.54% of electricity generation, respectively [6]. Among renewable energy sources, solar energy has zero greenhouse gas emissions to the atmosphere to produce electrical power [7]. Additionally, the increase in photovoltaic (PV) projects and research led to significant enhancement in solar PV device technology [8]. Therefore, PV solar cells offer lower cost and less energy-intensive fabrication processes along with the usage of abundant and economical material [9].

Especially, perovskite solar cells (PSCs) have gained considerable interest thanks to their cost-effective production techniques and the substantial increase in power conversion efficiency (PCE) in recent years. PSCs were introduced with a PCE of 3.8%

[10] in 2009; however, upon implementation of different chemical compounds and cell preparation techniques, their efficiency has already surpassed the value of 24% [11]; that is also a reason for the perovskite solar cells to have great interest. Additionally, the sensitivity of perovskites to moisture and temperature has been relatively overcome. Thus, PSCs have become suitable devices employed in electricity generation with the help of photovoltaic device technology.

PSCs are produced employing different fabrication techniques among which spin-coating is the most used solution deposition method [12]. This method limits the size of substrates and is applied on small-area devices ($<$1 cm^2); however, large-area ($>$100 cm^2) devices are needed for the commercialisation of PSCs [13]. Thus, scalable solution-based deposition methods have gained interest in fabricating PSCs, such as doctor blading, slot-die coating, spray coating, inkjet printing, screen printing and electrodeposition [14]. Additionally, crystalline silicon solar cells are widely used in the PV market due to their high module efficiency, availability, non-toxicity, and longevity, but they suffer from the theoretical efficiency limit of 29.56% [15]. Perovskite/silicon tandem solar cells are promising candidates to overcome the efficiency barrier to produce PV devices with higher PCE. For instance, a non-toxic perovskite/silicon-based solar cell achieved a PCE of 30.7% [16]. Therefore, perovskites can be used in module fabrication and thereby brought to the market [17].

Perovskite materials have a chemical formula of ABX_3 where A is a cation, B is a metal, and X is a halogen. The cation A fits into the space composed of four adjacent corner-sharing BX_6 octahedra. Besides, the ionic radii of A, B and X have been used for establishing the distortion of the BX_6 octahedron [18]. Detailed information about perovskite materials has been given in Section 1.2, while perovskite device architecture and PSC preparation methods have been described in Section 2.1 and Section 2.2, respectively. Besides, fundamental concepts of solar cells have been introduced in Section 1.4.

The perovskite devices have been fabricated using various perovskite chemical structures created by the changes in the parts of the ABX_3 structure. In the literature, some studies focus on the halogen, cation, or metal parts of the perovskite structure, which resulted in many perovskite materials being developed and introduced. Based on that, the information on two types of perovskite materials has been described and discussed in Section 2.3, highlighting dual-metal perovskites and mixed perovskites. Additionally, the properties of those hybrid perovskite solar cell studies and research findings have been presented and discussed.

Density functional theory (DFT) has been employed to conduct computational studies on perovskite materials. In this project, DFT has been used for numerical calculations, and results were visualised utilising Cambridge serial total energy package (CASTEP).

The fundamental concepts of DFT have been given in Section 1.3, while relevant studies on the perovskites with DFT have been presented in Section 2.4.

In this thesis, inorganic bi-based perovskites and organic-inorganic lead-based perovskites with titanate nanotubes (Tint) have been investigated in terms of photovoltaic characteristics and long-term stability. The inorganic $Cs_3Bi_2I_9$ and $Cs_3Bi_2Br_9$ perovskites have been examined to investigate the structural, electronic, and optical properties of the perovskites with the help of the CASTEP computer program code using first principles DFT calculations. The results of the computational study were revealed in Chapter 4.

Additionally, dual halogen bi-based perovskites with the chemical structure of $Cs_3Bi_2Br_xI_{9-x}$ have been investigated in terms of their spectral and photovoltaic properties in Chapter 5. The UV-vis spectra of the perovskites were examined, and their energy band gaps were estimated using Tauc plots.

Moreover, MAI treatment to recover degraded $MAPbI_3$ with titanate nanotubes ($MAPbI_3$/Tint) has been investigated in Chapter 6. The UV-vis spectra of precursors were examined, and the energy band gap of $MAPbI_3$/Tint was obtained using the Kubelka-Munk function. The current density-voltage (J-V) characteristics of $MAPbI_3$/Tint solar cells were investigated before and after degradation and MAI treatment.

1.1.1 Issues with Perovskites

Perovskites have gained considerable interest as absorbers of light in photovoltaic devices because of having favourable optical properties, such as tunable band gap, ambipolar charge carrier transport and long diffusion length of the charge carriers [19]. Additionally, a remarkable improvement in power conversion efficiency (PCE) of hybrid organic-inorganic metal halide perovskite solar cells has been achieved in the past decade, as the highest PCE value of the solar cells was recorded as 24.2% [20]. Nevertheless, perovskite solar cells are facing two key issues, which are the toxicity of lead (Pb) and long-term stability.

The long-term stability issue in perovskite solar cells stems from various structural and environmental challenges, such as small grain size, moisture, heat, light, and oxygen [21]. The stability issue can be solved by tuning the tolerance factor to enhance the stability of perovskite materials [22]. However, the Goldschmidt tolerance factor can only be used to determine the stability of perovskites having a chemical structure of ABX_3 [23].

As for the toxicity problem of lead-based perovskites, the homovalent substitution of lead with tin (Sn) and germanium (Ge) has been proposed. However, it was reported

that, Sn^{2+} and Ge^{2+} were easily oxidised into Sn^{4+} and Ge^{4+} in air, which is a stability problem [19]. On the other hand, the use of trivalent metal cation-based perovskites has provided non-toxic and stable materials for perovskite solar cell fabrication. For instance, the organic-inorganic bismuth-based perovskite film performed great stability for 40 days under humidity and ambient air at room temperature [24].

1.1.2 Aim and Objectives

Considering the advantages and limitations of perovskite solar cells, this project aims to produce perovskites with improved stability and to analyse perovskite solar cells using computational and empirical methods.

The main objectives of the study are:

(i) to investigate electronic and optical properties of low-toxic perovskite materials using theoretical simulations

(ii) to determine an efficient solution-based fabrication procedure to build the layers in the cell structure

(iii) to fabricate perovskite solar cells with improved stability by considering the necessary arrangements in the production of perovskite material and the solar cell architecture

(iv) to seek methodology to recover degraded solar cells.

1.2 Perovskite Solar Cells

Perovskite originates from calcium titanium oxide mineral with the formula of $CaTiO_3$, which was discovered by Gustav Rose in the Ural Mountains of Russia in 1839 [25]. It was named after Russian mineralogist Lev Perovski, who defined the ABX_3 chemical structure [26]. Thus, the chemicals with ABX_3 general chemical formula have been called perovskite.

In the ABX_3 structure, A and B are cations of varied sizes, while X is an anion [25]. The A cations can be selected as methylammonium (MA) ($CH_3NH_3^+$), formamidinium (FA) ($HC(NH_2)_2^+$), tetramethylammonium (TMA) ($(CH_3)_4N^+$), Cs^+, and Rb^+, whereas the smaller cation, B, is chosen as a metal such as Pb^{2+}, Sn^{2+}, Ge^{2+}, Cu^{2+}, Eu^{2+} and Co^{2+} [27]. On the other hand, the X is a halide ion such as I^-, Cl^-, Br^-, and F^- [28].

The crystal structure of the perovskites consists of corner-sharing BX_6 with A cation, which is shown as the three-dimensional framework in Figure 1.1 [29]. In the cubic

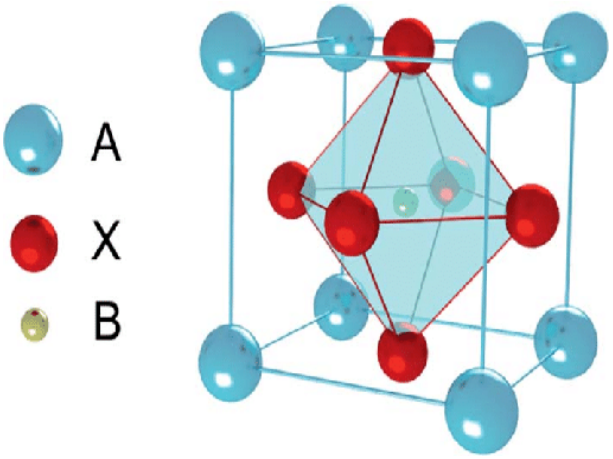

FIGURE 1.1: ABX_3 perovskite structure [29].

cell, A is located at the corners of the cube, while B is settled in the centre of the cubic cell and surrounded by the X anions. Apart from the cubic cell, various crystal structures are obtained by tilting and rotating of BX_6 polyhedral such as tetragonal, orthorhombic, rhombohedral, and hexagonal [30].

The typical perovskite solar cell consists of several layers, which contribute to determining the electronic and optical properties. Perovskite material is sandwiched between two charge carrier layers facilitating the movement of electrons and holes. These charge transport layers, namely the electron transport layer (ETL) and hole transport layer (HTL), are connected to two electrodes, which act as cathode and anode. The electrode, whose surface sunlight hits, can be selected as indium tin oxide (ITO) or fluorine-doped tin oxide (FTO), while the counter electrode can be chosen as Au, Ag or Al [31]. Figure 1.2 depicts a basic perovskite cell structure [32]. In the cell, compact-TiO_2 (c-TiO_2) material is used as the electron-selective layer.

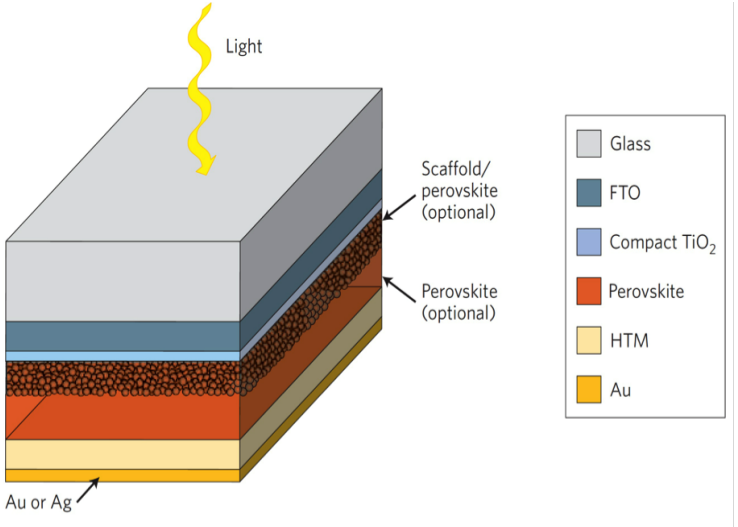

FIGURE 1.2: Perovskite cell structure [32].

1.3 Density Functional Theory

DFT has been applied in many different scientific fields such as condensed matter physics, solid-state chemistry, and materials science [33]. By defining the crystal structure of a material, band structure, the density of states, acoustic wave propagation and elastic constants, electron-energy loss spectra (EELS), nuclear magnetic resonance (NMR), infrared (IR), Raman and inelastic neutron scattering (INS) can be obtained [33]. To simulate these properties, CASTEP is an effective computer program to use, which is a first principles quantum mechanical code [34].

The behaviour of nuclei in an atom can be described by Born-Oppenheimer approximation as if it is a classical point-like particle, whereas the behaviour of electrons is defined by solving the Schrodinger equation [33]. For the one-electron systems, the solution of the equation is straightforward, yet it becomes a complex problem to solve when the electron number increases and the many-body Schrodinger equation is required to define the behaviour of the electrons [35]. Nevertheless, the difficulty of the solution of the many-body Schrodinger equation can be overcome when the density of electrons is considered by using DFT. The fundamental principle of DFT is that the total energy of a system, consisting of nuclei and electrons, is a unique functional of the electron density [33].

In the DFT problem, the ground state energy and particle density of a system with N-electron have converted a set of independent particle equations, Kohn-Sham equations [36]. These equations contain a modified effective potential, which is a functional of the total density and includes quantum-mechanical exchange and correlation of the particles [33]. The commonly used approximation for exchange-correlation (XC) is local density approximation (LDA), with which it is assumed that the XC energy density at a certain position depends only on the particle density at that point. On the other hand, generalised-gradient approximations (GGAs), including PW91 and Perdew, Becke and Ernzerhof (PBE) functionals, are based on a local density gradient. The other common approximations beyond the GGA are meta-GGA, in which the Laplacian of the density can be involved, hybrid functionals, in which an experimental fraction of Hartree-Fock exchange is contained, and DFT+U, in which an on-site Hubbard-U potential is considered [33].

After the exchange-correlation potential is determined, the basis for the single-particle wave functions is chosen. Bloch theorem is used to define the wave function of the periodic crystal system. Wave functions are represented by periodic Bloch functions multiplied by a complex phase factor. The wave vectors of the phase factor are defined in the first Brillouin zone in reciprocal space. Integrals over the Brillouin zone are calculated numerically using a discrete mesh of wave vectors called k-points. The Bloch functions are expressed by plane-wave basis sets controlled by a single parameter, namely cut-off energy [33].

In the core regions near the nuclei, singular electron-nuclei Coulomb interaction induces sharp peaks in the Kohn-Sham states because of the increase of the high wave vector. The Kohn-Sham states do not reflect the environmental impacts on the chemical and electronic properties of the material since Coulomb interactions dominate the potential in the core region. At that point, instead of Kohn-Sham states or the Coulomb potential, pseudo-potentials are utilised to reproduce atomic scattering properties and Coulombic form outside the core region [33].

1.4 Fundamentals of Solar Cells

1.4.1 Nature of Solar Radiation

Sunlight is an infinite energy source used to produce electricity utilising photovoltaic devices. In photovoltaic devices, the quantum nature of light is considered for energy conversion, and thereby light is considered as a stream of particles called photons [37]. The quantitative measurement of light is the wavelength. Light with a single wavelength is defined as monochromatic, while light involving different wavelengths is named spectrum.

Einstein's relation is used to express the energy of photons in Joules as the light is considered a flux of particles and given by [38]:

$$E = h\nu = \frac{hc}{\lambda} \tag{1.1}$$

where h is the Planck's constant (6.626×10^{-34} J.s), ν is the frequency of the radiation, c is the speed of light in vacuum (2.998×10^{8} m/s), and λ is the wavelength of monochromatic light. The energy of a photon in eV is defined by [39]:

$$E/q = \frac{(hc/q) \times 10^{6}}{\lambda \times 10^{6}} = \frac{1.24}{\lambda\ (in\ \mu m)} \tag{1.2}$$

where q is the electron charge (1.602×10^{-19} C).

A light beam is characterised by the area hit by light and the power from the sun. Therefore, the irradiance in W/m^2 is given by [40]:

$$G = \frac{Power}{Area} \tag{1.3}$$

The photon flux density in $s^{-1}.m^{-2}$ defined as the number of photons passing through an area perpendicular to the beam per second is given by [40]:

$$\Phi = \frac{G}{E} = \frac{Power/Area}{h\nu} \tag{1.4}$$

The formulation above is developed by considering monochromatic light, which is characterised by a single wavelength, frequency, and photon energy in a beam.

The irradiance out of the atmosphere is defined as the solar constant, S=1353 W/m^2, while the irradiance, which is the sharp radiation on the ground, is named standard irradiance, 1 kW/m^2. The difference between these two originates from the obstacles throughout the journey from extraterrestrial space to the ground like scattering or absorption of light by air molecules or clouds [41].

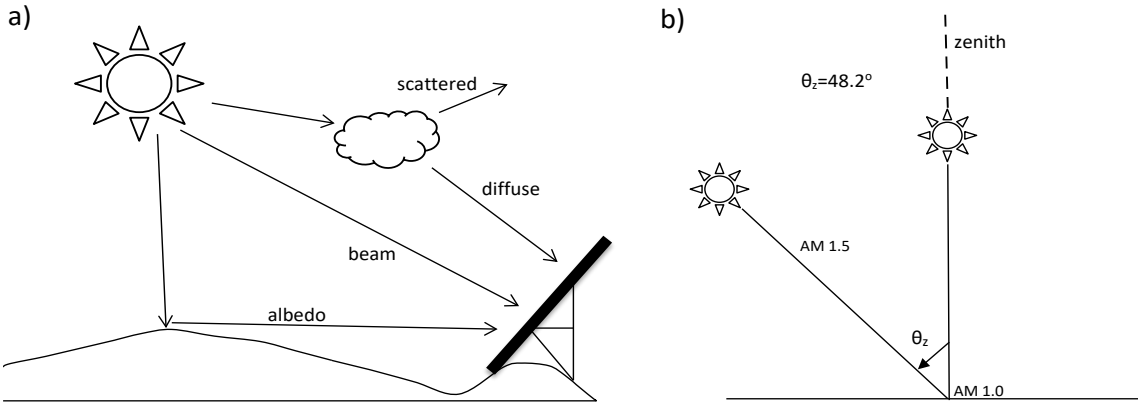

FIGURE 1.3: a) Solar radiation in the atmosphere b) Air mass

Figure 1.3-a demonstrates several types of solar radiation through the atmosphere. The radiation is called diffuse radiation when it arrives at a receiver after being scattered by clouds, while it is named albedo radiation when it reaches the receiver after being reflected by the ground. However, the radiation is called direct or beam radiation when there is no scattering or reflecting. The total radiation of direct, diffuse and albedo radiation is defined as the global radiation [37].

The relative path length of a direct beam through the atmosphere is called air mass (AM), which is an important parameter in the characterisation of solar cells. AM is calculated from $\sec\theta_z$ where θ_z is the angle from zenith as shown in Figure 1.3-b [42]. In clear weather conditions at sea level, AM is equal to 1 when the sunlight is at the zenith. AM 1.5 at the zenith angle of 48.2 ^oC is used in standard test conditions for solar cells together with the standard irradiance of 1 kW/m^2 [43].

1.4.2 Fundamentals of Semiconductors

1.4.2.1 Energy Bands

The energy levels occupied by electrons within the crystalline solid construct energy bands, which are the conduction band and valence band. The valence band is the highest occupied energy band at absolute zero, while the conduction band is the lowest unoccupied band. The highest energy level in the valence band and the lowest energy level in the conduction band are denoted as E_v and E_c, respectively. The energy difference between the top of the valence band and the bottom of the conduction band is defined as the energy band gap, E_g [41].

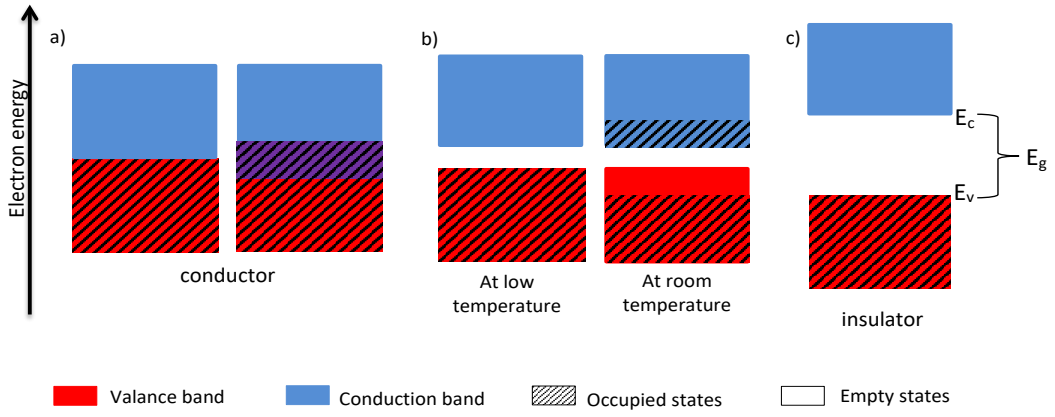

FIGURE 1.4: Schematic energy band diagram of a) conductors, b) semiconductors, and c) insulators

Figure 1.4 demonstrates the energy band diagrams of the conductor, semiconductor, and insulator. In insulator materials, the band gap is wide enough to forbid the movement of the electrons from the valence band to the conduction band; on the other hand, in conductive materials, the band gap disappears, and conduction and valence bands are adjacent or overlap, which provides the electron movement without facing any obstruction. As for semiconductor devices, the energy band gap exists at low temperatures, yet it is narrower than the band gap of insulators. Additionally, at room temperature, some electrons in the valence band find enough energy to jump into the conduction band due to thermal excitation, and thereby the semiconductor becomes conductive. The vacant spaces in the valance band, which are created after the electron movement from the valance band to the conduction band, are called 'holes' [39].

1.4.2.2 Semiconductors under Illumination

The empty conduction band and the fully occupied valence band are divided by the energy band gap for the intrinsic (pure) semiconductors in absolute zero and dark.

Once the semiconductor is illuminated with light, a photon excites an electron from the valence band (VB) to the conduction band (CB), and an electron deficiency in the valence band is created, thereby electron-hole pair is formed, which is demonstrated in Figure 1.5-a.

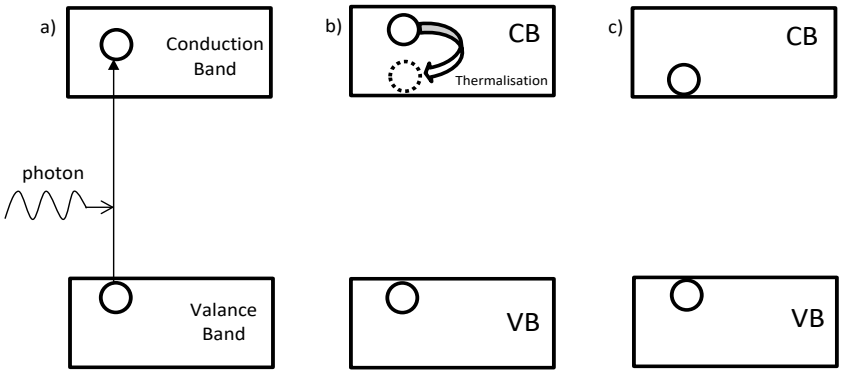

FIGURE 1.5: Creation of electron-hole pairs in semiconductors under illumination by following the process of (a) light absorption, (b) thermalisation and (c) creation of the pairs

The photons, which have energy higher than the band gap, are absorbed by semiconductors. Photons with lower energy than the band gap do not have enough energy to excite the electrons, so they do not create electron-hole pairs. Thus, a semiconductor with a certain band gap absorbs a finite part of the spectrum, and the photon flux density in $s^{-1}.m^{-2}$ is given by [44]:

$$\Phi(E_g) = \int_{E_g}^{\infty} \phi_E(E) dE \tag{1.5}$$

where ϕ_E is the spectral photon flux density in $s^{-1}.m^{-2}.eV^{-1}$, and E denotes photon energy in eV. As an electron-hole pair is created, its energy is higher than the band gap. After the interactions with the lattice, the nuclei, and the lattice vibrations, the excited electron and hole lose their excess energy and are located at an energy level close to band edges. The process is called 'thermalisation' illustrated in Figures 1.5-b and 1.5-c. Therefore, the energy of the electron and the hole is denoted by E_c and E_v, respectively. All photogenerated electron-hole pairs have the same energy equaling the energy band gap.

The first step for the conversion of light to electricity is the absorption of light and the creation of mobile charge carriers, or electron-hole pairs. The following step is the separation of charge carriers to produce current, voltage and power. In the photovoltaic conversion, it is expected that one photon creates one electron in the external circuit, so the current of a solar cell is estimated. Yet, in general, the number of generated electrons is less than the number of photons. In case one photon creates

one electron, the current in Amperes can be calculated by [37]:

$$I = \Phi A q \tag{1.6}$$

where Φ is the photon flux density of a monochromatic beam in $s^{-1}.m^{-2}$, A is the area in m^2 exposed to light. Besides, the maximum voltage of the monochromatic beam is $V = E/q$, where E is the photon energy because the electric potential energy is not larger than the photon energy creating electron-hole pairs. Therefore, using $P = IV$ [38], the maximum power output in Watts is obtained as:

$$P = \Phi A E \tag{1.7}$$

Thus, the maximum power conversion efficiency for a monochromatic converter is equal to 100%. Nevertheless, semiconductors are different from monochromatic converters because they absorb a broad range of wavelengths. Additionally, they are facing fundamental losses. For instance, semiconductors cannot absorb light having energy below the band gap energy, which causes a loss of photon flux and thus provokes current loss. Another loss is energy loss during thermalisation after the electron-hole pair is created, which causes voltage loss.

The current density of a semiconductor without applied external voltage is given by [44]:

$$J(E_g) = q \int_{E_g}^{\infty} \phi_E(E) dE \tag{1.8}$$

where ϕ_E is the spectral photon flux density. After applying $I = J \times A$ [38], the corresponding current in Amperes is found as:

$$I(E_g) = Aq \int_{E_g}^{\infty} \phi_E(E) dE \tag{1.9}$$

Additionally, the voltage of a semiconductor and the energy band gap relationship is given by [37]:

$$qV \leq E_g \tag{1.10}$$

where qV defines the energy of separated charges at terminals of the converter. On the other hand, the right-hand side of the equation represents the energy of thermalised electron-hole pairs after absorption, which denotes the band gap energy, unlike the monochromatic beam in which the energy is the energy of the photon. Thus, using Equation 1.8 and Equation 1.10 in $P = J \times V$ [45], the maximum power density in $W.m^{-2}$ measured by the terminals of a solar cell is given by:

$$P_{out} = E_g \int_{E_g}^{\infty} \phi_E(E) dE \tag{1.11}$$

Besides, the incident irradiance power density in W.m^{-2} is given by [44]:

$$P_{in} = \int_0^\infty e_E(E)dE = \int_0^\infty E\phi_E(E)dE \tag{1.12}$$

where e_E is the spectral irradiance. Therefore, the maximum efficiency of a single-junction solar cell is defined by [44]:

$$\eta = \frac{J(E_g)V(E_g)}{P_{in}} = \frac{E_g \int_{E_g}^\infty \phi_E(E)dE}{\int_0^\infty E\phi_E(E)dE} \tag{1.13}$$

The selection of a semiconductor with an optimum energy band gap is important for photovoltaic conversion. On the one hand, once a semiconductor with a band gap near 0 eV is selected, the voltage is almost zero, although the current density is at its maximum. On the other hand, when a semiconductor with a band gap close to 4 eV is chosen, the current decreases to zero even though the voltage increases. Hence, the energy band gap of semiconductors should be between 1-1.5 eV to produce a solar cell with high efficiency.

1.4.2.3 Doping in Semiconductors

Semiconductors are insulators in an intrinsic form, but they are transformed into conductive materials when photons are absorbed because the absorption creates mobile electrons in the conduction band and mobile holes in the valence band. Besides, semiconductors are turned into conductive materials adding impurities into the semiconductor lattice, namely 'doping' [39].

The band theory is used to explain the transformation of semiconductors into conductors adding impurities. In the crystal structure of silicon, each atom needs four symmetrically positioned bonds to neighbouring atoms to construct a tetrahedral crystalline structure known as a diamond lattice in Figure 1.6 [41].

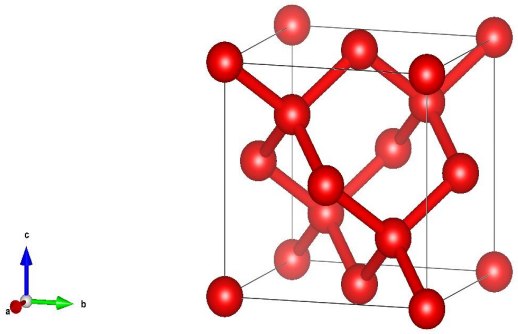

FIGURE 1.6: The crystal structure of diamond

Silicon is a group-IV element like germanium and diamond, whose electronic configuration consists of four outer electrons, and it needs four symmetrically positioned bonds to neighbouring atoms so that covalent bonding is constructed between the atoms [39]. In the crystalline structure, each bond includes two electrons, which are valence electrons in the band structure. Intrinsic silicon is an insulator as the electrons are fixed in the crystalline structure, and there are not any mobile electrons to provoke conductivity. The semiconductor starts conducting electricity once an impurity is added to the silicon.

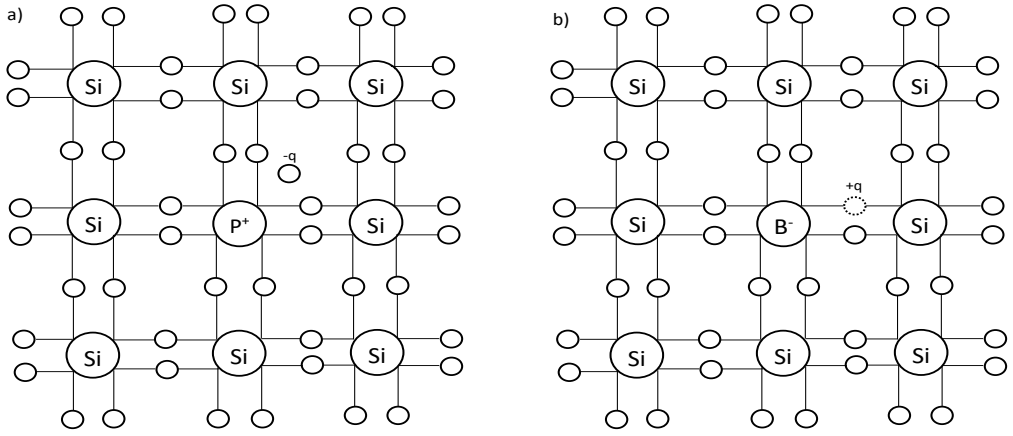

FIGURE 1.7: Schematic diagram of silicon a) with a group five impurity b) with a group three impurity

The four outer electrons of silicon are satisfied by the four outer electrons of a group-V element when silicon is doped by the group-V element like phosphorous, arsenic, etc. The fifth outer electron of the group-V element stays free in the crystalline structure in Figure 1.7-a. The free charge makes silicon conductive and presented in a conduction band. The group-IV semiconductors doped by a group-V element are named n-type semiconductors because they provide mobile negative charge carriers into the crystalline structure. Additionally, the group-V impurities are called donors because they donate electrons to the conduction band of the group-IV semiconductors [46].

On the other hand, an electron deficiency occurs in the crystal structure when silicon is doped by a group-III element like boron, gallium, etc. Therefore, in the crystalline structure, three bonds including two electrons and one bond with one electron are constructed in Figure 1.7-b. The electron deficiency is named the hole presented in the valence band. Holes are considered positive charge carriers, and the doped semiconductor is named a p-type semiconductor. Besides, group-III impurities are called acceptors [46].

1.4.2.4 Current-Voltage Characteristics of Solar Cells

A p-n junction is the combination of p-type and n-type semiconductors, which are produced by group three and group five impurities, respectively, shown in Figure 1.8-a. Once the n-type semiconductor having mobile electrons and the p-type semiconductor owning mobile holes are combined, the electrons move to the p-type side, while the holes move into the n-type side. The electrons and holes near the interface recombine, and thereby depletion region is constructed in Figure 1.8-b.

At the depletion region, a dipole field is constructed, which obstructs the further motion of charge carriers. The dipole field creates a potential barrier, which prevents electrons' movement to the p-side and holes' movement to the n-side. The potential barrier is purely internal and not measured from the terminals of the semiconductor. It is denoted by V_{bi} meaning built-in potential in Figure 1.8-c. The built-in potential barrier is changed by applying an external voltage, V. If forward bias is applied, the potential barrier lowers in Figure 1.8-d.

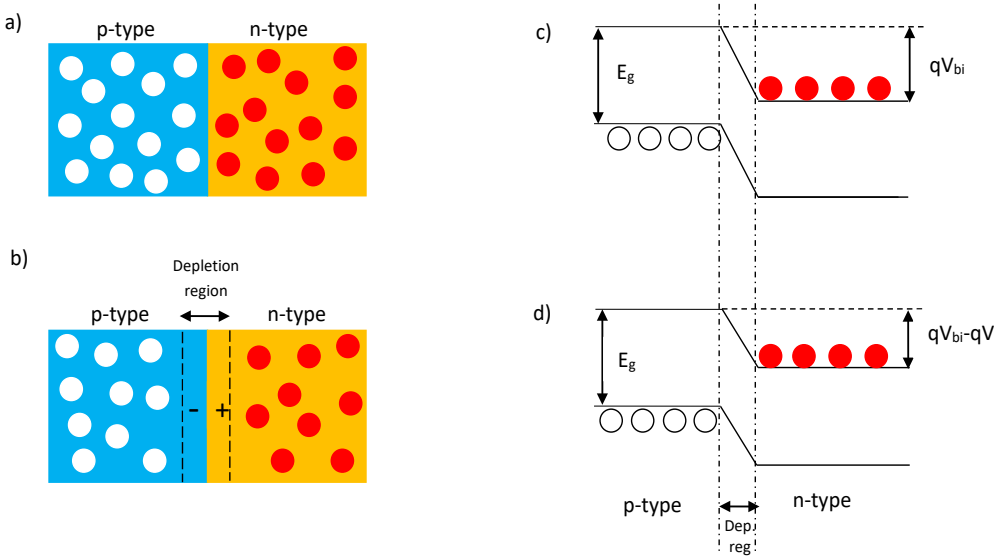

FIGURE 1.8: Schematic diagrams of a) combination of p-type and n-type semiconductors b) construction of depletion region c) band structure of p-n junction d) band structure of p-n junction under applied voltage

The net current flowing through the junction is given by [47]:

$$I = I_0 \left\{ exp\left(\frac{qV}{k_B T}\right) - 1 \right\} \tag{1.14}$$

where I_0 is the current at thermal equilibrium. Equation 1.14 is named the ideal diode equation determining current-voltage (I-V) characteristics of a semiconductor, rectifier, or diode.

The electron-hole pairs are created after illumination of the p-n junction. Negative charge carriers in the n-side produced by the illumination are much fewer than the carriers created by doping. However, the number of negative charge carriers significantly increases on the p-side after the illumination. Thus, the created electrons on the p-side provoke the photogenerated current, I_l, which follows the same path as the electrons created by thermal activation over the band gap. The photogenerated current is added to the current of I_2 because it reinforces the electron current across the band gap. The net current through the junction is given by [48]:

$$I = I_0 \left\{ exp\left(\frac{qV}{k_B T}\right) - 1 \right\} - I_l \tag{1.15}$$

Additionally, the photogenerated current is temperature independent, but it depends on light intensity. Hence, the current is well approximated by the linear function of the irradiance. Once I is changed by $-I$, the current is given by [49]:

$$I = I_l - I_0 \left\{ exp\left(\frac{qV}{k_B T}\right) - 1 \right\} \tag{1.16}$$

which is named the Shockley solar cell equation. Figure 1.9 illustrates the current-voltage characteristics of solar cells and diodes.

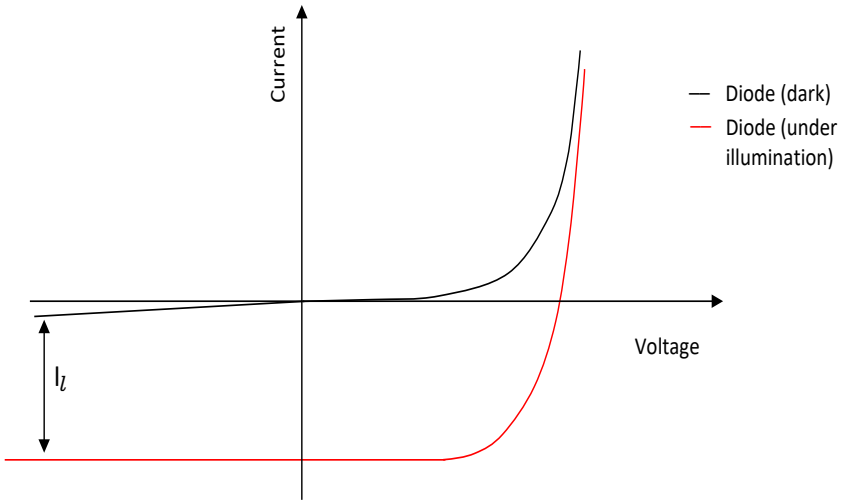

FIGURE 1.9: I-V characteristics of diodes in dark (black) and under illumination (red)

As for electrical terms of solar cells, the current at zero voltage is named short circuit current denoted by I_{sc}. The current is the photogenerated current, I_l. On the other

hand, the voltage at zero current is called open circuit voltage denoted by V_{oc} and given by [47]:

$$V_{oc} = \frac{k_B T}{q} \ln\left(\frac{I_l}{I_0} + 1\right) \cong \frac{k_B T}{q} \ln\left(\frac{I_l}{I_0}\right) \tag{1.17}$$

The addition of $+1$ in the natural logarithm is neglected as I_l is many orders of magnitude bigger than I_0. The maximum power output generated at maximum power point is given by [50]:

$$P_{max} = I_{mp} V_{mp} \tag{1.18}$$

where I_{mp} and V_{mp} are maximum current and voltage, respectively. Figure 1.10 demonstrates the I-V characteristics and power characteristics of solar cells.

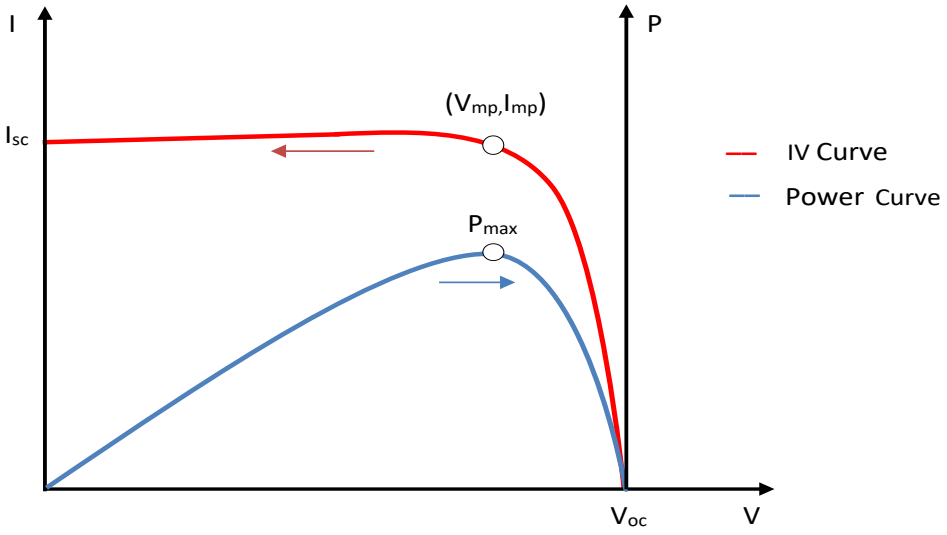

FIGURE 1.10: I-V curve and corresponding power characteristic of typical solar cells

The maximum power is also calculated by $P_{max} = FF\ I_{sc} V_{oc}$, where FF is the fill factor, which is the measure of how closely the shape of the I-V curve is rectangular in Figure 1.10. The fill factor is given by [49]:

$$FF = \frac{v_{oc} - \ln(v_{oc} + 0.72)}{v_{oc} + 1} \tag{1.19}$$

where $v_{oc} = V_{oc}/k_B T$.

As for the power conversion efficiency (PCE) of solar cells, it is defined as the ratio of the electrical power obtained from solar cells and the power of incident sunlight, and given by [41]:

$$PCE = \frac{P_{max}}{Incident\ Power} = \frac{I_m V_m}{Area \times Irradiance} = \frac{FF I_{sc} V_{oc}}{AG} \tag{1.20}$$

The efficiency of solar cells is determined by the measurements in standard test conditions, which are the temperature of 25 ^{o}C and the irradiance of 1 kW/m^2. Additionally, the maximum power point is chosen for the efficiency calculations.

The number of electrons produced by incident photons is defined by the quantum efficiency of solar cells, Q_E. Therefore, the photogenerated current density is given by [40]:

$$J_l = qQ_E\Phi \tag{1.21}$$

where Φ is incident photon flux density. Q_E is also named external quantum efficiency as it stems from external illumination.

Although I_{sc} is proportional to the irradiance and almost independent of the temperature, V_{oc} strongly depends on temperature and is given by [49]:

$$V_{oc} \cong \frac{k_B T}{q} \ln\left(\frac{I_l}{I_0}\right) = \frac{k_B T}{q} \ln\left(\frac{I_l}{Ce^{-E_g/k_B T}}\right) = \frac{E_g}{q} - \frac{k_B T}{q} \ln\left(\frac{C}{I_l}\right) \tag{1.22}$$

where C is a prefactor which is weakly dependant on temperature. V_{oc} does not increase with temperature because I_0 also depends on the temperature. Besides, V_{oc} weakly depends on irradiance through I_l, yet it is not as strong as I_{sc}. The maximum efficiency from a solar cell is obtained when the voltage is equal to the ratio of E_g/q. However, this maximum voltage cannot be obtained from a real solar cell, and it is just for ideal conditions. Moreover, V_{oc} cannot be higher than the band gap and lowers with increasing temperature according to Equation 1.22.

1.4.3 Charge Carrier Statistics

1.4.3.1 Density of Carriers

Each allowed energy level in a crystal can be occupied by a maximum of two electrons with opposite spins according to the Pauli exclusion principle. At low temperatures, the electrons are allowed to occupy up to a certain energy level, which is called the 'Fermi level' denoted by μ, which is described in more detail in Section 1.4.3.2. Once the temperature increases, some electrons gain enough energy to settle in a higher energy level denoted by E. The probability of the occupation is given by [41]:

$$f(E) = \frac{1}{1 + e^{(E-\mu)/k_B T}} \tag{1.23}$$

where k_B is the Boltzmann constant, and T is the absolute temperature. Besides, the number of permitted energy states per unit volume and energy, namely density of states, is given by [43]:

$$N(E) = \frac{8\sqrt{2}\ \pi\ m_e^{*3/2}}{h^3}\sqrt{E - E_c} \tag{1.24}$$

where m_e^* is the effective mass of electron, h is the Planck's constant, and E_c is the band edge of conduction band. The number of electrons per unit volume in the conduction band of the crystal is given by [41]:

$$n = \int_{E_c}^{E_{max}} f(E)N(E)dE \tag{1.25}$$

At high temperatures, because of $E - \mu \gg k_B T$, Equation 1.23 can be converted to [41]:

$$f(E) \approx exp\left(\frac{\mu - E}{k_B T}\right) \tag{1.26}$$

Once the upper limit of the integral in Equation 1.25 is taken as infinity since there are not any levels above the E_{max}, the density of states is obtained by [41]:

$$n = 2\left(\frac{2\,\pi\, m_e^*\, k_B T}{h^2}\right)^{3/2} exp\left(\frac{\mu - E_c}{k_B T}\right) \tag{1.27}$$

Once electrons are excited to the conduction band, they are rapidly thermalised and occupy only a narrow shell near E_c. The width of the shell occupied by electrons after thermalisation is equal to the thermal energy of $k_B T$. The number of states in this shell of the conduction band is denoted by N_c. Thus, the number of electrons per unit volume is given by [39]:

$$n = N_c(T)\exp\left(\frac{\mu - E_c}{k_B T}\right) \tag{1.28}$$

N_c depends on the temperature and volume of the semiconductor. A semiconductor with a larger crystal structure has a higher number of states. Hence, N_c is also called the density of states. In the Boltzmann approximation, the density of electrons in the conduction band is given by Equation 1.28 where $N_c(T)$ is the effective density of states.

On the other hand, the hole density in the valence band in thermal equilibrium is given by [39]:

$$p = 2\left(\frac{2\,\pi\, m_p^*\, k_B T}{h^2}\right)^{3/2} exp\left(\frac{E_v - \mu}{k_B T}\right) \tag{1.29}$$

where m_p^* is effective mass of holes and E_v is the band edge of valence band. Therefore, the density of holes in the valence band is given by [39]:

$$p = N_v(T)\exp\left(\frac{E_v - \mu}{k_B T}\right) \tag{1.30}$$

where $N_v(T)$ is the effective density of states in the valence band.

1.4.3.2 Chemical Potential

The energy of electrons, μ, is determined by integrating electron density and given by [49]:

$$\mu = E_c + k_B T \ln\left(\frac{n}{N_c}\right) \tag{1.31}$$

The number of electrons is always smaller than the density of states. Therefore, μ is always lower than E_c and higher than E_v. μ is called chemical potential, which is thermodynamic energy. It is a free energy per electron and useful work within the electron concentration at the temperature of T.

The chemical potential of electrons is also called the Fermi level. The states are occupied by electrons below the Fermi level, while they are empty above the Fermi level. In semiconductors, the Fermi level is in the band gap, so the valence band is occupied, whereas the conduction band is unoccupied. In thermal equilibrium, in which solar cells are in the dark and not exposed to an external voltage, the chemical potential is constant throughout the system.

Charge carriers are only created by adding impurities in thermal equilibrium. For example, in n-type semiconductors, the number of charge carriers is equal to the number of donors, whereas the number of carriers is equal to the number of acceptors in p-type semiconductors. Hence, the chemical potential can be calculated using the donor and acceptor concentrations.

The chemical potential of an intrinsic semiconductor is close to the middle of the band gap. In a p-type semiconductor, the chemical potential is in the bottom half of the energy band gap, while the electrochemical potential in an n-type semiconductor is in the top half. The chemical potential on the n-side, namely the electrochemical potential, is given by [51]:

$$\mu_e = E_c(r) - k_B T \ln\left(\frac{N_c}{n}\right) \tag{1.32}$$

where $E_c(r)$ is the position-dependent energy of the bottom of the conduction band, N_c is the density of states in the conduction band, and n is the electron concentration on the n-side, which is equal to donor concentration on the n-side.

On the other hand, the chemical potential on the p-side is given by [46]:

$$\mu_h = E_v(r) + k_B T \ln\left(\frac{N_v}{p}\right) \tag{1.33}$$

where $E_v(r)$ is the position-dependent valance band edge, N_v is the density of states in the valence band, and p is the hole concentration on the p-side, which is equal to the acceptor concentration on the p-side.

1.4.3.3 Mass Action Law

Semiconductors and solar cells operate at a certain temperature at which electrons are thermally activated to the other band. Charge carriers created by thermal activation are named minority charge carriers, while carriers produced by doping are called majority charge carriers.

The electrochemical potential is equal to the chemical potential of holes in thermal equilibrium, so $\mu = \mu_e = \mu_h$. Additionally, once the electron and hole concentrations are defined by n_0 and p_0, respectively, the product of the densities is defined as mass action law and given by [51]:

$$n_0 p_0 = N_c N_v e^{-E_g/k_B T} = {n_i}^2 \tag{1.34}$$

where n_i is the electron and hole concentrations in an intrinsic semiconductor. In thermal equilibrium, the product of electron and hole densities is independent of doping. Electrons and holes of an intrinsic semiconductor are of equal concentration, and thereby [43]:

$$n_i = n = p \tag{1.35}$$

$$N_c \; e^{(\mu - E_c)/k_B T} = N_v \; e^{(E_v - \mu)/k_B T} \tag{1.36}$$

Therefore, the chemical potential of the intrinsic semiconductor is given by [43]:

$$\mu = \frac{E_c + E_v}{2} + \frac{k_B T}{2} \ln\left(\frac{N_v}{N_c}\right) \tag{1.37}$$

Equation 1.37 shows that the Fermi level is in the middle of the energy band gap.

On the other hand, solar cells do not operate in thermal equilibrium, so they do not produce electricity in the dark and without an external voltage. Once they are excited by light, mobile charge carriers are created and called minority charge carriers because the number of carriers created by light is much smaller than the number of carriers produced by doping. Under illumination, the majority carrier concentration is approximately the same as in thermal equilibrium. Nevertheless, the minority carrier concentration is significantly increased under illumination. Additionally, the chemical potentials of electrons and holes are different under illumination, which is called splitting of Fermi levels.

Once the electrochemical potential and the chemical potential of holes are different, the product of the concentration of charge carriers in Equation 1.36 is obtained as:

$$np = N_c N_v e^{\mu_e - E_c + E_v - \mu_h / k_B T} \tag{1.38}$$

Therefore, the mass action law is generalised as [40]:

$$np = n_i{}^2 e^{\Delta\mu/k_B T} \tag{1.39}$$

where $\Delta\mu$ is the subtraction of $\mu_e - \mu_h$. The difference between the chemical potential on the p-side and the chemical potential on the n-side is equal to the voltage across the junction. Thus, the mass action law is given by [40]:

$$np = n_i{}^2 e^{qV/k_B T} \tag{1.40}$$

Figure 1.11 demonstrates energy band diagrams and chemical potentials of the p-n junction in thermal equilibrium and away from equilibrium. There is only one chemical potential in thermal equilibrium because the electrochemical potential and chemical potential of holes are equal. Once an external voltage is applied, the potential difference of qV is observed. Besides, the chemical potential far from the junction on the p-side is the same as the chemical potential on the p-side in equilibrium. The same situation is also valid for the electrochemical potential on the n-side far from the junction. Thus, far from the junction, chemical potentials are equal to the equilibrium chemical potential, whereas chemical potentials are split near the junction.

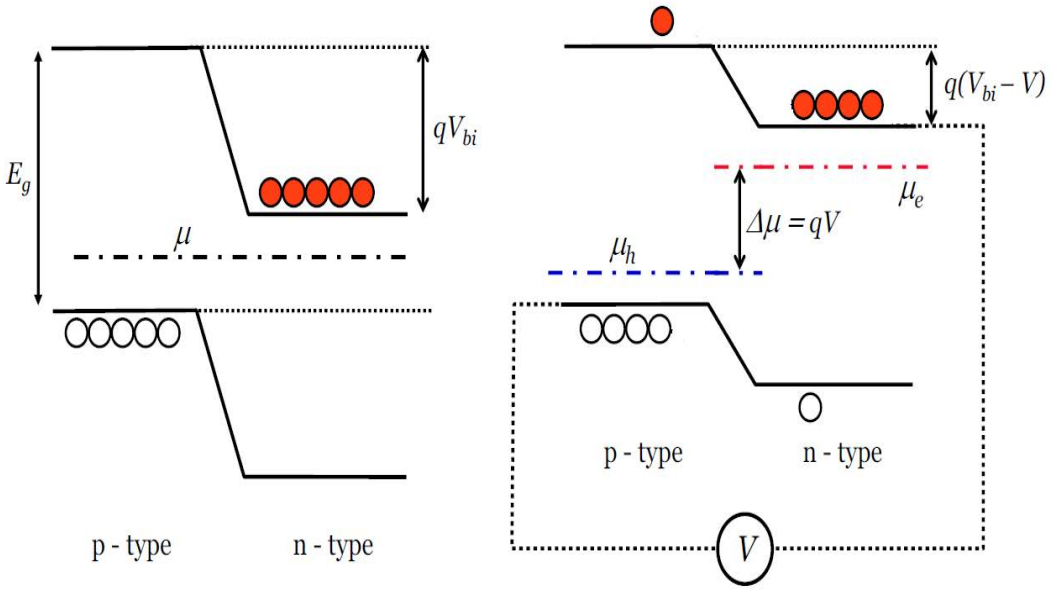

FIGURE 1.11: Energy band diagram of p-n junction in equilibrium (left hand-side) and under excitation (right hand-side)

1.4.4 Carrier Transport, Generation and Recombination

1.4.4.1 Carrier Transport

There are two driving forces to induce the motion of charge carriers which are electrons and holes. The first one is the electric field along the p-n junction. In thermal equilibrium, the electric field does not affect the movement of charge carriers, but away from the equilibrium it produces a current called drift current. On the other hand, the second force inducing the carriers' movement is the carrier concentration gradient causing diffusion current. Although it is not a mechanical force, it makes the charge carriers move to equilibrate carrier concentrations. Although there is an electric field along with a large concentration gradient in the p-n junction in thermal equilibrium, there is no movement of charges across the junction because these two forces cancel each other.

The diffusion current is determined by Fick's law, which gives the charge carrier current density resulting from a gradient in carrier density [46]. Once there is a non-uniform concentration of charge carriers, the carrier current density is proportional to the gradient of carrier density. The charge carrier diffusion current density is given by [39]:

$$j = -D\frac{dn(x)}{dx} \tag{1.41}$$

where D is the proportionality constant, namely the diffusion coefficient. Thus, the diffusion current density of electrons driven by the concentration gradient in one-dimension is given by [41]:

$$J_n = qD_n\frac{dn(x)}{dx} \tag{1.42}$$

where D_n is the diffusion coefficient of electrons. Additionally, the diffusion current density of holes is given by [41]:

$$J_p = -qD_p\frac{dp(x)}{dx} \tag{1.43}$$

where D_p is the diffusion coefficient of holes. The diffusion coefficients are related to carrier mobilities and defined by Einstein relations [43]:

$$D_n = \frac{k_B T}{q}\vartheta_n \tag{1.44}$$

$$D_p = \frac{k_B T}{q}\vartheta_p \tag{1.45}$$

where ϑ_n is the electron mobility, and ϑ_p is the hole mobility.

On the other hand, the drift current is determined by Ohm's law [41]. Once a semiconductor layer with the thickness of δx and the voltage drop of δV is considered, Ohm's law for the small element is given by [39]:

$$\delta V = RI \tag{1.46}$$

where R is the resistance of the thin layer, and I is the current. The voltage drop related to the electric field is given by [39]:

$$\delta V = \varepsilon \delta x \tag{1.47}$$

The resistance is proportional to the thickness and given by [39]:

$$R = \rho \frac{\delta x}{A} \tag{1.48}$$

where ρ is the proportionality constant called resistivity of the semiconductor, and A is the area of the layer. Additionally, the electric field proportional to the current density is given by [43]:

$$\varepsilon = \rho J \tag{1.49}$$

Thus, the drift current density related to the electric field is given by [39]:

$$J_d = \sigma \varepsilon = -\sigma \frac{d\varphi}{dx} \tag{1.50}$$

where σ is the conductivity, and φ is the electrostatic potential. Therefore, the electrical current density, J_n, and hole current density, J_p, in three dimensions is given by [49]:

$$J_{tn} = qD_n \nabla n(r) - q\vartheta_n n(r) \nabla \varphi(r) \tag{1.51}$$

$$J_{tp} = -qD_p \nabla p(r) - q\vartheta_p p(r) \nabla \varphi(r) \tag{1.52}$$

where $\sigma_n = qn\vartheta_n$ and $\sigma_p = qp\vartheta_p$ are electron and hole conductivities, respectively.

1.4.4.2 Carrier Generation

According to Beer-Lambert law, once a solar cell is illuminated by a photon flux, the photon flux density for a thin slab is given by [42]:

$$\delta \Phi = -\alpha \Phi(x) \delta x \tag{1.53}$$

where δx is the thickness of the thin slab, α is the constant of proportionality called absorption coefficient. The absorption coefficient is a universal function for each material and is independent of doping and defects in semiconductors.

Once the reflection of photons is considered, the photon flux density at x depth is given by [41]:

$$\Phi(x) = \Phi_0(1 - R)e^{-\alpha x} \tag{1.54}$$

where R is the reflection coefficient and Φ_0 is the photon flux density of incident light at the surface.

The number of photons absorbed per unit of time is equal to the number of electron-hole pairs produced after the absorption. The generation rate of the free electron-hole pairs in the thin slab is controlled by the photon flux density given by Equation 1.53. Thus, the generation rate in $m^{-3}.s^{-1}$ is given by [52]:

$$g(x)\delta x = -\delta\Phi = \alpha\Phi(x)\delta x \tag{1.55}$$

Therefore, the generation function, which is the number of electron-hole pairs generated per unit volume per unit time, is given by [50]:

$$g(x) = \Phi_0(1 - R)e^{-\alpha x}\alpha \tag{1.56}$$

Once a monochromatic light and white light are considered, the corresponding generation functions are given by [40]:

$$g_\lambda(x) = (1 - R_\lambda)e^{-\alpha_\lambda x}\alpha_\lambda\Phi_\lambda(\lambda) \tag{1.57}$$

$$g(x) = \int (1 - R_\lambda)e^{-\alpha_\lambda x}\alpha_\lambda\Phi_\lambda(\lambda)d\lambda \tag{1.58}$$

The absorption of light causes the movement of an electron from the valence band to the conduction band once the energy of a photon is higher than the band gap of the semiconductor. The momentum of the photon is determined by the De Broglie relationship and given by [41]:

$$\varrho = h\nu/c = h/\lambda \tag{1.59}$$

Additionally, the relationship between momentum and energy of a free electron is defined by [43]:

$$E = \frac{\varrho^2}{2m} \tag{1.60}$$

where m is the mass of the electron. Once the propagation constant, k, is considered, the energy-momentum relation is given by [39]:

$$E = \frac{\hbar^2 k^2}{2m} \tag{1.61}$$

where $\hbar = h/2\pi$ and $k = 2\pi/\lambda$. Once Equation 1.61 is differentiated twice by k, the mass of the free electron is obtained by [39]:

$$m = \frac{\hbar^2}{d^2E/dk^2} \tag{1.62}$$

which is also used for determining the effective mass of an electron in the crystal.

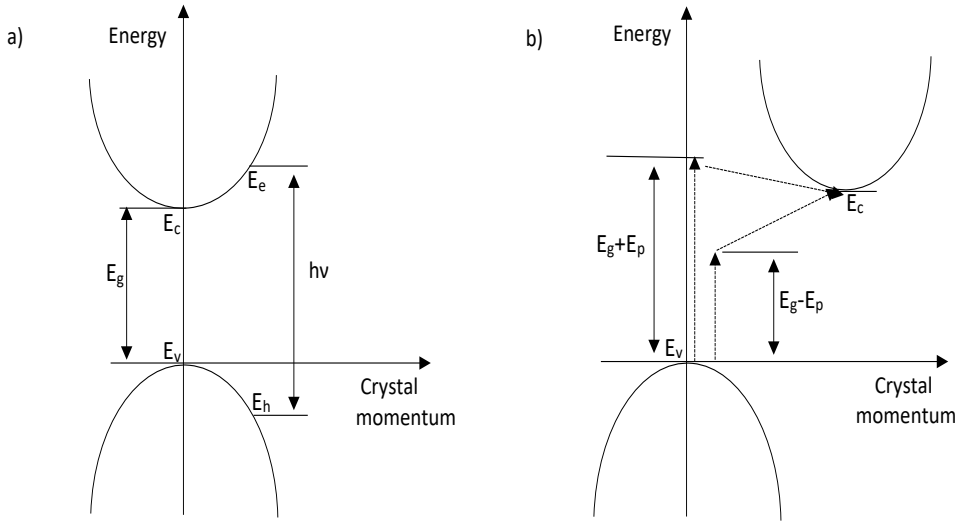

FIGURE 1.12: Schematic diagram of energy-momentum relationship in a) direct-band-gap b) indirect-band-gap semiconductors

Figure 1.12-a demonstrates the energy-crystal momentum relationship for direct band gap semiconductors. In direct band gap semiconductors, the crystal momentum of the minimum energy of the conduction band is the same as the momentum of the maximum energy of the valence band. Therefore, the minimum energy and the maximum energy have the same wave vector of k. Once photon energy of $h\nu$ is considered, the absorption coefficient of direct band gap semiconductors is defined by [42]:

$$\alpha_\lambda = C(h\nu - E_g)^{1/2} = C\left(\frac{hc}{\lambda} - E_g\right)^{1/2} \tag{1.63}$$

where C is a constant.

Additionally, in direct-band-gap semiconductors, the energy-momentum relationship of an electron in the conduction band is given by [41]:

$$E_e - E_c = \frac{\varrho^2}{2m_e^*} \tag{1.64}$$

where m_e^* is the effective mass of the electron. As for a hole in the valence band, its energy-momentum relationship is given by [41]:

$$E_v - E_h = \frac{\varrho^2}{2m_h^*} \tag{1.65}$$

where m_h^* is the effective mass of the hole.

On the other hand, in indirect band gap semiconductors, the crystal momentum of the minimum energy of the conduction band differs from the crystal momentum of the maximum energy of the valence band. The excitation of electrons from the valence band to the conduction band is achieved by involving another particle, which has high momentum, but low energy. The particle is called phonon, which is a lattice vibration at finite temperatures [39].

Figure 1.12-b illustrates the energy-crystal momentum relationship of indirect-band-gap semiconductors. The electron movement from the valence band maximum to the conduction band minimum occurs by absorbing or emitting the energy of the phonon, E_p, when the energy of the photon is of $E_g - E_p$ or $E_g + E_p$, respectively [41].

1.4.4.3 Carrier Recombination

The recombination of charge carriers is the opposite process of electron-hole pairs generation. The recombination of electron-hole pairs occurs by several mechanisms, such as band-to-band, intermediate defect levels in the band gap. Figure 1.13 demonstrates the schematic diagrams of different recombination processes.

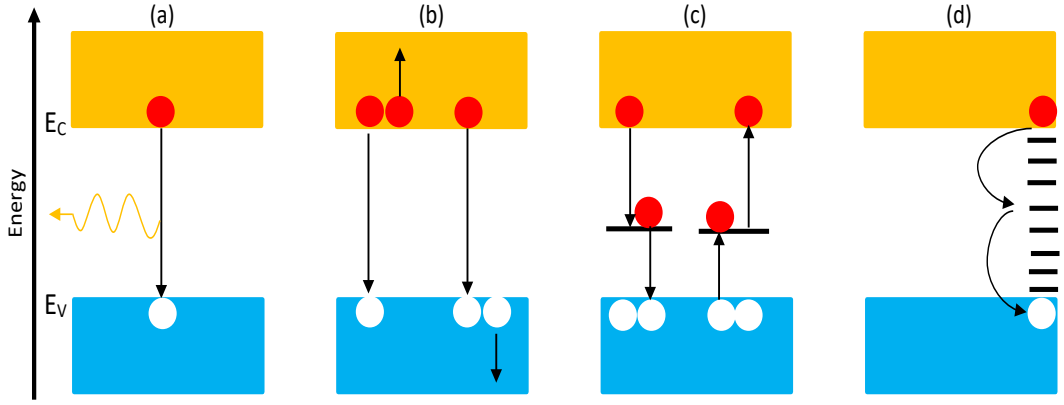

FIGURE 1.13: Schematic diagram of a) radiative recombination b) Auger recombination c) defect-assisted (SHR) recombination d) Surface recombination

Radiative recombination is an example of band-to-band recombination, which is the process of recombining an electron-hole pair by emitting a photon in Figure 1.13-a.

The rate of the radiative recombination defining the recombination of electron-hole pairs per unit of time per unit volume is given by [49]:

$$r_{rad} = B(np - n_0 p_0) \tag{1.66}$$

where B is a coefficient.

Another band-to-band recombination is the Auger recombination demonstrated in Figure 1.13-b. In this process, the energy of the recombined electron-hole pair is utilised by another charge. The rate of Auger recombination is given by [53]:

$$r_{Auger} = (C_{p0}p + C_{n0})(np - n_i^2) \tag{1.67}$$

where C_{p0} and C_{n0} are coefficients.

Another recombination occurs owing to defects causing intermediate levels into the band gap. The levels divide the emission of the energy into several steps and act as stepping-stones for the electron to gradually lose the energy where it recombines. This energy would disappear again into lattice vibrations and heat. This process is called defect-assisted, trap-assisted, or Shockley-Hall-Read (SHR) recombination in Figure 1.13-c. The recombination rate via defects is given by [54]:

$$r_{SHR} = \frac{np - n_i^2}{\tau_p(n + n_1) + \tau_n(p + p_1)} \tag{1.68}$$

where $n_1 = n_i \exp\left(\frac{E_t - E_i}{k_B T}\right)$, $p_1 = p_i \exp\left(\frac{E_t - E_i}{k_B T}\right)$, and E_t is the defect energy. τ_n and τ_p are parameters, which are proportional to the defect concentration and determine minority-carrier lifetimes at low injection.

According to low injection approximation, majority-carrier concentrations do not change and remain the same as the concentrations in equilibrium. Once a p-type semiconductor is considered, the hole concentration remains equal to the acceptor concentration, which means $p \cong p_0 = N_A$. Therefore, the recombination rate is obtained by [49]:

$$r = CN_A(n - n_0) = \frac{1}{\tau_n}(n - n_0) \tag{1.69}$$

where τ_n is the minority-carrier lifetime of an electron, which is inversely proportional to the constant, CN_A. Equation 1.69 shows that the recombination function is proportional to the difference between electron concentration from equilibrium, which is called excess minority carrier density. Besides, the recombination rate of n-type material can be derived similarly. The inverse of the lifetime in Equation 1.69 is a sum of different contributions to the lifetime and given by [53]:

$$\frac{1}{\tau} = \frac{1}{\tau_{rad}} + \frac{1}{\tau_{Auger}} + \frac{1}{\tau_{SHR}} \tag{1.70}$$

where τ is τ_n or τ_p by depending on the type of semiconductor.

The minority-carrier lifetime determines the length of carrier diffusion. Thus, the diffusion length is given by [49]:

$$L = \sqrt{D\tau} \tag{1.71}$$

where D is the diffusion constant. Once the drift flux in the electric field of ε is considered, the drift lengths for electrons and holes are obtained by [54]:

$$l_n = \varepsilon \tau_n \vartheta_n \tag{1.72}$$

$$l_p = \varepsilon \tau_p \vartheta_p \tag{1.73}$$

Surface recombination in Figure 1.13-d is a significant defect related to the transition symmetry of the crystal. The current density flowing towards the surface is equal to the surface recombination function, r_{surf}, as all charge carriers recombine at the surface. Thus, the recombination current density is given by [40]:

$$J_s = -q r_{surf} \tag{1.74}$$

Once a p-type semiconductor is considered, the surface recombination function is given by [40]:

$$r_{surf} = S(n - n_0) \tag{1.75}$$

where S is the surface recombination velocity, which is the equivalent of the minority-carrier lifetime in the bulk.

The treatment above is for the back surface. Once surface recombination velocity is high, when the back surface is covered by metal contact, electron concentration is equal to the electron concentration in equilibrium. The surface recombination is lowered by surface passivation. At the surface, there are some bonds, which are not satisfied by electrons, because of the distorted crystal structure. Once these dangling bonds are satisfied by attaching a material, such as silicon oxide, or silicon nitrate, the surface is passivated. Thus, surface recombination is reduced.

Chapter 2

Literature Review

2.1 Architecture of Perovskite Solar Cells

Perovskite solar cells are designed by using n-i-p or p-i-n type architecture. The cell is called an n-i-p design cell when the n-type semiconductor side of the cell, the electron transport layer side, is illuminated by solar radiation [55]. On the other hand, the cell is named p-i-n cell when the hole transport layer side faces the sunlight [56]. Figure 2.1 demonstrates n-i-p and p-i-n structured cells, in which planar and mesoporous carrier selective layers were used [57].

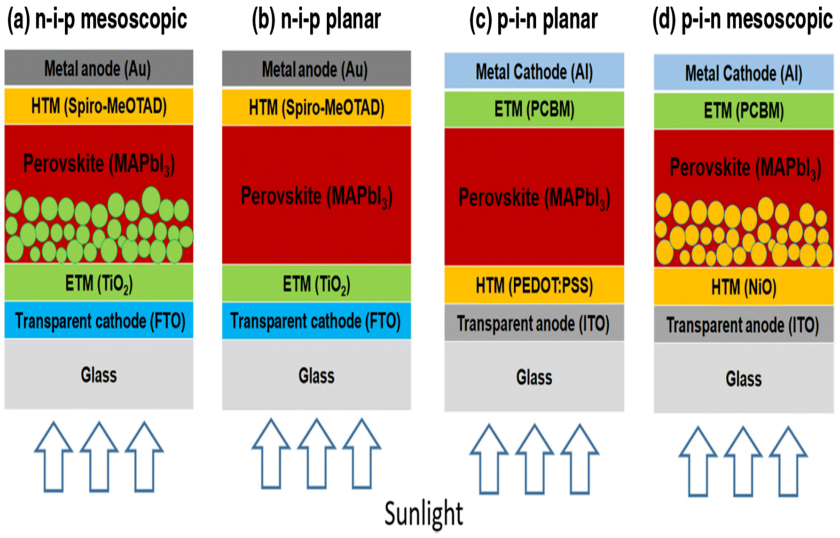

FIGURE 2.1: Schematics of architectures of perovskite solar cells in n-i-p and p-i-n configurations [57].

As for the size of perovskite solar cells, high efficiencies of perovskite solar cells are obtained with small aperture area devices, <0.1 cm^2, yet small size cells cause errors in the device performance measurements [58]. Therefore, the active cell areas of perovskite solar cells are expected to be >1 cm^2 for obtaining reliable results from the

devices [59]. Nevertheless, large-size perovskite solar cells complicate the continuous fabrication of cracks- and pinhole-free perovskite and carrier selective layers [29]. Hence, preparation techniques of the devices gain importance to overcome the drawbacks of large-size perovskite solar cells.

2.1.1 Electron Transport Layer

The n-type semiconductor of TiO_2 has been frequently used as an electron transport layer in the studies of perovskite solar cell production [25]. Compact layer n-type TiO_2 was utilised as an electron transport layer in a planar heterojunction solar cell [60]. The device is designed by using the cell structure of FTO glass/ETL/ $CH_3NH_3PbI_{3-x}Cl_x$/spiro-OMeTAD(HTL)/Ag. The perovskite layer was obtained using the vapour deposition method, in which the organic part, CH_3NH_3I, and the inorganic part, $PbCl_2$, of the perovskite were simultaneously coated on the c-TiO_2 layer by separate sources. The power conversion efficiency of the planar thin-film solar cell was over 15%, which showed that perovskite solar cells with high efficiency are produced without the design complexity of the devices [60].

Modification of TiO_2 by doping can change the carrier concentration of the layer and thereby affect the cell performance. Yttrium-doped TiO_2 ($Y - TiO_2$) electron transport layer was utilised with the perovskite cell structure of ITO/ETL/$CH_3NH_3PbI_{3-x}Cl_x$ /spiro-OMeTAD/Au [61]. It was obtained that the conductivity of $Y - TiO_2$ films was higher than undoped TiO_2 with the values of 2×10^{-5} S/cm and 6×10^{-6} S/cm, respectively. It was assumed that the increase in the conductivity stemmed from the rise in carrier concentration of $Y - TiO_2$ films. Additionally, the ITO electrode was modified using a polymer, polyethyleneimine ethoxylated (PEIE), to reduce the work function of ITO. Therefore, the solar cell achieved the power conversion efficiency of 19.3% under AM 1.5 illumination [61].

N-type ZnO is another desirable ETL material. ZnO had higher electron mobility than TiO_2, and it was applied straightforwardly by spin-coating method without a sequent annealing process unlike TiO_2 [62]. Additionally, perovskite and hole transport layers were applied at room temperature, and thereby flexible solar cell fabrication was achieved [62]. The cell structure was determined as ITO/ZnO/$CH_3NH_3PbI_3$/ spiro-OMeTAD/Ag by using two different substrates, ITO/glass and ITO/poly-(ethylene terephthalate) (PET). The cell with glass substrate achieved a power conversion efficiency of 15.7%, while the PET cell provided PCE of 10.2%. Although the flexible cell did not have PCE as much as the glass substrate cell, it was important to prove that the flexibility of the solar cell was only limited by the substrate, not by the perovskite [62].

On the other hand, it was shown that electron transport through the perovskite layer was faster than through ETL of TiO_2 when the ETL layer was replaced by Al_2O_3 in the solar cell with the transparent HTL of spiro-OMeTAD [63]. Al_2O_3 behaved as a scaffold since its energy band gap, 7 to 9 eV, is much broader than that of the perovskite, 1.55 eV. The power conversion efficiency (PCE) of the solar cell with Al_2O_3 reached 10.9%, whereas the PCE of the cell having the ETL was obtained as 7.6% for $CH_3NH_3PbI_2Cl$ perovskite solar cells [63].

2.1.2 Hole Transport Layer

Organic transport layers poly(3,4-ethylenedioxythiophene) polystyrene sulphonate (PEDOT:PSS), and 2,2′,7,7′-tetrakis(N,N-pdimethoxyphenylamino)-9,9′-spirobifluorene (spiro-OMeTAD) can be used as p-type hole transport layers [64]. Spiro-OMeTAD is widely used in perovskite cells [65]. The usage of spiro-OMeTAD causes photoluminescence (PL) intensity quenching, which stems from carrier extraction between the perovskite and the HTL [66].

Inorganic p-type semiconductors, such as $CuSCN$, CuI, and NiO_x, can be used as the hole transport layer in the perovskite cell structure [64]. The usage of CuI as HTL with the cell structure of FTO/TiO_2(ETL)/$CH_3NH_3PbI_3$/HTL/Au provided not only higher electrical conductivity and higher fill factor but a cost-effective alternative to organic counterparts [67]. Nevertheless, the cell power conversion efficiency, 6%, was lower than the PCE of 7.9% from the cell produced by using an organic hole conductor layer, spiro-OMeTAD, on account of the lower potential output of the CuI cell [67].

Polymeric materials were studied as hole transport layers, which were poly-3-hexylthiophene (P3HT), poly-[2,1,3-benzothiadiazole-4,7-diyl[4,4-bis(2-ethylhexyl)-4H-cyclopenta[2,1-b:3,4-b']dithiophene-2,6-diyl]] (PCPDTBT), (poly-[[9-(1-octylnonyl)-9H-carbazole-2,7-diyl]-2,5-thiophenediyl-2,1,3-benzothiadiazole-4,7-diyl-2,5-thioph- enediyl]) (PCDTBT) and poly-triarylamine (PTAA) [68]. The devices were structured as FTO/dense blocking TiO_2/mesoporous TiO_2/$CH_NH_3PbI_3$/HTM/Au. The device produced using PTAA along with a 600 nm thick mesoporous TiO_2 layer yielded the highest power conversion efficiency of 12% among the polymeric HTL counterparts. On the other hand, the device with organic spiro-OMeTAD reached PCE of 8.4% under full sunlight illumination [68].

On the contrary, a perovskite solar cell without a hole conductor layer was introduced using TiO_2 nanosheets as electron collectors with methylammonium lead iodide perovskite ($CH_3NH_3PbI_3$) [69]. The perovskite layer coated on the TiO_2 layer using the spin-coating method behaved as both a light absorber and a hole conductor. The perovskite solar cell achieved PCE of 5.5% under standard AM 1.5 solar light of 1000 W/m^2 [69].

2.2 Preparation Methods of Perovskite Solar Cells

Spin-coating is the most common coating technique when the layers are constituted in the perovskite solar cell devices since it forms uniform layers. Additionally, the choice of solvent is also important for uniformity. γ-butyrolactone (GBL), N,N-dimethylformamide (DMF), dimethyl sulfoxide (DMSO) and N-methyl-2-pyrrolidone (NMP) are used as solvents when perovskite solution is prepared. The combination of two solvents has also affected the morphology of the perovskite layer. It was shown that the perovskite layer of the cell, which was prepared by spin-coating, was improved in terms of uniformity and density when the GBL and DMSO were used together as solvents [70]. Additionally, after the perovskite layer coating, toluene, which is non-solvent for perovskites, was applied to the perovskite layer by spin-coating. It was observed that the perovskite layer with toluene treatment had more uniformity than the layer without toluene, which had a textile-like inhomogeneous surface. After these processes, the cell with the perovskite of $MAPb(I_{1-x}Br_x)_3$ achieved PCE of 16.2% [70].

Vapour-assisted solution process was used to obtain planar perovskite films with microscale grainsize [71]. In this method, the inorganic component (PbI_2) was coated on the substrate, which was FTO glass with c-TiO_2 layer, and CH_3NH_3I vapour was applied on the PbI_2 film to form the perovskite layer of $CH_3NH_3PbI_3$ at 150 ^{o}C. The perovskite thin film achieved full surface coverage and small surface roughness in addition to microscale grain size. The cell construction was completed after the perovskite layer was coated with spiro-OMeTAD and thermally evaporated Ag. The solar cell reached PCE of 12.2% under the illumination of AM 1.5G solar irradiation [71].

Solvent-induced fast deposition-crystallisation procedure provided uniform perovskite thin films [72]. At this technique, $CH_3NH_3PbI_3$ in DMF was coated on the FTO glass with a dense TiO_2 layer by spin-coating. The following step was to apply chlorobenzene onto the perovskite to induce crystallisation. It was observed that the crystal grains in the thin film were in the size of microns. The solar cells with the architecture of FTO/TiO_2/perovskite/spiro-OMeTAD/Ag achieved PCE of 13% under standard AM 1.5G illumination [72].

The solution-based hot-casting technique was presented to obtain millimetre-sized crystalline grains in the perovskite thin film, which was uniform and pinhole-free [73]. The perovskite solution of lead iodide (PbI_2) and methylamine hydrochloride (MACl) at 70 ^{o}C was spin-coated on the FTO/PEDOT:PSS substrate at 180 ^oC. The cell designed as FTO/PEDOT:PSS/$CH_3NH_3PbI_{3-x}Cl_x$/PCBM/Al yielded PCE of approximately 18%. It was found that the grain size of the crystals increased remarkably when the substrate temperature increased from room temperature to 190 ^{o}C. DMF or NMP was suggested as the solvent owing to their high boiling points [73].

2.3 Perovskites with Varied Chemical Structure

The chemical structure of perovskites, ABX_3, can be modified by including another cation, metal, or halogen in the perovskite structure. Moreover, two different perovskites can be combined to produce another perovskite material. Therefore, the properties of perovskite solar cells can be tuned and improved. In this chapter, some studies examining dual metal perovskites and mixed perovskites have been demonstrated.

2.3.1 Dual Metal Perovskites

In this section, the studies on perovskite solar cells comprised of two metals have been examined. All perovskites were produced by combining Pb and Sn as the metal part of the organic-inorganic halide perovskite structure of AMX_3.

In 2013, Stoumpos et al. studied various hybrid metal iodide perovskites with the formation of AMI_3, where A is a cation such as MA ($CH_3NH_3^+$), FA ($HC(NH_2)^{2+}$) and Cs, M is a metal of Sn or/and Pb, in terms of thermal stability, optical and electrical properties of them [74]. It was shown that the preparation method and the level of impurities impacted the chemical and physical properties of perovskites. Temperature-dependent single-crystal X-ray diffraction results were used to investigate structural phase transitions and the relationship between resistivity and crystal structure. The charge transport properties of the materials were characterised using diffuse reflectance studies. Additionally, the charge transport type of these materials was determined by the Seebeck coefficient and Hall-effect measurements. It was demonstrated that the n- or p-type semiconductor formation was determined by the preparation method. For example, solution-processed materials acted as n-type semiconductors, while the compounds formed by solid-state reactions behaved as p-type semiconductors. In that study, the dual metal perovskite of $MASn_{1-x}Pb_xI_3$ was examined by using x of 0.25, 0.50 and 0.75 in terms of structural, electrical, and optical properties of them [74].

In 2014, Ogomi et al. demonstrated Sn/Pb-based perovskite with the formulation of $CH_3NH_3Sn_xPb_{(1-x)}I_3$ by combining the precursors of CH_3NH_3I, PbI_2 and SnI_2 [75]. The dual-metal perovskite solar cell structure was selected as F-doped SnO_2 layered glass/compact titania layer (35 nm)/porous titania layer (200 nm)/ $CH_3NH_3Sn_xPb_{(1-x)}I_3$/regioregular ploy(3-hexylthiophene-2,5-diyl)(P3HT)(100 nm) /cathode electrode (Ag (10 nm) and Au (55 nm)). The highest PCE of the cell, 4.18%, was obtained when x was equal to 0.5, with the open circuit voltage, V_{oc}, of 0.42 V, fill factor, FF, of 0.50, and short circuit current density, J_{sc}, of 20.04 mA.cm^{-2} [75].

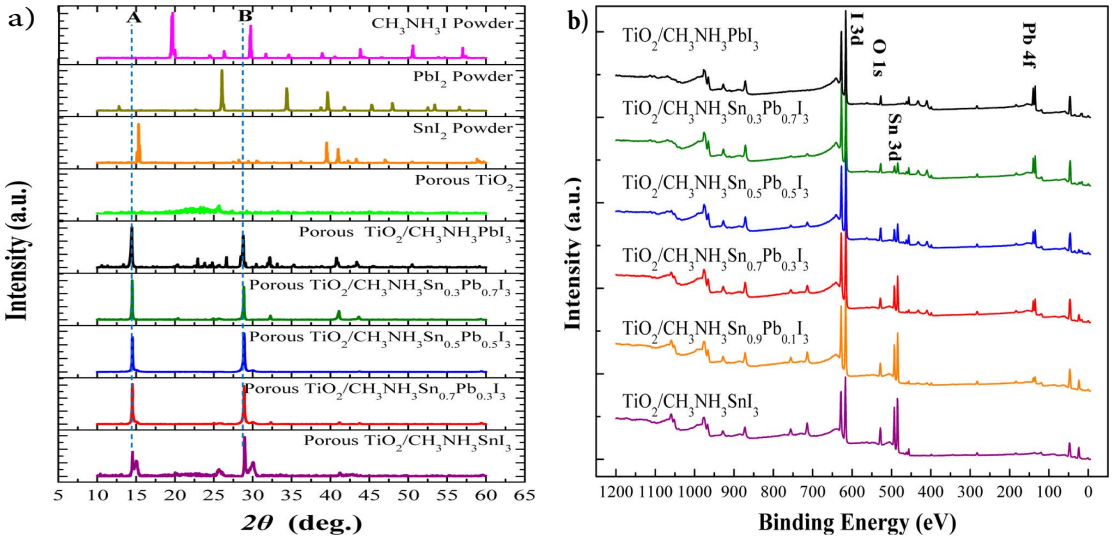

FIGURE 2.2: a) XRD patterns and b) XPS spectra of $CH_3NH_3Sn_xPb_{(1-x)}I_3$ coated on porous TiO_2 [75].

X-ray diffraction (XRD) patterns were used to characterise perovskites on the porous TiO_2 layer and its precursors in Figure 2.2-a. XRD patterns showed that the dual metal perovskite of $CH_3NH_3Sn_xPb_{(1-x)}I_3$ did not contain its precursors such as CH_3NH_3I, PbI_2, SnI_2. As for X-ray photoelectron spectroscopy (XPS) results in Figure 2.2-b, XPS graphs of $CH_3NH_3PbI_3$, $CH_3NH_3SnI_3$, and $CH_3NH_3Sn_xPb_{(1-x)}I_3$ with x ranging between 0 and 1 showed that the final composition of each perovskite was consistent with initial expected blending ratios in the chemical structures. For example, the chemical structure of $CH_3NH_3Sn_{0.7}Pb_{0.3}I_3$ was obtained as $CH_3NH_3Sn_{0.74}Pb_{0.26}I_{2.27}$ [75].

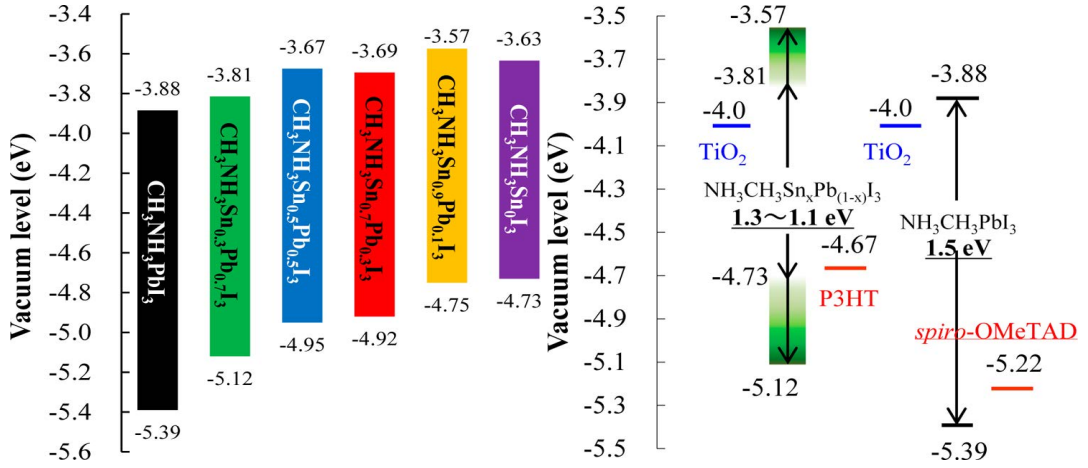

FIGURE 2.3: Energy diagrams of $CH_3NH_3Sn_xPb_{(1-x)}I_3$, titania, P3HT, spiro-OMeTAD [75].

In Figure 2.3, the energy diagrams of the Sn/Pb dual metal perovskite demonstrated that the valence band changed from -5.12 to -4.73 eV, while the conduction band shifted from -3.81 to -3.63 eV when x was changed from 0.3 to 1. From the comparison

of the energy band diagram between $CH_3NH_3Sn_xPb_{(1-x)}I_3$ and HTLs, P3HT was selected as HTL because the valence bands of the perovskite were deeper than the valence band of P3HT, -4.67 eV, whereas the valence band of spiro-OMeTAD, -5.22 eV, was deeper than the perovskite valence band. As for ETL, titania was used since the conduction band range of the perovskite was shallower than the conduction band of titania, -0.4 eV [75].

On the other hand, Hao et al. examined the performance of Pb/Sn perovskites material with the structure of $CH_3NH_3Sn_xPb_{1-x}I_3$ by using spiro-OMeTAD and its additives as HTL [76]. Although Ogomi et al. suggested poly(3-hexylthiophene-2,5-diyl) (P3HT) as the proper hole transport layer with dual metal perovskite solar cells, Hao et al. showed that spiro-OMeTAD was also suitable as HTL for $CH_3NH_3Sn_xPb_{1-x}I_3$ perovskite solar cells. It was found that in the energy band gap of the dual metal Pb/Sn perovskite, the linear trend (Vegard's law) was not observed between two extremes of 1.55 and 1.35 eV. The perovskite had a lower bandgap of $<$1.3 eV. Thus, absorption shifted to the near-infrared region. The highest short-circuit current, 20.64 mA.cm^{-2}, and the broadest light absorption, almost 1050 nm, was obtained when x was chosen as 0.5 in the perovskite of $CH_3NH_3Sn_{1-x}Pb_xI_3$ [76].

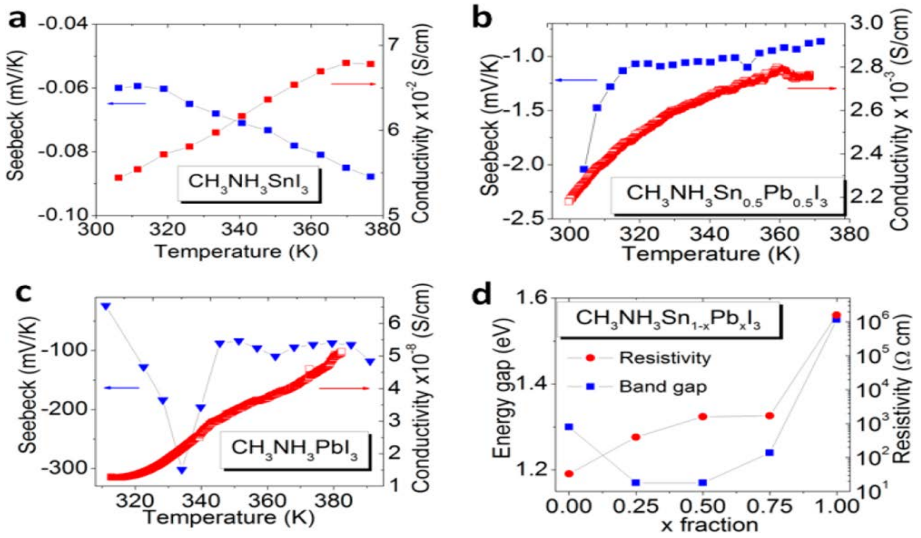

FIGURE 2.4: Conductivity, Seebeck coefficients, energy band gap and resistivity figures of $CH_3NH_3Sn_{1-x}Pb_xI_3$ solid solutions [76].

The conductivity of all perovskites increased when the temperature increased, which proved all was semiconductor in Figure 2.4. Additionally, the energy band gaps were between 1.15-1.55 eV. Seebeck coefficient measurements showed that all compositions n-type semiconductors, and the Seebeck coefficient dramatically decreased while the x value in $CH_3NH_3Sn_{1-x}Pb_xI_3$ was increasing. The irregular pattern was observed in resistivity, although a linear trend was expected according to Vegard's law [76].

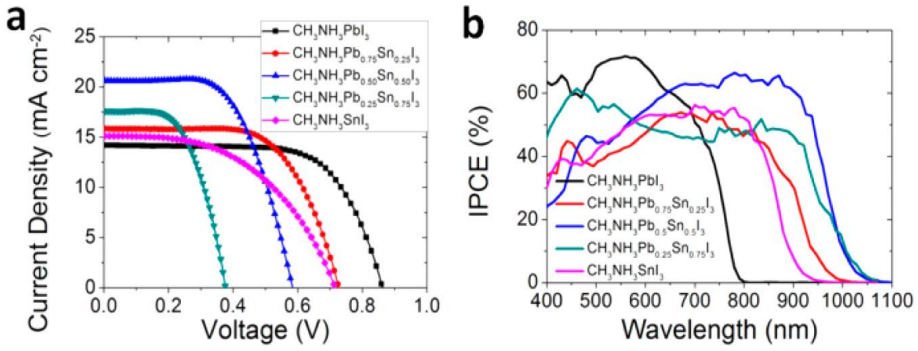

FIGURE 2.5: Photocurrent density-voltage characteristics and corresponding IPCE spectra for $CH_3NH_3Sn_{1-x}Pb_xI_3$ solar cells [76].

In Figure 2.5, the photovoltaic characteristics of the solar cells prepared using $CH_3NH_3Sn_{1-x}Pb_xI_3$, spiro-OMeTAD and its additives were demonstrated [76]. In Figure 2.5 (a), the J-V curves of the perovskites with different x values showed that the device with lead-free perovskite of $CH_3NH_3SnI_3$ performed J_{sc} of 15.18 mA.cm^{-2}, V_{oc} of 0.716 V, FF of 50.07%, and PCE of 5.44%. It was claimed that soup-like compositions of additives, lithium bis(trifluoromethylsulfonyl)imide salt and 4-tert-butylpyridine, were not suitable for Sn perovskites because they were too reactive, which made the perovskite devices non-functional or unstable [76].

The incident photon-to-electron conversion efficiency (IPCE) curves covered visible and infrared spectrum up to 1050 nm for the $CH_3NH_3Sn_{1-x}Pb_xI_3$ perovskites in Figure 2.5 (b) [76]. A decrease in the energy band gap induced a broader wavelength of absorption edge, which was observed from the shift of IPCE edges. The IPCE edge was 950 nm for the perovskite of $CH_3NH_3SnI_3$ with the energy band gap of 1.30 eV, whereas the edge shifted near-infrared region around 1050 nm for $CH_3NH_3Sn_{0.75}Pb_{0.25}I_3$ and $CH_3NH_3Sn_{0.50}Pb_{0.50}I_3$ with the band gap of 1.17 eV. All perovskites with Sn had higher IPCE edge than 800 nm, which was the limit for $CH_3NH_3PbI_3$ perovskites [76].

2.3.2 Mixed Perovskites

It is possible to create a perovskite solar cell by incorporating two different perovskite materials to increase performance and stability. In this section, we have discussed several studies in which mixed perovskites consisting of $FAPbI_3$ and $MAPbBr_3$ have been examined.

In 2015, Jeon et al. fabricated a bilayer solar cell by combining $MAPbBr_3$ and unstable $FAPbI_3$ [77]. It was found that the incorporation of $MAPbBr_3$ into $FAPbI_3$ stabilised the perovskite phase of $FAPbI_3$ and improved the power conversion efficiency (PCE). The molar ratio (x) dependence on the performance of mixed perovskite structured as $(FAPbI_3)_{1-x}(MAPbBr_3)_x$ with x ranging between 0 and 0.3, was examined.

Additionally, phase stability, the morphology of the perovskite layer and hysteresis in current-voltage characteristics as a function of chemical composition were demonstrated [77].

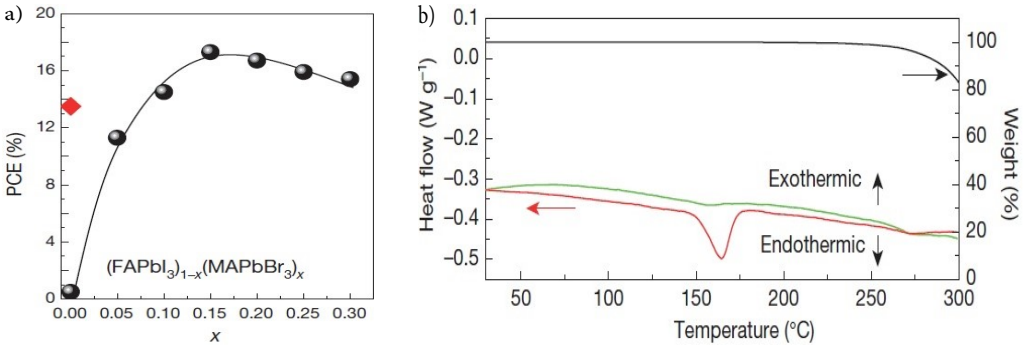

FIGURE 2.6: a) PCE values for $(FAPbI_3)_{1-x}(MAPbBr_3)_x$ perovskite devices annealed at 100 ^{o}C for 10 min and b) DSC and thermogravimetric curves of yellow $FAPbI_3$ [77].

In Figure 2.6-(a), PCEs of $(FAPbI_3)_{1-x}(MAPbBr_3)_x$ were obtained by using the average of backward scan sweep (from V_{oc} to J_{sc}) and forward scan sweep (from J_{sc} to V_{oc}) for different x values between 0 and 0.30. The solar cells were heated at 100 ^{o}C before the J-V measurements were taken for the PCEs calculation. When x was equal to 0 in $(FAPbI_3)_{1-x}(MAPbBr_3)_x$, although the J_{sc}, V_{oc}, FF, and PCE values were too low at 100 ^{o}C, the values considerably increased at 150 ^{o}C, which were 1.10 mA.cm^{-2}, 0.88 V, 0.51, and 0.5% for the former, and 22.0 mA.cm^{-2}, 0.88 V, 0.7, and 13.5% for the latter, respectively. It showed that $FAPbI_3$ demonstrated good perovskite characteristics at high temperatures. The highest efficiency of the perovskite was obtained as 17.3% with J_{sc} of 22.0 mA.cm^{-2}, V_{oc} of 1.08 V and FF of 0.73 when x was equal to 0.15 [77].

Differential scanning calorimetry (DSC) (heat and temperature relationship) and thermogravimetric (mass and temperature relationship) analysis of the yellow $FAPbI_3$ were completed to probe the phase change in Figure 2.6-(b). It was observed that, at around 160 ^{o}C, there was an endothermic peak without any weight loss, which was not seen until the temperature was above 250 ^{o}C. That means phase change occurred from yellow non-perovskite to black perovskite at around 160 ^{o}C. It was observed that the phase change was reversible as the black phase turned into the yellow phase after it was put in ambient conditions for ten days. Therefore, the yellow phase $FAPbI_3$ affected the perovskite performance [77].

On the other hand, Correa Baena et al. revealed the impact of discrete compact electron selective layer (ESL) for a mixed perovskite solar cell of $(FAPbI_3)_{0.85}(MAPbBr_3)_{0.15}$ and $MAPbI_3$ [78]. The configuration of the devices was FTO/compact metal oxide/perovskite /spiro-MeOTAD/gold. The planar ESLs of SnO_2, TiO_2 and Nb_2O_5 were used since planar electron selective layers facilitate the production of perovskite solar cells in large-scale compared to mesoporous

counterparts. The low-temperature atomic layer deposition (ALD) method was used to deposit the ESL with 15 nm thickness onto FTO glass. According to X-ray photoelectron spectroscopy (XPS) results of TiO_2 and SnO_2 deposition as ESLs on the FTO substrates, they were covered entirely with TiO_2 or SnO_2 without any pinholes and contamination. The mixed perovskite was deposited on the ESL by spin-coating [78].

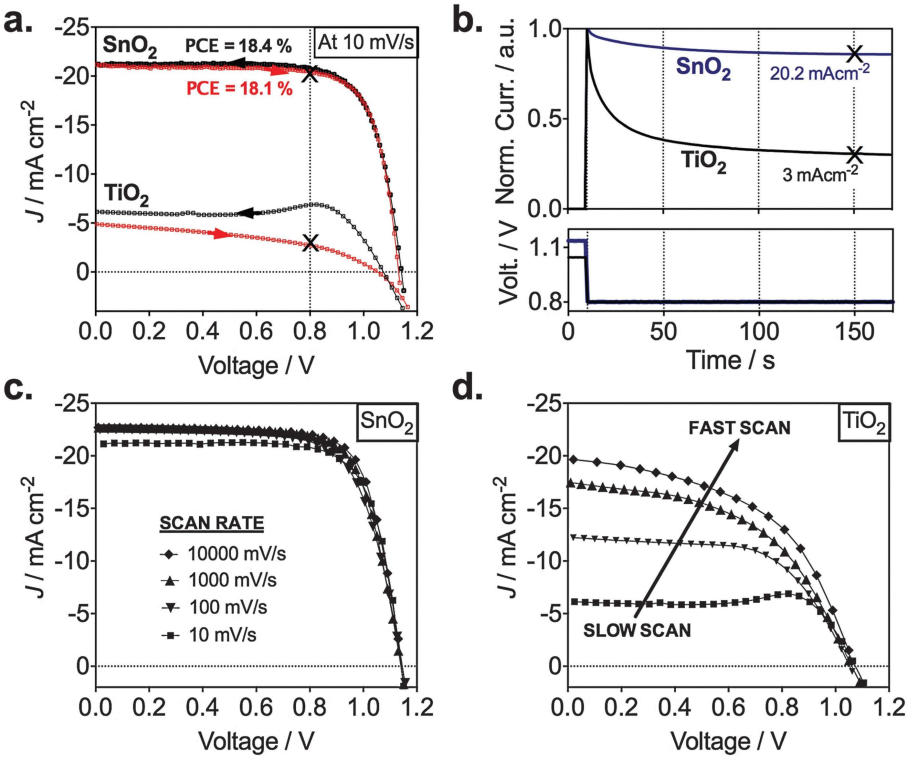

FIGURE 2.7: a) Current-voltage curves of TiO_2 and SnO_2-based mixed perovskite solar cells measured from backward (black) and forward (red) scan b) Normalised transient photocurrents obtained from V_{oc} to the maximum power point voltage for both cells c) Scan rate characteristics of the SnO_2 and d) TiO_2-based cells [78].

To analyse the electronic properties of the mixed cells with TiO_2 and SnO_2 ESL, J-V curves were examined in Figure 2.7. The open circuit voltages of both devices with TiO_2 and SnO_2 were around 1.14 V. Some of the devices prepared with SnO_2 achieved the V_{oc} of 1.19 V, which was close to the thermodynamic maximum V_{oc} of approximately 1.32 V, meaning good charge selectivity and low charge recombination [78].

Though the cell with TiO_2 showed strong hysteresis between the reverse and forward scanning in Figure 2.7-(a), the device with SnO_2 demonstrated hysteresis free pattern, meaning charge collection was independent of voltage. The differences between forward and backward scanning were observed using transient photocurrents measured at 0.8 V, yielding maximum power. After $\sim$ 50 s, a steady photocurrent was obtained for the two devices when the voltage changed from the open circuit voltage

to 0.8 V. Yet, until 50 s, the photocurrent of SnO_2 device dropped just 10% from 23 to 20.2 mA.cm^{-2} whereas the current of the device with TiO_2 decreased 70% from 10 to 3 mA.cm^{-2}. The stabilised current of the solar cell with SnO_2, 20.2 mA.cm^{-2}, corresponded with the open circuit current, 20.7 mA.cm^{-2}, obtained from the J-V curve [78].

To understand the phenomena behind the hysteresis of TiO_2 based device, J-V graphs of both devices were obtained choosing different voltage scan rates in Figure 2.7. Only backward scanning was operated, which was obtained the device was preconditioned at 1.12 V for 10 s. When the sweep rate changed from 10 mV/s to 10 V/s, the device with SnO_2 had a slight increase in current density, reaching its maximum value of 23 mA.cm^{-2}, while J_{sc} of the device with TiO_2 significantly increased from 5 mA.cm^{-2} to 20 mA.cm^{-2}. That meant the light absorption and photocurrent generation in the perovskite material was the same as the perovskite/SnO_2 configuration. However, low charge collection of TiO_2 based cells for low scan sweep was observed. Additionally, Nb_2O_5 was used as ESL with the mixed perovskite solar cell, but it showed considerable hysteresis and low photocurrent density like the device with TiO_2 [78].

In 2017, Yang et al. introduced a perovskite solar cell with an efficiency of 22.1% by adding extra I_3^- ions into the mixed perovskite consisting of $FAPbI_3$ and $MAPbBr_3$ [79]. To obtain a perovskite with high performance, it is important to avoid defects along with the preparation of dense and uniform thin layers on the substrates because defects cause a reduction in open circuit voltage and short circuit current, which contribute to the device performance [79].

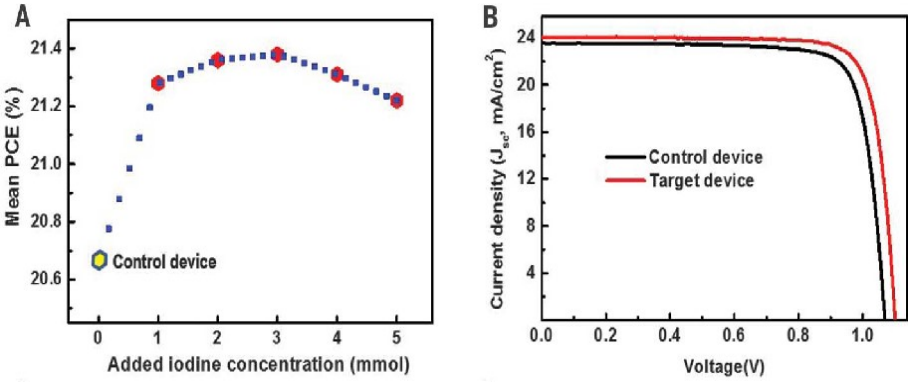

FIGURE 2.8: A) Power conversion efficiencies as a function of different iodide concentrations B) J-V curves for the control and target devices [79].

Two types of devices were prepared to observe the difference between the devices with and without additional triiodide ions, I_3^-, which were called target and control device, respectively [79]. In Figure 2.8, the PCE results were shown according to different concentrations of I_3^-. The solar cell with max efficiency was obtained from the target device when the dripping solution included 3 mmol I_3^-. V_{oc}, J_{sc}, FF and PCE

of the target device was 1.1 V, 24.1 mA.cm^{-2}, 81.9% and 21.6%, whereas the values of the control device were 1.07 V, 23.5 mA.cm^{-2}, 80.8% and 20.3%, respectively. It was claimed that the increase of J_{sc} stemmed from improving light harvesting capacity, not increasing charge collection since the device thickness and surface morphologies of the target and control devices were identical. The improvement in J_{sc} and FF showed enhancement in crystallinity and reduction in trapping sites, which were responsible for nonradiative charge recombination [79].

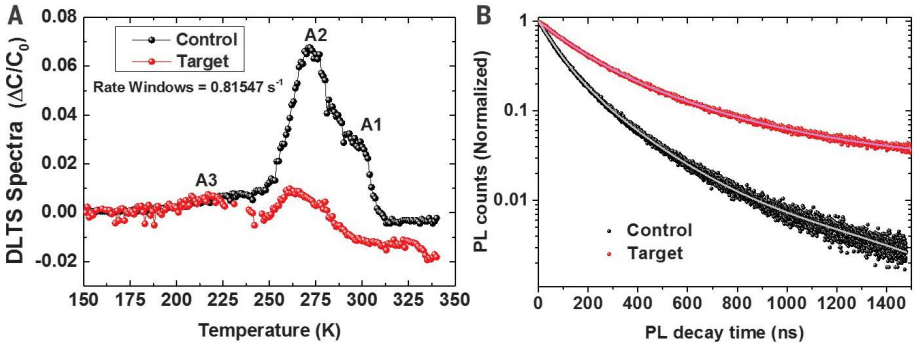

FIGURE 2.9: A) Deep-level transient spectroscopy spectra for the control and target perovskite layers B) Time-resolved photoluminescence decay curves for the control and target layers emitted at $\lambda = 825\ nm$ with the biexponential fitting [79].

Deep-level transient spectroscopy (DLTS) and steady-state and time-resolved photoluminescence (PL) were used to analyse the defects deeply in Figure 2.9. From the DLTS spectra, three defect levels were captured, namely A1, A2 and A3. In the target layer, the A1 signal did not exist anymore, which meant the A1 level defects were overcome straightforwardly. Additionally, the defect concentration of A2 level was reduced from 5.28 $\times$ 1014 cm^{-3} to 8.81 $\times$ 1013 cm^{-3} by the addition of I_3^- [79].

As for photoluminescence (PL) results in Figure 2.9, PL decay was measured by time-correlated single-photon counting. It was suggested that the short PL lifetime originated from defect-induced non-radiative recombination whereas the long PL lifetime resulted from radiative recombination. It was obtained that the target layer and the control layer of PL lifetime and carrier lifetime were $\sim$ 138 ns and $\sim$ 1105 ns, and $\sim$ 72 ns and $\sim$ 228 ns, respectively. The longer PL lifetime of the target device, $\sim$ 138 ns, indicated a lower number of defects and higher crystallinity in the device morphology [79].

2.4 Perovskite Studies with DFT

DFT is a useful tool to analyse matter in terms of structural, chemical, optical, spectroscopic, elastic, vibrational and thermodynamic properties [33]. In this section,

several studies on perovskites using the first principles DFT calculations have been examined.

The energetics of three organic cations of ammonium (NH_4^+), methylammonium, (CH_3NH_3) and formamidinium ($NH_2CHNH_2^+$) in lead iodide perovskite structure were studied by using PBEsol exchange-correlation functional implemented in VASP package [80]. It was shown that adjustment in dipole moment affected ferroelectric behaviour and dielectric constant. Additionally, the changes in the cation size of the perovskite influenced the energy band gap and ferroelectric property. It was also suggested to use an aprotic cation to avoid a degradation pathway [80].

Electronic properties of $CH_3NH_3PbI_3$ were examined using DFT [81]. The PBE was chosen as the exchange-correlation functional, and CASTEP was used as the computer program. The Brillouin zone k-point grid sampling was taken as $4 \times 4 \times 4$. Electronic band structure and density of states of the perovskite were obtained in addition to the x-ray diffraction graph (XRD). The energy band gap between the conduction band minimum and valance band maximum was calculated as 1.43 eV, while the band gap was obtained as 1.51 eV according to the Kubelka-Munk spectrum from experiments. The energy band gap difference between experimental and computational results originated from an underestimation of the band gap by GGA XC functional [81].

However, it was achieved that the energy band difference between experimental and computational results was overcome [82]. Electronic structure and defect calculations of $CH_3NH_3PbI_3$ were performed using VASP code [82]. The electronic structure calculations were based on the unit cell of the perovskite, whereas the defect calculations were obtained from a $3 \times 3 \times 3$ supercell with Γ point. VASP code with standard frozen-core projector augmented-wave (PAW) was used for the first principle DFT calculations. GGA was selected as exchange-correlation functional, and 400 eV was taken as cut-off energy for basis functions. Spin-orbital coupling (SOC) was not included in the calculations since energy band gap underestimation from the computational results was eliminated when GGA was used with non-SOC. Therefore, the energy band gap of the $CH_3NH_3PbI_3$ was found to be 1.5 eV [82].

As for defects in the perovskite of $CH_3NH_3PbI_3$, it was found that the dominant defects were p-type V_{Pb} and n-type MA_i, where 'V' and 'i' represented vacancy and interstitial, respectively[82]. It was shown that shallow-level defects were observed when the formation energy was low, while deep-level defects were created in the case of high formation energy. Unusual defect properties were explained by the strong Pb lone-pair s orbital and I p orbital antibonding coupling in addition to the high ionicity of the perovskite [82].

2.5 Degradation Issue of Perovskite Solar Cells

Perovskite crystallographic stability and structure are defined by the Goldschmidt tolerance factor, t, and octahedral factor, κ, given by: [32].

$$t = \frac{R_A + R_X}{\sqrt{2}\,(R_B + R_X)} \qquad \kappa = \frac{R_B}{R_X} \tag{2.1}$$

where R_A and R_B are ionic radii of cation A and B, and R_X is the radius of anion X in the ABX_3 perovskite structure. R_A should be between $\sim$ 1.60 A^o and $\sim$ 2.50 A^o to construct perovskite [83]. Additionally, the material is classified as perovskite once $0.825 < t < 1.059$ and $0.414 < \kappa < 0.732$ are provided [23]. A perovskite crystal structure is mostly cubic in case t is in the range of 0.9-1.0, whereas distorted perovskite is formed for t with the values of 0.80-0.89, which is named octahedral tilting [84]. On the other hand, a non-perovskite structure is obtained when $t < 0.8$ and $1.0 < t$ [22].

The chemical stability of materials can vary from one material to another. In the metal part of the perovskite structure, the most used metals, Pb, Sn and Ge, show different stability even if they belong to the same metal group [85]. Pb-based perovskites have good stability towards the air for months, whereas they are prone to degrading by humidity. On the other hand, Sn-based perovskites are air and humidity sensitive owing to the oxidation of Sn^{2+} to Sn^{4+} in air [86]. Formation of Sn^{4+} causes self-doping in the material because it behaves p-type dopant, although Sn perovskites are n-type semiconductors [74].

The combination of two different perovskite, $MAPbBr_3$ and $FAPbI_3$, stabilised the perovskite phase of $FAPbI_3$, and increased the PCE to 18% under the standard illumination of 100 mW.cm^{-2} [77]. Although the band gap of $FAPbI_3$ is lower than the band gap of $MAPbI_3$, which is suitable to obtain higher efficiency, the perovskite of $FAPbI_3$ suffers from instability. The perovskite of $FAPbI_3$ is at the black perovskite phase (α-phase) at high temperatures (above 160 ^{o}C), whereas it turns into yellow polymorph (δ-phase) at ambient conditions. It was found that the addition of $MAPbBr_3$ into $FAPbI_3$ increased the perovskite phase stability of $FAPbI_3$ [77].

The perovskite of $FA_{0.81}MA_{0.15}PbI_{2.51}Br_{0.45}$ reached 20.5% efficiency with the large aperture area solar cells, more than 1 cm^2 [59]. The devices with different preparation methods showed different stability under full sunlight illumination after 100 h. The cells produced using vacuum flash-assisting solution process maintained 90% of their initial efficiency, whereas the cells with conventional single-step solution deposition method retained 70% of the efficiency [59]. Therefore, it is supported that the preparation method of perovskite solar cells has significant importance on stability.

The two-step deposition method improved the PCE of the lead-based $CH_3NH_3PbI_3$ perovskite solar cell to 15% and provided high stability [87]. The FTO glass/TiO_2/perovskite/spiro-MeOTAD (HTM) structured solar cell was sealed in argon and exposed to 100 mW.cm^{-2} illumination from light-emitting diodes at 45 ^{o}C. The J-V curve was measured every two hours, and the PCE was calculated to compare the difference between the initial value and the value after 500 h. It was observed that the PCE of the device was conserved more than 80% after 500 h [87].

Triple cation perovskite solar cells exhibited impressive power conversion efficiency of 21.1% with high stability [88]. $MAPbI_3$, $FAPbI_3$ and $CsPbI_3$ have different issues which need to be tackled. $MAPbI_3$ cells did not achieve the efficiency above 20% in addition to their high temperature and humidity sensitivity [88]. $MAPbI_3$ degrades in moisture and produced PbI_2 at high temperatures on account of CH_3NH_3I lost [89]. On the other hand, $CsPbI_3$ is non-perovskite orthorhombic δ-phase (yellow phase) at room temperature, while it is in photoactive perovskite α phase (black phase) at temperatures above 300 ^{o}C [88]. However, the mixture of the three cations in the perovskite of $Cs_x(MA_{0.17}FA_{0.83})_{(100-x)}Pb(I_{0.83}Br_{0.17})_3$ enhanced not only the PCE to 21.1% but maintained the PCE up to 18% under illumination after 250 h at room temperature [88].

The addition of Rb^+ as the fourth component into the cation part of the lead-based perovskite provided efficient devices with high stability [90]. Rb^+ is not preferable as an A-site cation in perovskites since the tolerance factor of the perovskite of $RbPbI_3$ is not in the suitable range owing to the small ionic radius of Rb^+. Thus, $RbPbI_3$ shows only the non-perovskite yellow phase. Nonetheless, the usage of Rb^+ into the perovskite with the multiple cation part of RbCsMAFA provided stabilised efficiencies of up to 21.6%. Moreover, when the hole transfer layer changed from spiro-OMeTAD to polytriarylamine polymer (PTAA), the cell protected its efficiency, >17%, up to 95% at 85 ^{o}C under full sunlight illumination after 500 h [90].

The usage of solid hole transfer material (HTM) increased the stability of $CH_3NH_3PbI_3$ perovskite devices compared to liquid junction cells [91]. The solid-state perovskite solar cell with mesoporous TiO_2 and spiro-MeOTAD as HTM achieved 9.7% PCE efficiency with long-term stability. The device was subjected to AM 1.5G illumination at room temperature without sealing. The PCE of the device increased by about 14% from the beginning to 200 h and then almost remained stable at 9.7% after 500 h.

On the other hand, without a hole transfer layer, the solar cell with the perovskite of $(5-AVA)_x(MA)_{(1-x)}PbI_3$ achieved maintaining the PCE of 12.8% after >1000 h under full sunlight illumination at ambient air conditions [92]. The device had two mesoporous materials, TiO_2 and ZrO_2, covered by a porous carbon film as a third layer. The cell configuration was FTO-covered glass/c-TiO_2 layer/mesoscopic

TiO_2/ZrO_2/C triple layer/the perovskite/Au counter-electrode. The perovskite with the cations of methylammonium (MA) and 5-aminovaleric acid (5-AVA) was applied through the three layers scaffold by drop-casting. The resulting cell provided 12.8% efficiency and lasted without sealing under the illumination of AM 1.5G after 1008 h [92].

The selection of the electron transfer layer (ETL) and hole transfer layer (HTL) also has a significant impact on cell stability. The cell, which was produced by the selection of p-doped $Ni_xMg_{1-x}O$ as HTL and n-doped TiO_x as ETL with $MAPbI_3$-PCBM film, maintained >90% of its initial PCE, >15%, under the illumination of AM-1.5 sunlight after 1000 h [58]. The device was designed as FTO glass/$Li_{0.05}Mg_{0.15}Ni_{0.8}O$/perovskite/PCBM/$Ti_{0.95}Nb_{0.05}O_x$ /Ag. The air-stable layer of $Ti_{0.95}Nb_{0.05}O_x$ protected the perovskite from humidity and prevented it from degradation [58].

Another study on the perovskite solar cell in terms of high stability was conducted using p-type NiO_x and n-type ZnO [64]. The cell, which was prepared by the cell structure of ITO glass/$NiO_x/CH_3NH_3PbI_6/ZnO$/Al, maintained about 90% of initial PCE of 16.1% after 60 days in the air with 30-50% humidity at room temperature without encapsulation. The metal oxide ZnO separated the perovskite and Al layer and saved the perovskite from degradation [64].

Chapter 3

Methodology

3.1 The First-principle Calculations for $Cs_3Bi_2I_9$ and $Cs_3Bi_2Br_9$

Bi-based perovskites are promising materials to use as light absorbers in solar cells because they provide higher stability and lower toxicity compared to lead-based counterparts. In this study, two inorganic Bi-based perovskites, $Cs_3Bi_2I_9$ and $Cs_3Bi_2Br_9$, have been investigated in terms of their structural, electronical, and optical properties using first-principles calculations with CASTEP.

DFT was utilised to investigate crystal structures, electronic band gaps, density of states and absorption coefficients of $Cs_3Bi_2I_9$ and $Cs_3Bi_2Br_9$ using CASTEP. The first principle DFT calculations were conducted using the exchange correlation function of Perdew-Burke- Ernzerhof formalism for solids (PBEsol). The cut-off energy of plane wave basis and k-point Monkhurst-Pack (MP) grid for Brillouin zone sampling were chosen as 350 eV and $7 \times 7 \times 5$, respectively [93]. Atomic positions in the unit cells of the Bi-based perovskites, which were produced using single-crystal diffractometry, absorption correction and least-squares refinement, were employed [94], [95]. Crystal structures of the perovskites were simulated by employing Jmol and VESTA (Visualisation for Electronic and Structural Analysis) after geometric optimisation was applied on the unit cell structures. Additionally, electronic density of states, joint density of states and absorption coefficients calculations were investigated using OptaDOS, which is a post-processing tool for CASTEP [96].

3.2 Production of $Cs_3Bi_2Br_xI_{9-x}$ Solar Cells

The Bi-based perovskite solar cells were produce using $c\text{-}TiO_2$, $Cs_3Bi_2Br_xI_{9-x}$ (x is varying from 0 to 9), spiro-MeOTAD, and Au as the ETM, light absorber, HTM and

counter electrode, respectively. The synthesis of the precursor materials and the production procedure of the solar cells were given in the following sections.

3.2.1 Synthesis of the bi-based perovskites

CsI (99.999%, Sigma-Aldrich), BiI_3 ($\geq$99.998%, Sigma- Aldrich), $CsBr$ (99.999%, Sigma-Aldrich), $BiBr_3$ (99.998%, Sigma-Aldrich) and DMF (anhydrous, 99.8%, Sigma-Aldrich) were used to produce perovskite solutions without further purification.

Figure 3.1 demonstrates the $Cs_3Bi_2I_9$, $Cs_3Bi_2Br_9$, BiI_3 and $BiBr_3$ solutions. The solutions were prepared in 20 mmol/L concentrations and then diluted to 10 mmol/L shown in glass bottles and quartz cuvettes, respectively. All 20 mmol/L solutions were prepared by mixing CsI or $CsBr$ with the related Bi-halide salts in DMF (10 ml) at 70 ^{o}C for 24 h. The amounts used were given in Table 3.1. CsI (0.1558 g) and BiI_3 (0.2358 g) were mixed in DMF (10 ml) at 70 ^{o}C for 24 h to obtain $Cs_3Bi_2I_9$ (20 mmol/L) [19]. The Bi-halide salt solutions were prepared by solving BiI_3 (0.2358 g) in DMF (10 ml) and $BiBr_3$ (0.1794 g) in DMF (10 ml) in separate bottles applying the same production procedure with the perovskites.

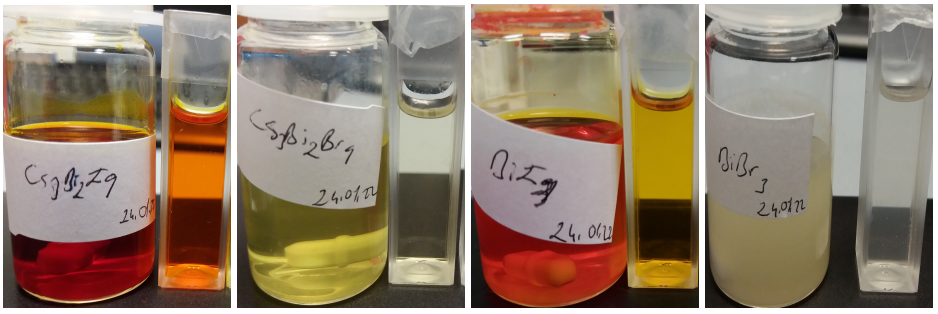

FIGURE 3.1: The solutions of $Cs_3Bi_2I_9$, $Cs_3Bi_2Br_9$, BiI_3 and $BiBr_3$ at 20 mmol/L and 10 mmol/L concentrations.

Table 3.1 gives the amounts of $BiBr_3$, BiI_3, $CsBr$ and CsI to produce $Cs_3Bi_2Br_xI_{9-x}$ perovskites (20 mmol/L) mixed in DMF (10 ml) at 70 ^{o}C for 24 h. Besides, Figure 3.2 demonstrates the images of the Bi-based perovskite solutions. From left hand side to right hand side, the order of bottles shows the x values in $Cs_3Bi_2Br_xI_{9-x}$, which is changing from 1 to 8.

Perovskites	$BiBr_3$ (g)	BiI_3 (g)	$CsBr$ (g)	CsI (g)
BiI_3	-	0.2358	-	-
$BiBr_3$	0.1794	-	-	-
$Cs_3Bi_2I_9$	-	0.2358	-	0.1558
$Cs_3Bi_2BrI_8$	-	0.2358	0.0425	0.1039
$Cs_3Bi_2Br_2I_7$	-	0.2358	0.0851	0.0519
$Cs_3Bi_2Br_3I_6$	-	0.2358	0.1276	-
$Cs_3Bi_2Br_4I_5$	0.0897	0.1179	0.0425	0.1039
$Cs_3Bi_2Br_5I_4$	0.0897	0.1179	0.0851	0.0519
$Cs_3Bi_2Br_6I_3$	0.0897	0.1179	0.1276	-
$Cs_3Bi_2Br_7I_2$	0.1794	-	0.0425	0.1039
$Cs_3Bi_2Br_8I$	0.1794	-	0.0851	0.0519
$Cs_3Bi_2Br_9$	0.1794	-	0.1276	-

TABLE 3.1: The amounts of the components to produce Bi-halide salts and $Cs_3Bi_2Br_xI_{9-x}$ perovskites in DMF.

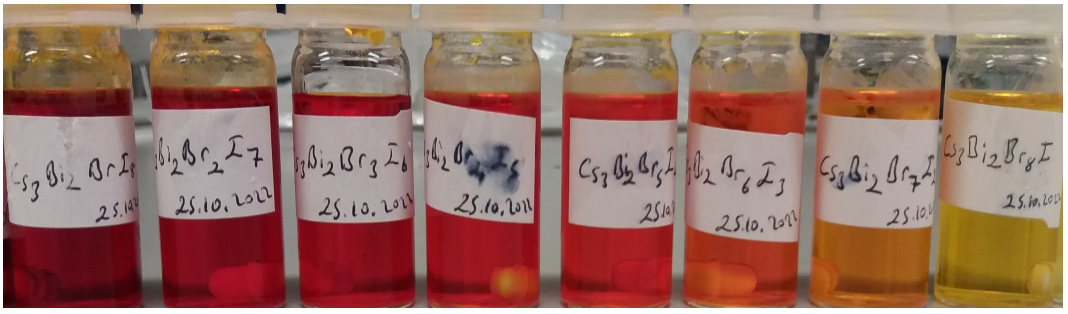

FIGURE 3.2: The images of $Cs_3Bi_2Br_xI_{9-x}$ solutions in order of x changing from 1 (the darkest red bottle) to 8 (the lightest yellow bottle).

3.2.2 Synthesis of the ETM

The c-TiO_2 was employed as the ETM to fabricate solar cells with Bi-based perovskites. Two different preparation methods were used to produce ETMs, whose ingredients were given in Table 3.2. Titanium (IV) butoxide (97 %, Sigma-Aldrich), titanium (IV) isopropoxide (97 %, Sigma-Aldrich), acetic acid (glacial, Fisher Scientific), hydrochloric acid (∼37%, Fisher Scientific), and ethanol (absolute, ≥99.8%, Fisher Scientific) were used to prepare c-TiO_2 solutions without further purification.

To prepare c-TiO_2 with titanium (IV) butoxide, firstly, acetic acid was mixed with ethanol for 5 min. Afterwards, titanium (IV) butoxide was added to the acetic solution, and then the solution was mixed for 10 min. Lastly, the clear solution was

mixed for 1 h after the drop-wise addition of deionised water. Therefore, the preparation of *c-TiO_2* was completed.

As for the recipe-2, titanium (IV) isopropoxide & ethanol (2.53 ml), and hydrochloric acid & ethanol (2.53 ml) were mixed in separate bottles on magnetic stirrers for 5 min [97]. Afterwards, the acetic solution was added to the titanium (IV) isopropoxide & ethanol solution under heavy stirring. The transparent *c-TiO_2* solution was ready to use after 30 min mixing.

ETM Recipe-1	**ETM Recipe-2**
Titanium (IV) Butoxide (4 ml)	Titanium (IV) Isopropoxide (369 μl)
Acetic Acid (4 ml)	Hydrochloric Acid (35 μl)
Deionised Water (0.75 ml)	Ethanol (5.06 ml)
Ethanol (40 ml)	-

TABLE 3.2: The amounts for preparing ETMs with two different recipes.

Figure 3.3 demonstrates the microscope images of *c-TiO_2* on ITO-glass substrates, which were produced following the procedure in Section 3.2.4. Figure 3.3-(a) shows the microscope image of the *c-TiO_2* layer fabricated using the recipe-1, whereas Figure 3.3-(b) illustrates the microscope image of the *c-TiO_2* layer from recipe-2. It was observed that the surface coverage of the *c-TiO_2* layer with recipe-2 was smoother and more uniform compared to the other. The *c-TiO_2* layer with recipe-2 had some roughness and accumulated particles at some regions on the ITO-glass substrate. Thus, it was suggested to use the *c-TiO_2* solution produced from recipe-2.

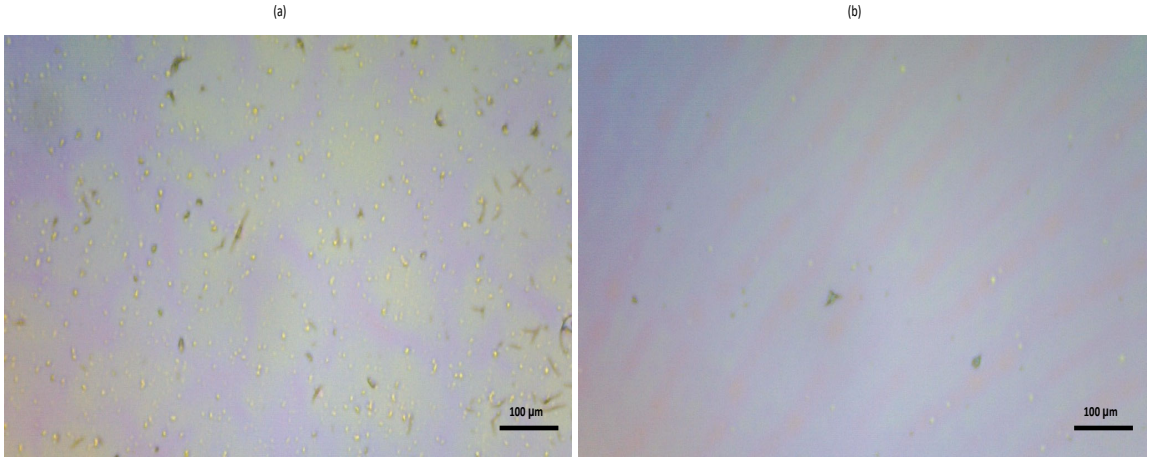

FIGURE 3.3: Microscope images of *c-TiO_2* from recipe-1 (a) and recipe-2 (b) on ITO-glass substrates

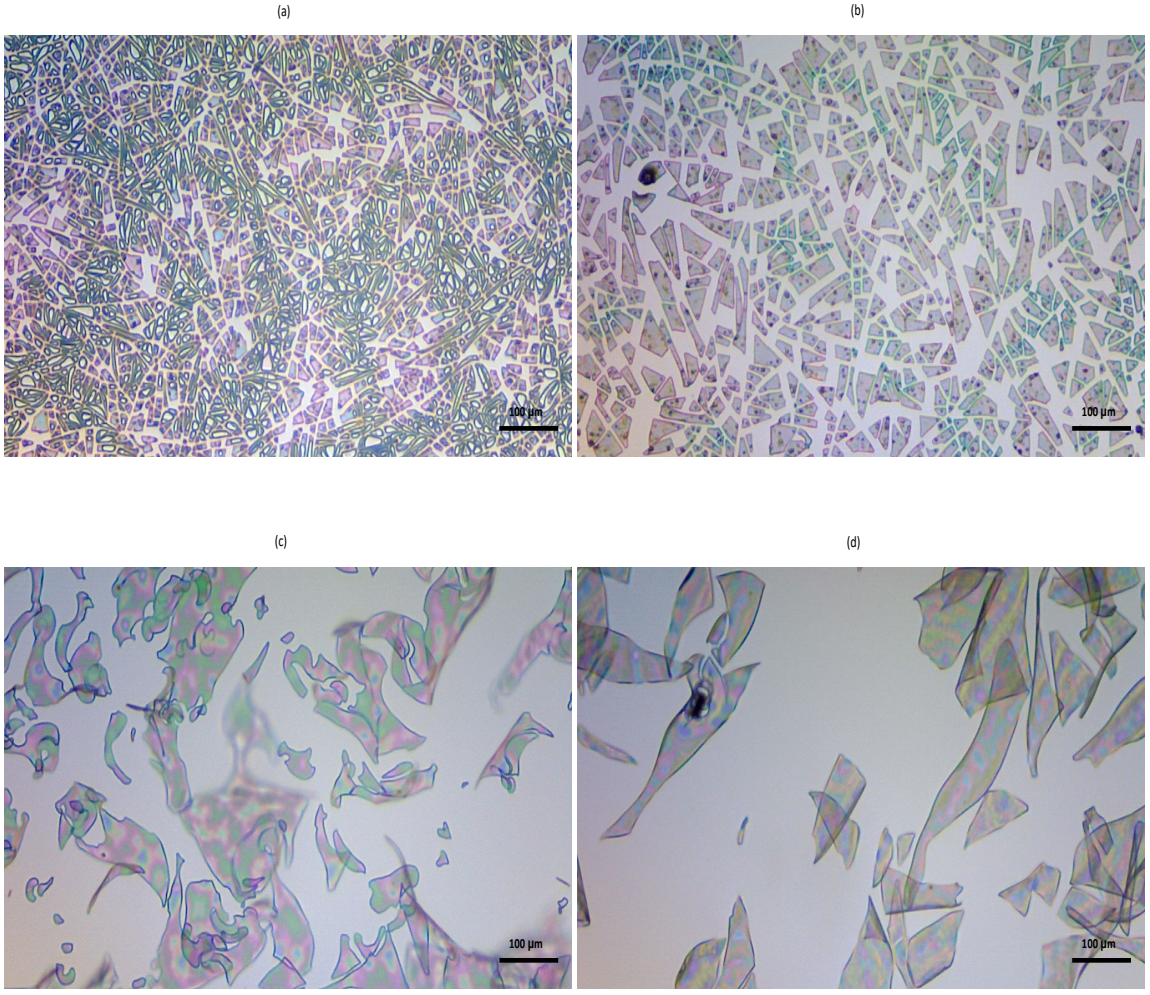

FIGURE 3.4: Microscope images of the two-layers c-TiO_2 from recipe-1 (a), from recipe-2 (c), and the three-layers c-TiO_2 from recipe-1 (b), from recipe-2 (d)

Figure 3.4 shows the microscope images of the two-layers and three-layers c-TiO_2 from recipe-1 and recipe-2 on ITO-glass substrates. The two-layers and three-layers c-TiO_2 substrates were produced by coating c-TiO_2 solution on the ITO-glass substrates twice and three times applying sequential spin-coating procedure in Section 3.2.4. After one layer was deposited, the other layer was coated using the same spin-coating process. After the two or three layers were coated on the substrates, the substrates were placed in a furnace for annealing by employing the procedure in Section 3.2.4.

Figure 3.4-(a) demonstrates the microscope image of the two-layers c-TiO_2, while Figure 3.4-(b) illustrates the microscope image of the three-layers c-TiO_2 produced using recipe-1. Besides, Figure 3.4-(c) and Figure 3.4-(d) demonstrate the microscope image of the two-layers and three-layers c-TiO_2 produced using recipe-2, respectively. It was observed that the surface roughness increased with the increasing number of layers. Additionally, accumulations of the particles on the surface of the substrates

significantly increased. Therefore, it was suggested to apply one layer *c-TiO_2* on the ITO-glass substrates as ETMs.

3.2.3 Synthesis of the HTM

Spiro-MeOTAD was employed as the HTM to fabricate perovskite solar cells. The spiro-MeOTAD solution was prepared using spiro-MeOTAD (Sigma-Aldrich), bis(trifluoromethane)sulfonimide lithium salt (99.95%, trace metals basis, Sigma-Aldrich), acetonitrile (anhydrous, 99.8%, Sigma-Aldrich), 4-tert-Butylpyridine (Sigma-Aldrich), chlorobenzene ($\geq$99.5%, Sigma-Aldrich) without further purification.

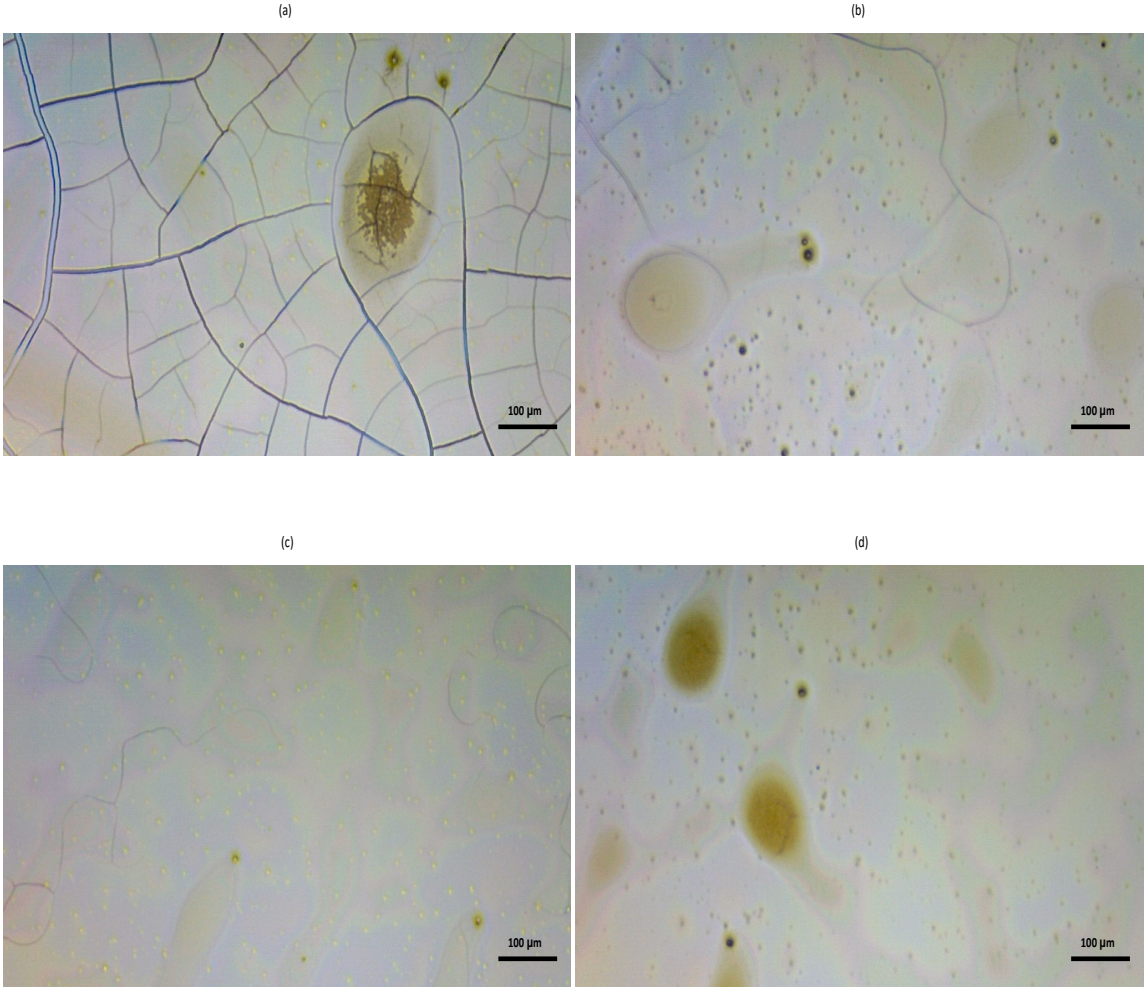

FIGURE 3.5: Microscope images of the spiro-MeOTAD layer produced using 2000 rpm (a), 3000 rpm (b), 4000 rpm (c), and 4000 rpm heated at 120 ^{o}C (d).

The spiro-MeOTAD solution was comprised of spiro-MeOTAD (72.3 mg), chlorobenzene (1 ml), 4-tert-butylpyridine (28.8 μl), and lithium salt solution (17.5 μl), which was prepared by dissolving bis(trifluoromethane)sulfonimide lithium salt (520

mg) in acetonitrile (1 ml) [98]. The solution was mixed on a magnetic stirrer for 30 min to obtain a clear yellowish solution.

Figure 3.5 shows the microscope images of the spiro-MeOTAD layers on ITO-glass substrates, which were fabricated applying different spinning speeds. The ITO-glass substrates were coated with spiro-MeOTAD using spin-coating at 2000 rpm, 3000 rpm and 4000 rpm, whose microscope images are shown in Figure 3.5-(a), Figure 3.5-(b) and Figure 3.5-(c), respectively. It was observed that the spiro-MeOTAD coated substrate at 4000 rpm provided the optimum surface coverage of the HTM, whereas the substrate coated at 2000 rpm had a surface with many cracks. Additionally, it was observed that the spiro-MeOTAD surface deteriorated when the coated substrate was heated at 120 ^{o}C after the spin-coating process. The damaged surface microscope image of the heated substrate after spin-coating at 4000 rpm is given in Figure 3.5-(d). Therefore, the HTLs at perovskite solar cells were formed using 4000 rpm without heating.

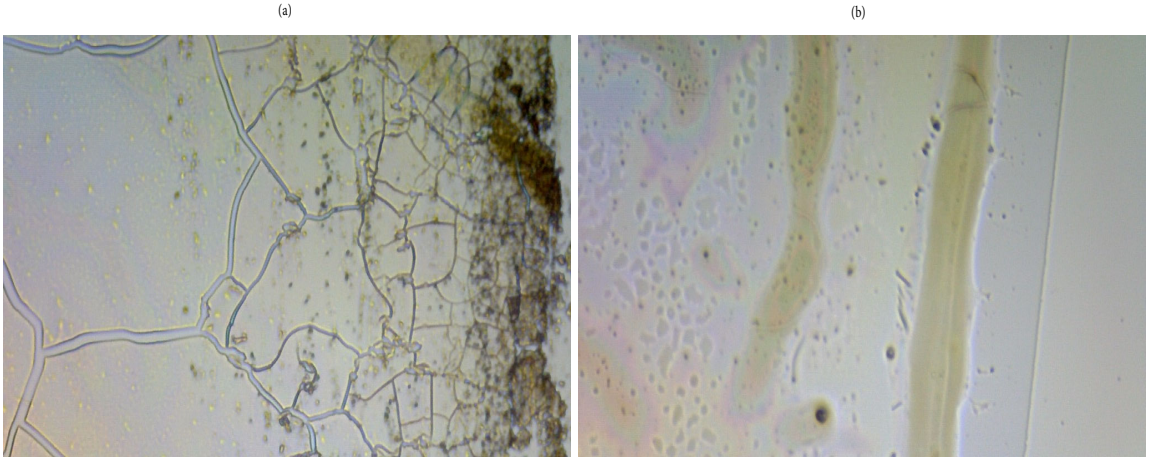

FIGURE 3.6: Microscope images of the spiro-MeOTAD edges cleaned with a cotton bud (a) and taped (b).

Figure 3.6 shows the microscope images of the edges of spiro-MeOTAD layers, which were cleaned with a cotton bud and taped. The cotton bud cleaning process severely damaged the HTL and caused many cracks at the surface shown in Figure 3.6-(a). However, the edge of the spiro-MeOTAD layer, whose substrate was taped before the spin-coating process, was smoothly cleaned by pulling out the tape after the spin-coating process in Figure 3.6-(b). Hence, the electrodes of the solar cells were protected from contamination during the coating processes by using tapes.

3.2.4 Production of the Bi-based perovskite solar cells

The pre-patterned ITO-glass substrates (20×15 mm, Ossila) were used to prepare the Bi-based solar cells after cleaning. Figure 3.7 shows the schematic diagram of a

ITO-glass substrate, where the yellow parts are indium tin oxide coated glass whereas the other parts are bare glass. The substrates were sequentially cleaned with a commercial detergent (Teepol multi-purpose), deionised water, acetone (Sigma-Aldrich), isopropanol (≥99.5%, Fisher Scientific), and ethanol (absolute, ≥99.8%, Fisher Scientific) in an ultrasonic bath for 15 min, and then dried with nitrogen [99, 100].

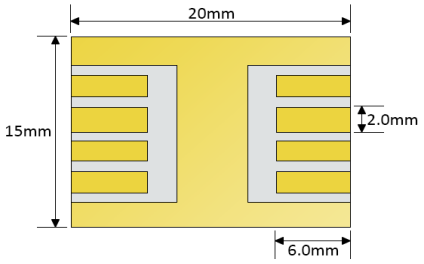

FIGURE 3.7: Schematic diagram of pre-patterned ITO-glass substrates

The Bi-based solar cells were constructed using n-i-p configuration and thereby the structure of the cells were designed as ITO-glass/ETM/perovskite/HTM/counter electrode. The solar cell architecture of ITO-glass/c-TiO_2/$Cs_3Bi_2Br_xI_{9-x}$/ spiro-MeOTAD/Au was used in the production of the Bi-based solar cells. The preparation method of the precursors can be found in Section 3.2.1, Section 3.2.2 and Section 3.2.3.

First, the c-TiO_2 solution (15 μl) was coated on the clean ITO-glass substrate using spin-coating method at 2000 rpm for 30 s. Then, the c-TiO_2 coated ITO-glass substrate was annealed in a furnace at 500 ^{o}C with the set point ramp rate of 5 ^{o}C/min for 30 min [101].

The light absorber perovskite layer was coated on the c-TiO_2 layer using spin-coating method at 2000 rpm for 30 s, and then the coated substrate was annealed on a hot plate at 120 ^{o}C for 15 min. However, a uniform film coverage of the perovskite layer was not obtained using perovskite solutions at room temperature. Figure 3.8-(a) and Figure 3.8-(c) shows the microscope images of the $Cs_3Bi_2Br_9$ and $Cs_3Bi_2I_9$ thin films, which were produced using the related perovskite solutions at room temperature. The images show discontinuity of the film coverage. However, the perovskite solutions were heated at 70 ^{o}C before coating, the film coverage was improved shown in Figure 3.8-(b) and Figure 3.8-(d). Yet, there were still some discontinuities in the film coverage and some accumulations of the perovskites at specific regions on the film.

The smooth, continuous, and uniform coverage of the Bi-based perovskite thin films were obtained using the following procedure. Firstly, the c-TiO_2 coated ITO-glass substrates were heated on a hot plate at 120 ^{o}C for 20 min. The perovskite solutions

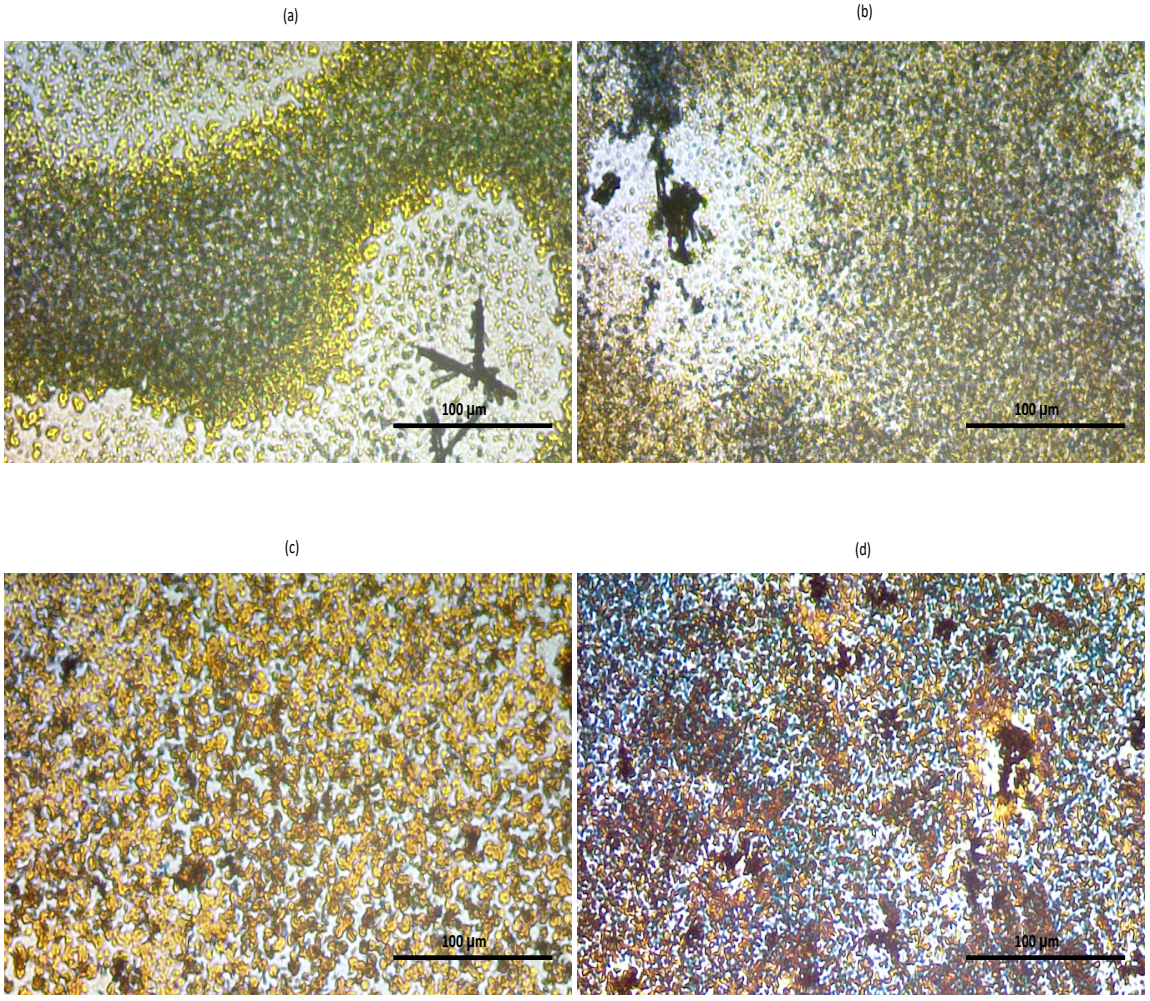

FIGURE 3.8: Microscope images of perovskite layers from the solutions of a) $Cs_3Bi_2Br_9$ at room temperature, b) $Cs_3Bi_2Br_9$ at 70 ^{o}C, c) $Cs_3Bi_2I_9$ at room temperature, d) $Cs_3Bi_2I_9$ at 70 ^{o}C.

were also mixed and heated at 70 ^{o}C for 30 min. Afterwards, the heated ITO-glass were coated with the heated perovskite solution (15 μl) using spin-coating technique at 2000 rpm for 30 s, and then placed on the hot plate at 120 ^{o}C for annealing for 15 min. Additionally, the perovskite coated substrates were covered with petri dishes during the annealing process. Figure 3.9-(a) and Figure 3.9-(b) demonstrates the microscope images of the $Cs_3Bi_2Br_9$ and $Cs_3Bi_2I_9$ thin films, respectively. It was shown that the best coverage of the thin films was obtained after the ITO-glass substrates and perovskite solutions were heated up. The dot-like spots at the microscope images were attributed to some impurities in the perovskite solutions.

The spiro-MeOTAD solution (15 μl) was coated on the perovskite layer using spin-coating at 4000 rpm for 30 s after the perovskite coated ITO-glass substrate was cooled down at room temperature [98]. Therefore, the coating of the HTM of the Bi-based perovskite solar cell was completed.

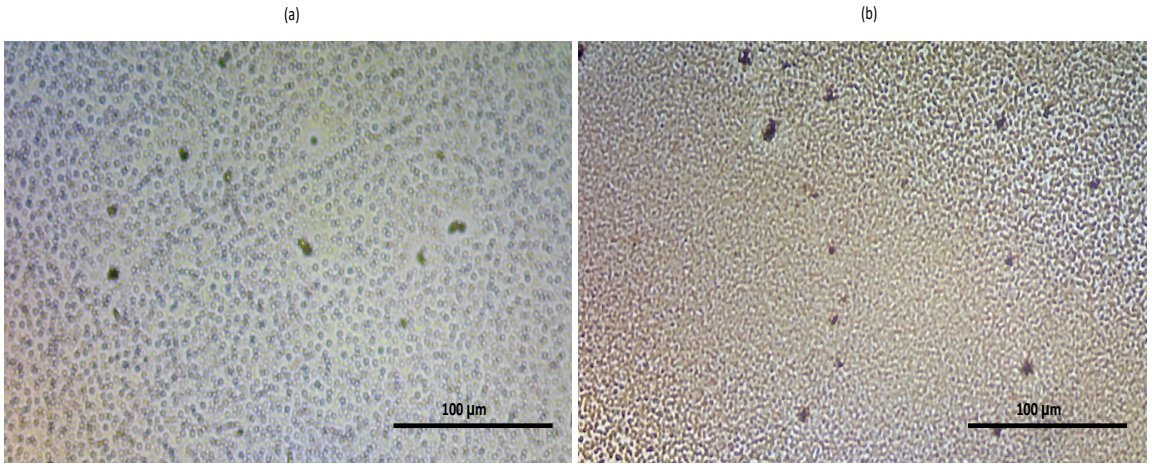

FIGURE 3.9: Microscope images of perovskite layers coated with a) $Cs_3Bi_2Br_9$ solution at 70 ^{o}C, b) $Cs_3Bi_2I_9$ solution at 70 ^{o}C. The ITO-glass substrates were heated at 120 ^{o}C before coating.

A sputter coater (Agar auto) was used to coat the substrates with Au as the counter electrode. The spiro-MeOTAD coated ITO-glass substrate was placed on a deposition mask (multi electrode mask, Ossila), and put in the sputter coater. After sputtering for 60 s, 200 μm Au layer was placed on the spiro-OMeTAD layer. Therefore, the production of the Bi-based perovskite solar cell was completed.

Figure 3.10 shows the schematic diagram and images of the bi-based perovskite solar cells, which were produced using $Cs_3Bi_2I_9$ and $Cs_3Bi_2Br_9$. The substrates, which were coated with $Cs_3Bi_2I_9$, had orange colour, while the substrates coated with $Cs_3Bi_2Br_9$ were yellow.

3.3 Production of $MAPbI_3$/Tint Solar Cells

The lead-based perovskite solar cells were produced using methylammonium lead iodide titanate nanotubes ($MAPbI_3$/Tint), spiro-MeOTAD, and Al sheet. The synthesis of the precursor materials and the production procedure of the solar cells were given in the following sections.

3.3.1 Preparation of the lead-based perovskites

NaOH solution (600 ml), which was prepared using sodium hydroxide (97%, pellets, Fisher Scientific) and deionised (DI) water at the concentration of 10 mol/L, was mixed with titanium (IV) oxide (anatase, 99.7%, Sigma-Aldrich) (130 g) [102]. The mixture was put into an autoclave at 140 ^{o}C for 24 h to obtain titanate nanotubes (Tint). Afterwards, Tint solution was treated with deionised water and H_2SO_4 ($\geq$95%,

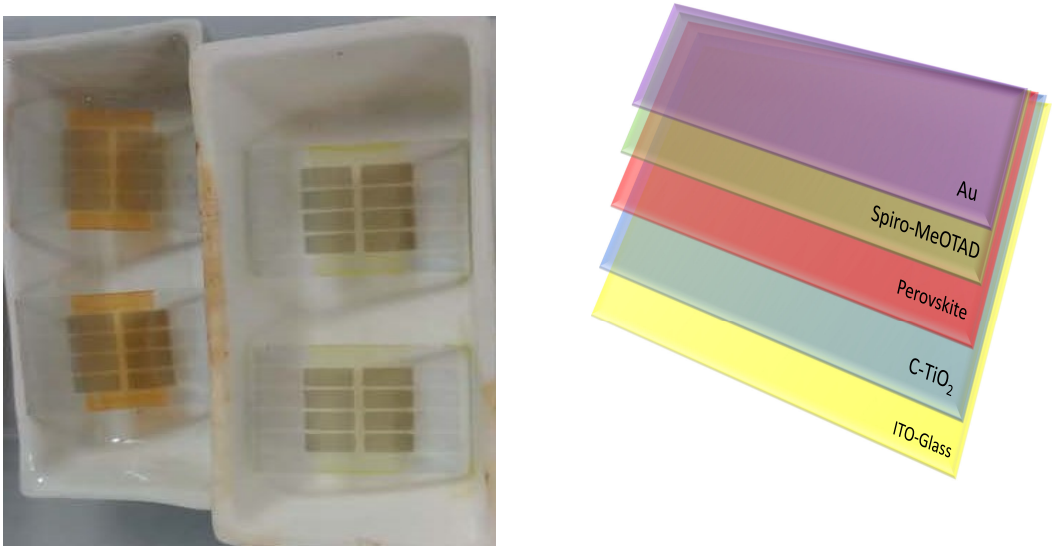

FIGURE 3.10: Left-hand side image shows the bi-based perovskite solar cells produced using $Cs_3Bi_2I_9$ (orange) and $Cs_3Bi_2Br_9$ (yellow), while the right-hand side image shows the schematic diagram of the solar cells.

Fisher Scientific) solution (0.1 mol/L) to decrease pH from 12 to 7. Later, the Tint solution was put into a centrifuge at 3900 rpm, 11030 rotor for 2 min to separate the liquid from the nanotubes. Lastly, the Tint was dried in an oven at 120 ^{o}C overnight, and thereby Tint with the formula of $H_2Ti_3O_7$ having 3-5 nm of internal tube diameter, 7-10 nm of external diameter and several hundred nm of length were obtained [102].

The ion-exchange method was utilised to produce lead titanate nanotubes (Pb/Tint) considering the concentration of 0.25 mol/L for Pb^{2+} ions in DI water [103]. Thus, lead (II) acetate trihydrate ($\geq$99%, Sigma-Aldrich) (1.472 g), Tint (1 g) and DI water (15.527 ml) were mixed on a magnetic stirrer for 5 h taking 1:1 molar ratio between Pb^{2+} and Tint. Afterwards, the mixture was filtered using a PTFE filter with 0.2 μm pore size, and then Pb/Tint white powder was left at room temperature to dry up overnight.

The molar ratio of 2:1 between hydroiodic acid (HI) (57%, Sigma-Aldrich) and Pb/Tint was used to obtain lead iodide titanate nanotubes (PbI_2/Tint). Pb/Tint (1 g), HI (0.570 ml) and DI water (8.643 ml) were mixed on a magnetic stirrer for 1 h considering 0.25 mol/L concentration of Pb/Tint in DI water. After the mixture had been filtered using a PTFE filter with 0.2 μm pore size, PbI_2/Tint yellow powder was put in an oven at 120 ^{o}C overnight.

As for production of the perovskite of $MAPbI_3$/Tint, PbI_2/Tint (0.8 g), methanamine hydroiodide (MAI) (98%, Sigma-Aldrich) (0.283 g) and isopropanol ($\geq$99.5%, Fisher Scientific) (28.320 ml) were mixed for 1 h using 10 mg/mL MAI in isopropanol [87] and 1:1.6 molar ratio for PbI_2/Tint:MAI [104]. The mixture was filtered using 0.2 μm

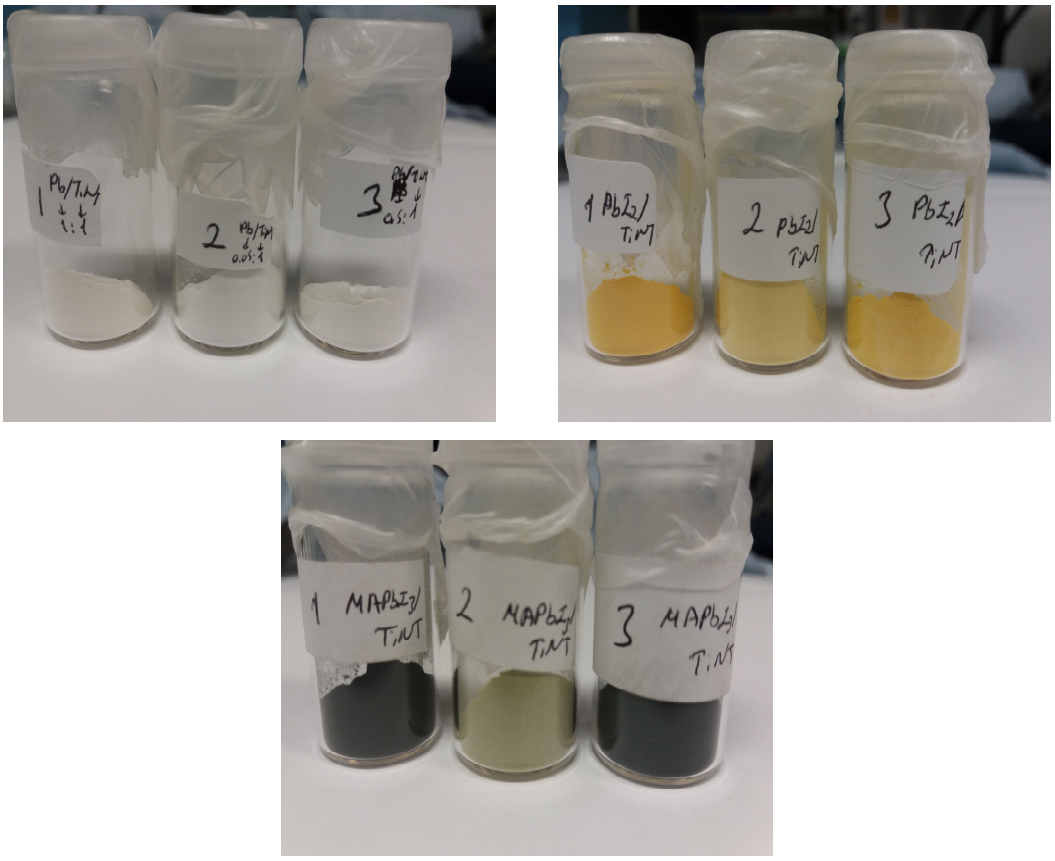

FIGURE 3.11: Images of the precursor powders produced using different molar ratios between Pb^{2+} and Tint, where Pb/Tint powders (left top image), PbI_2/Tint (right top image) and $MAPbI_3$/Tint (bottom image)

PTFE filter, and then $MAPbI_3$/Tint black powder was placed into desiccator to dry up overnight.

Three different ratios between Pb^{2+} and Tint were used while producing the Pb/Tint powder. The procedure above was given for the 1:1 molar ratio between Pb^{2+} and Tint, and the black $MAPbI_3$/Tint perovskite powder was named as (1) $MAPbI_3$/Tint. Besides, the precursor powders of Pb/Tint and PbI_2/Tint were also denoted as (1) Pb/Tint, and (1) PbI_2/Tint.

Additionally, two other molar ratios, 0.05:1 and 0.5:1, between Pb^{2+} and Tint were used to produce perovskites with Tint. The precursors, which were produced using 0.05:1 molar ratio, were labelled (2), while the powders with 0.5:1 ratio were named as (3). Therefore, the materials, which were produced using 0.05:1 molar ratio between Pb^{2+} and Tint, were denoted as (2) Pb/Tint, (2) PbI_2/Tint and (2) $MAPbI_3$/Tint, whereas the precursors with 0.5:1 molar ratio were labelled (3) Pb/Tint, (3) PbI_2/Tint and (3) $MAPbI_3$/Tint.

Figure 3.11 demonstrates the precursors prepared using different molar ratios between Pb^{2+} and Tint. The shade of white colour of Pb/Tint powders with all three

ratios was the same, whereas the shade of yellow colour of (2) PbI_2/Tint powder was paler than (1) PbI_2/Tint and (3) PbI_2/Tint. Moreover, (2) $MAPbI_3$/Tint had pale greenish colour, while (1) $MAPbI_3$/Tint and (3) $MAPbI_3$/Tint were black. Thus, it was decided that (1) $MAPbI_3$/Tint and (3) $MAPbI_3$/Tint were more suitable to use as a light absorber while solar cells were being produced.

3.3.2 Production of the lead-based perovskite solar cells

The pre-patterned ITO-glass substrates (20×15 mm, Ossila) were cleaned using the same procedure in Section 3.2.4. The doctor-blading method was used to coat the light absorber layer and HTM on the ITO-glass substrates [105]. Firstly, $MAPbI_3$/Tint paste composed of $MAPbI_3$/Tint (0.1 g), polyamic acid (5 mg) as a binder and isopropanol (0.5 ml) was deposited on an ITO-glass substrate using the doctor-blading method. Then, the substrate was annealed in an oven at 120 ^{o}C for 0.5 h. After the $MAPbI_3$/Tint coated ITO-glass substrate had cooled down, the HTM of the spiro-MeOTAD solution, whose preparation procedure was given in Section 3.2.3, was coated on the perovskite layer. Lastly, an Al sheet was placed on the solar cell as the counter electrode. Figure 3.12 demonstrates an image of a $MAPbI_3$/Tint solar cell from the ITO-glass side and its schematic diagram.

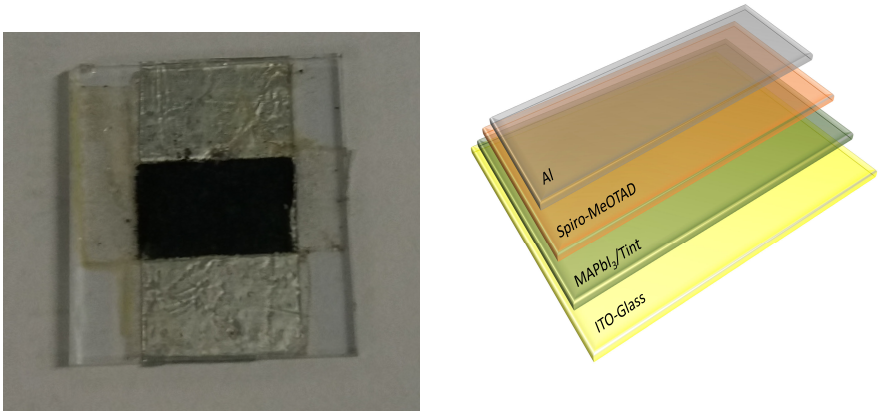

FIGURE 3.12: Images of a $MAPbI_3$/Tint perovskite solar cell from ITO-glass side (left) and schematic diagram (right).

3.4 Characterisation of the Perovskite Solar Cells

UV-vis characteristics of the solar cells were sought using the Scinco spectrophotometer, while the photovoltaic characteristics of the solar cells were determined using the Ossila I-V test system under irradiation of 100 mW.cm^{-2} air mass 1.5 global sunlight. The active area of the solar cells was 0.035 cm^2 using a

measurement aperture mask from Ossila. Additionally, the FTIR measurements of the precursor powders with Tints were obtained employing the ThermoFisher Scientific Nicolet IS5 FTIR spectrometer. All FTIR spectra were recorded in the 4000-500 cm^{-1} wavenumber range, while UV-vis measurements were performed using the wavelength range from 250 to 900 nm.

To measure UV-vis characteristics of $Cs_3Bi_2I_9$, the solution (20 mmol/L) was diluted so that 10 mmol/L concentrated solution was obtained. Additionally, the solution of $Cs_3Bi_2Br_9$ was diluted in the same concentration to obtain its spectral response.

To obtain the UV-vis spectrum of thin films of $Cs_3Bi_2Br_xI_{9-x}$, firstly, the solutions with 20 mmol/L were coated on quartz by spin coating at 2000 rpm for 30 s after heating up to 70 ^oC. Later, the coated quartz was placed on a hot plate at 120 ^oC for 15 mins for annealing.

As for the $Cs_3Bi_2I_9$ and $Cs_3Bi_2Br_9$ thin films with different layers, the perovskite thin films were produced applying the following procedure. Once a perovskite layer was formed after annealing and cooling down the ITO-glass substrate, another layer was applied using spin-coating. The aim was to find a thin layer of perovskite with better absorption.

Chapter 4

First Principle Calculations on Structural, Electronic and Optical Properties of $Cs_3Bi_2X_9$ (X=Br,I)

Perovskite solar cells have attracted great interest due to the considerable increase in their PCE. However, the toxicity of lead raises concerns about its usage as B part metal in the perovskite chemical structure formula of ABX_3. A less toxic trivalent cation of Bi^{3+} is a suitable alternative metal to overcome the toxicity issue. The heterovalent substitution of lead changes the perovskite chemical structure from ABX_3 to $A_3B_2X_9$ to retain charge neutrality [106]. Thus, various bi-based perovskites with the chemical structure of $A_3Bi_2X_9$ were introduced by using different A-side cations and X-side anions, such as $CH_3NH_3^+$, Cs^+ and Br^-, Cl^-, I^-, respectively [107].

DFT is a useful first-principles simulation method to calculate the structural, electronic, and optical properties of solid materials. There are several examples in which first-principle DFT calculations have been used to investigate the properties of perovskites. The electronic band gaps and energy bands of $MAPbI_3$ were investigated by using DFT via Vienna Ab-initio Simulation Package (VASP) with Generalised Gradient Approximations (GGAs) of Perdew, Burke and Ernzerhof (PBE) and PBEsol [108]. Additionally, the first principles DFT calculations were performed to obtain optimised crystal structure, electronic band structure and density of states of $MAPbI_3$ by using different functional theories, which were LDA, PBE/GGA, PW91/GGA and WC/GGA in CASTEP [109]. Refractive index and extinction coefficients of $MAPbI_3$ doped with Br or Cl and $MAPbBr_3$ doped with Cl or I was obtained using the exchange-correlation function of PBE with CASTEP [110]. As for lead-free perovskites, $Cs_3Sb_2I_9$ was examined in terms of electronic band structure, the partial density of states (PDOS) and absorption coefficient with the help of PAW method with the Heyd-Scuseria-Ernzerhof (HSE) functional in VASP [111]. Electronic

band structure, optical absorption spectra, DOS and PDOS of bi-based perovskite of $Cs_3Bi_2I_9$ were obtained using the PAW method with GGA-PBE functional and HSE with and without spin-orbit coupling (SOC) in VASP [112].

In this work, $Cs_3Bi_2I_9$, $Cs_3Bi_2Br_9$, and $Cs_3Bi_2Br_3I_6$ have been examined in terms of their optimised crystal structure, electronic band structure, the density of states and absorption coefficients. First-principles DFT calculations were employed to investigate the structural, electronic, and optical properties of the perovskites with the help of the CASTEP computer program code. CASTEP was not used to seek the characteristics of the inorganic Bi-based perovskites before this study.

4.1 Crystal Structure

The crystal structure of $Cs_3Bi_2I_9$ is built once bioctahedral $[Bi_2I_9]^{3-}$ clusters, which are formed by face-sharing BiI_6, are surrounded by Cs^+ cations [113]. $Cs_3Bi_2I_9$ crystallises in the hexagonal space group of $P6_3/mmc$ with the lattice parameters of a=b=8.294 $\mathring{A}$, c=21.312 $\mathring{A}$, α=β=90^o, and γ=120^o. Figure 4.1 shows the crystal structure of $Cs_3Bi_2I_9$ obtained from two different software, Jmol (top) and VESTA (bottom). The unit cell from Jmol involves only double $Cs_3Bi_2I_9$ atoms' locations, whereas the unit cell from VESTA includes all atom positions after being symmetrically propagated. As shown in the figure, $Cs_3Bi_2I_9$ consists of a stacking of hexagonal CsI_3 layers in a close-packed structure in which Cs has twelve I nearest-neighbours while Bi atoms are surrounded by six I atoms to fill octahedral spaces [94].

$Cs_3Bi_2Br_9$ owns trigonal crystal structure in $P\bar{3}m1$ the hexagonal space group with the lattice parameters of a=b=7.901 $\mathring{A}$, c=9.823 $\mathring{A}$, α=β=90^o, and γ=120^o. $Cs_3Bi_2Br_9$ crystal structure consists of Cs and Br atoms in cubic closest packing and corrugated layers, which are created by $BiBr_6$ octahedra sharing three vertices [95]. Figure 4.2 demonstrates the crystal structures of $Cs_3Bi_2Br_9$, which were obtained by Jmol (top) and VESTA (bottom). The crystal structure from Jmol indicates the atomic positions of a single $Cs_3Bi_2Br_9$ in a unit cell and lattice parameters. On the other hand, the crystal structure from VESTA gives all atomic positions occupied by $Cs_3Bi_2Br_9$ atoms in a unit cell.

The crystal structure of $Cs_3Bi_2Br_3I_6$ belong to the trigonal space group $P\bar{3}m1$ with the lattice parameters of a=b=8.143 $\mathring{A}$, c=10.033 $\mathring{A}$, α=β=90^o, and γ=120^o. $Cs_3Bi_2Br_3I_6$ crystal structure was illustrated using Jmol and VESTA, whose results were given in Figure 4.3. The crystal structure obtained from Jmol showed the atomic positions of a single $Cs_3Bi_2Br_3I_6$ perovskite in a unit cell, whereas the crystal structure from VESTA demonstrated a unit cell which was fully occupied from $Cs_3Bi_2Br_3I_6$ atoms.

4.2 Electronic Structure

The electronic band structure and density of states of $Cs_3Bi_2I_9$ are given in Figure 4.4-(a) and Figure 4.4-(b), respectively, in which Fermi energy levels were set to zero. The calculated band structure results show that the valence band maximum (VBM) is located at K, while the conduction band minimum (CBM) is at Γ, which indicates $Cs_3Bi_2I_9$ has an indirect bandgap. The indirect band gap was found as 1.99 eV, which is in good agreement with the previously reported experimental value of 1.9 eV [114]. On the other hand, the narrowest direct band gap of $Cs_3Bi_2I_9$, which is placed at Γ, was calculated as 2.13 eV. Additionally, the density of states is given in Figure 4.4-(b).

The perovskite of $Cs_3Bi_2Br_9$ was examined in terms of electronic band structure and density of states in Figure 4.5-(a) and Figure 4.5-(b), respectively, in which the dashed lines stand for Fermi energy level, which was set to zero. Figure 4.5-(a) demonstrates that both VBM and CBM are located at Γ and thereby $Cs_3Bi_2Br_9$ owns a direct band gap calculated as 2.42 eV. On the other hand, Figure 4.5-(b) illustrates the density of states of $Cs_3Bi_2Br_9$.

Figure 4.6-(a) demonstrates the energy band diagram of $Cs_3Bi_2Br_3I_6$, which was obtained calculating the energy of electronic states as a function of wave vectors, k, in reciprocal space. Fermi level was denoted by dashed lines at 0 eV. The occupied energy levels below the Fermi level were clearly separated from the unoccupied energy levels, which showed that the perovskite was a semiconductor. Additionally, VBM and CBM were located at different high symmetry k-points, which means $Cs_3Bi_2Br_3I_6$ owns an indirect band gap. The magnitude of the energy band gap was calculated as 1.83 eV. Figure 4.6-(b) illustrates the distribution of energy bands via density of states.

Figure 4.7-(a), Figure 4.8-(a), and Figure 4.9-(a) shows the electronic density of states for $Cs_3Bi_2I_9$, $Cs_3Bi_2Br_9$, and $Cs_3Bi_2Br_9$, respectively. Results in Figure 4.7 and Figure 4.8 were obtained by OptaDOS. The electronic density of states was compatible with the results, which were obtained using CASTEP in Figure 4.4-b, Figure 4.5-b, and Figure 4.6-b. Besides, Figure 4.7-(b), Figure 4.8-(b), and Figure 4.9-(b) demonstrate the joint electronic density of states of related perovskites.

4.3 Optical Properties

The absorption coefficients of $Cs_3Bi_2I_9$ and $Cs_3Bi_2Br_9$ are demonstrated in Figure 4.10-(a) and Figure 4.10-(b), respectively. It was observed that absorption coefficients showed blue-shifted movement when the halogen in $Cs_3Bi_2X_9$ changed from I to Br, which was compatible with the fact that the perovskites with Br had a higher energy band gap compared to the perovskites with I [110]. The absorption

coefficient edge of $Cs_3Bi_2I_9$ was recorded at 2.04 eV, whereas that of $Cs_3Bi_2Br_9$ was at 2.26 eV.

The absorption coefficient of the inorganic dual halide perovskite of $Cs_3Bi_2Br_3I_6$ is demonstrated in Figure 4.11. The band gap energy has an important role in the light-harvesting capability of an optoelectronic device [115]. The absorption coefficient onset of $Cs_3Bi_2Br_3I_6$ was observed at 1.74 eV, which was slightly different from the calculated energy band gap of $Cs_3Bi_2Br_3I_6$, which was 1.83 eV. Additionally, the energy band gap and absorption coefficient onset energy were compatible with each other for the perovskite of $Cs_3Bi_2I_9$ with the values of 1.99 eV and 2.04 eV. However, a significant difference between the absorption coefficient onset and band gap energies was observed in the results of $Cs_3Bi_2Br_9$. The absorption coefficient edge of $Cs_3Bi_2Br_9$ was recorded at 2.26 eV, whereas the energy band gap was calculated as 2.42 eV.

4.4 Discussion

This study aimed to theoretically investigate three Bi-based perovskites, $Cs_3Bi_2I_9$, $Cs_3Bi_2Br_9$ and $Cs_3Bi_2Br_3I_6$ in terms of structural, electronic and optical features using the first principle DFT calculations with CASTEP. The purpose of investigation on Bi-based perovskites was that they provide better stability, high PV performance, and more extensive usage in PV applications in addition to lower toxicity compared to Pb-based counterparts [116]. Additionally, DFT calculations along with CASTEP modelling software offer a useful tool to investigate structural, chemical, optical, spectroscopic, elastic, vibrational and thermodynamic properties in solid-state physics [117]. Therefore, it was aimed that the results contribute to the literature in terms of the theoretical research on determining the properties of the perovskites.

The crystallographic results showed that $Cs_3Bi_2I_9$ was in the hexagonal space group of $P6_3/mmc$ after the geometry optimisation via CASTEP, which was compatible with a study on the crystal structure of $Cs_3Bi_2I_9$ using DFT calculations via VASP [118]. Furthermore, electronic band structure calculations showed that $Cs_3Bi_2I_9$ had a direct band gap of 2.13 eV, which was in good agreement with the value of 2.12 eV in a study on $Cs_3Bi_2I_9$ via VASP [119]. Moreover, the calculations demonstrated that $Cs_3Bi_2I_9$ owned the indirect band gap energy of 1.99 eV, which was coherent with 2.02 eV from a DFT study on $Cs_3Bi_2I_9$ using a Quantum Espresso package [120].

As for the structural properties of $Cs_3Bi_2Br_9$, the crystal structure of it possessed trigonal distortion and $P\bar{3}m1$ symmetry after the geometry optimisation via CASTEP, which was compatible with the findings in a study on $Cs_3Bi_2Br_9$ perovskites using DFT [121]. However, the calculated direct band gap energy of $Cs_3Bi_2Br_9$ was inconsistent with the values in the literature. In this study, the band gap energy of 2.42 eV was underestimated by DFT calculations via CASTEP, whereas the band gap of

$Cs_3Bi_2Br_9$ was calculated as 2.66 eV in a study using DFT via VASP [122]. The band gap energy difference between the calculated value via CASTEP and the value from VASP in literature was attributed to cell parameters of the unit cell of $Cs_3Bi_2Br_9$. A c-doubled unit cell was suggested to obtain more compatible results with the ones in the literature. The c-doubled P$\bar{3}$m1 trigonal unit cell could be utilised with the cell parameters of a=b=7.8804 $\mathring{A}$ and c = 19.5572 $\mathring{A}$ instead of a=b=7.901 $\mathring{A}$ and c=9.823 $\mathring{A}$ [123].

4.5 Conclusion

The inorganic Bi-based perovskites of $Cs_3Bi_2I_9$, $Cs_3Bi_2Br_9$ and $Cs_3Bi_2Br_3I_6$ were theoretically investigated to obtain crystal structure, electronic and optical properties using DFT via CASTEP in this study. The results showed that $Cs_3Bi_2I_9$ belonged to $P6_3/mmc$ hexagonal space group, whereas $Cs_3Bi_2Br_9$ had P$\bar{3}$m1 hexagonal space group. Additionally, the calculated electronic band structures of the perovskites demonstrated that $Cs_3Bi_2I_9$ had an indirect band gap, while $Cs_3Bi_2Br_9$ owned a direct band gap. Moreover, absorption coefficient peaks performed blue-shifted tendency the halide X in $Cs_3Bi_2X_9$ structure changed from I to Br. Before this study, no theoretical investigation for structural, electronic and optical properties of the inorganic halide Bi-based perovskites of $Cs_3Bi_2I_9$, $Cs_3Bi_2Br_9$ and $Cs_3Bi_2Br_3I_6$ was conducted using the CASTEP code.

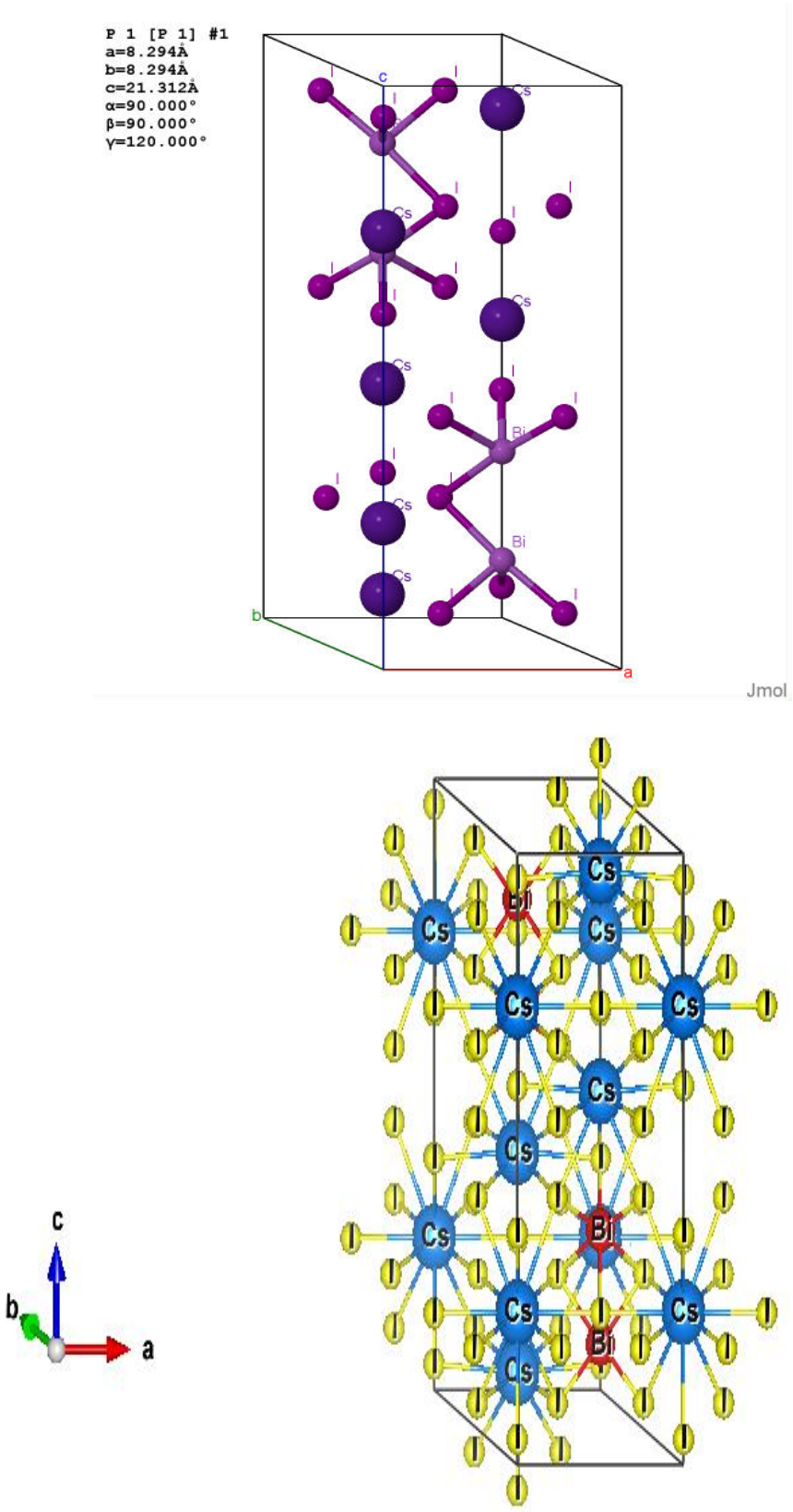

FIGURE 4.1: Crystal structure of $Cs_3Bi_2I_9$ simulated by Jmol (top) and VESTA (bottom). In the unit cell from Jmol, Cs, Bi and I are shown in violet, purple and magenta, respectively. In the unit cell from VESTA, Cs, Bi and I are represented in blue, red, and yellow, respectively. Cell parameters of the unit cell are given at the top left corner of the figure.

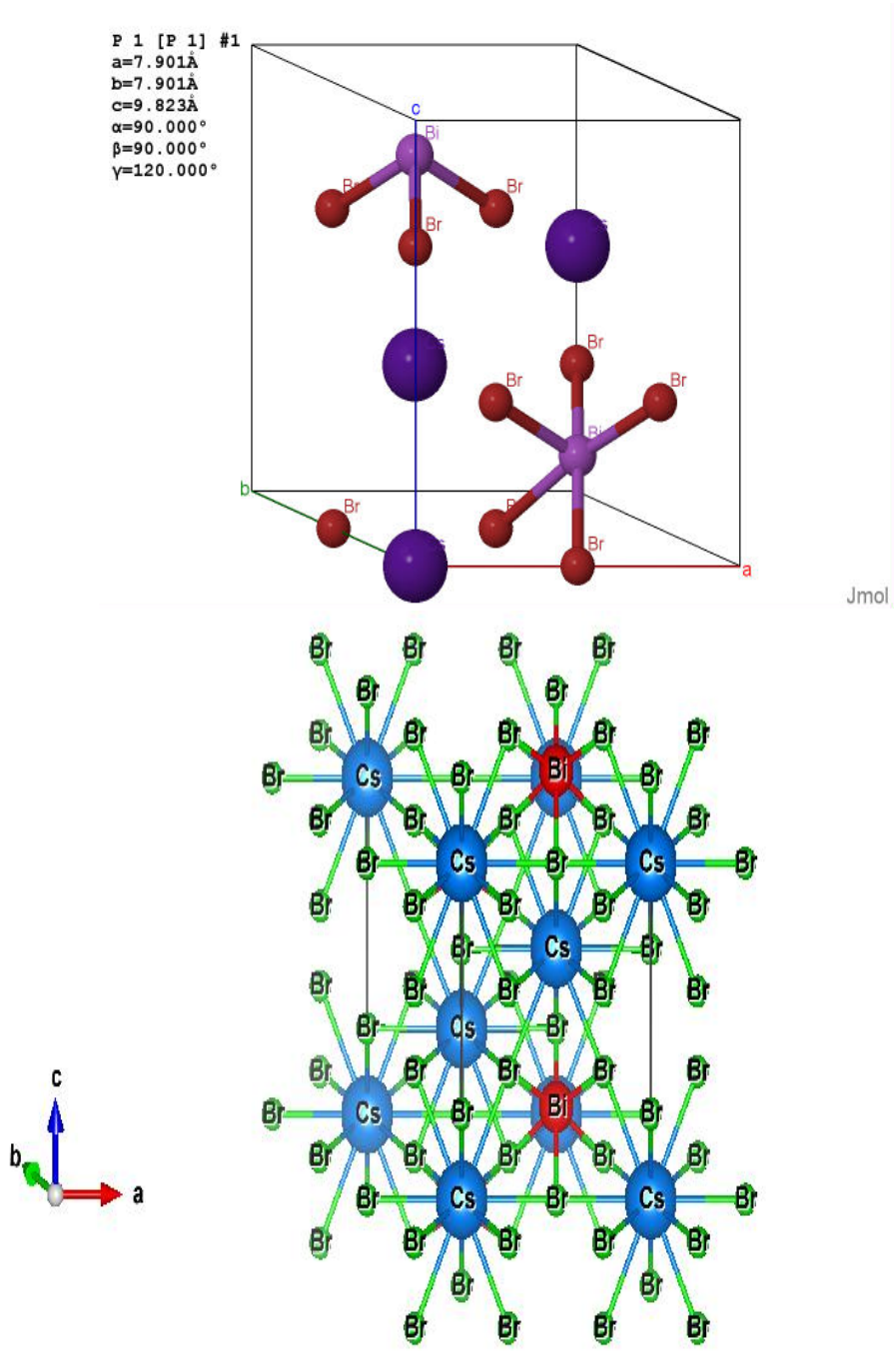

FIGURE 4.2: Crystal structure of $Cs_3Bi_2Br_9$ obtained by Jmol (top) and VESTA (bottom). Cs, Bi and Br atoms are presented in violet, purple and red, respectively, in the unit cell from Jmol. Additionally, in the crystal structure obtained from VESTA, Cs, Bi and Br atoms are presented in blue, red, and green, respectively. Cell parameters are given at the left corner of the figure.

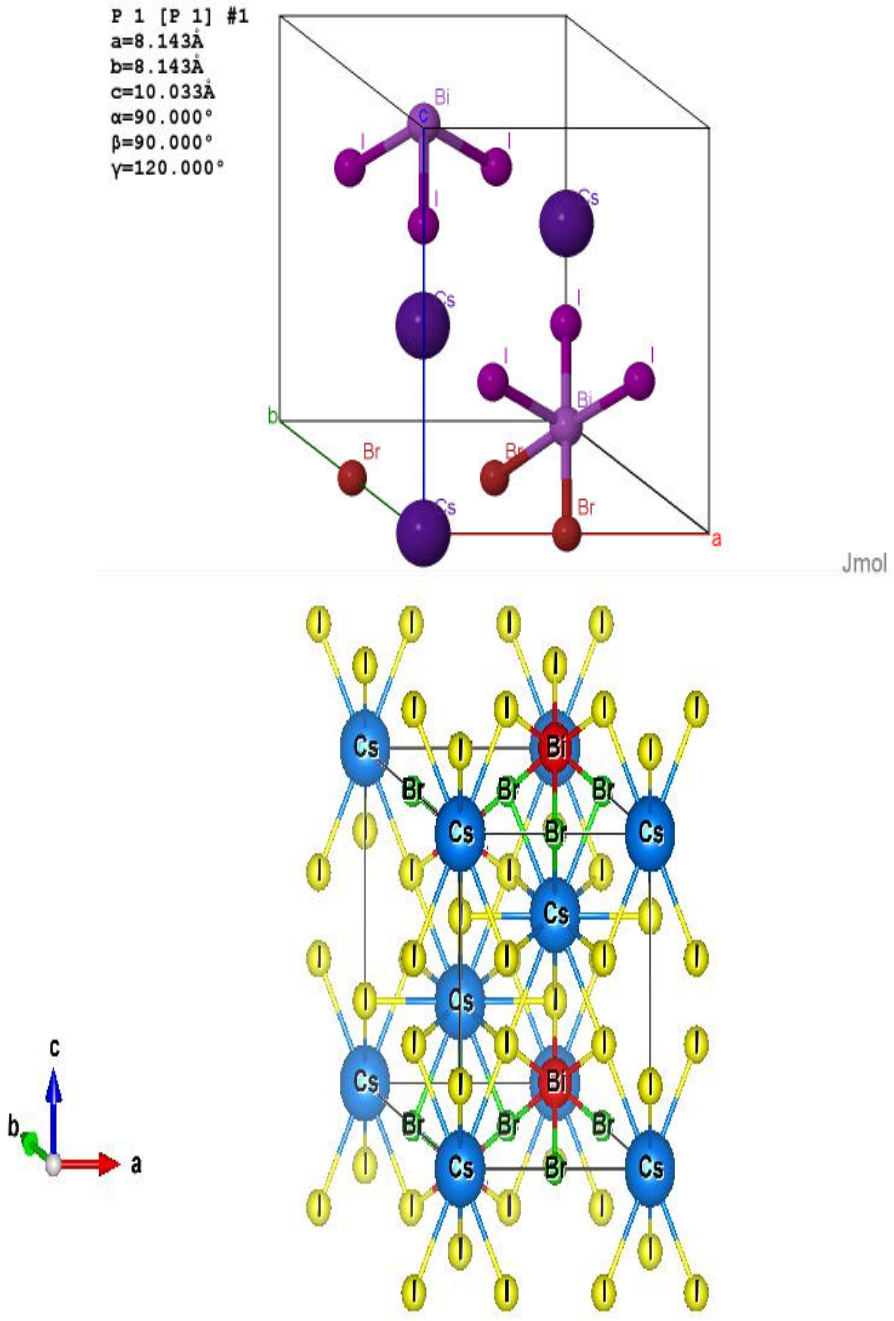

FIGURE 4.3: Crystal structure of $Cs_3Bi_2Br_3I_6$ obtained by Jmol (top) and VESTA (bottom). Cs, Bi, Br and I atoms are presented in violet, purple, red and magenta, respectively, in the unit cell from Jmol, whereas Cs, Bi, Br and I atoms are presented in blue, red, green and yellow, respectively, in the unit cell from VESTA. Cell parameters are given at the left corner of the figure.

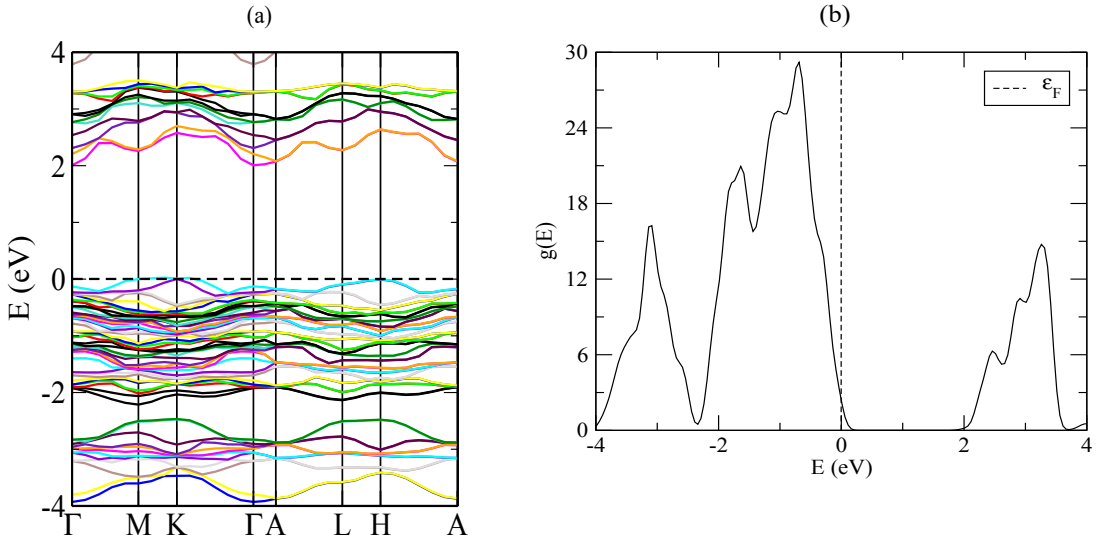

FIGURE 4.4: Calculated electronic band structure (a) and density of states (b) of $Cs_3Bi_2I_9$. Dashed lines represent Fermi energy level, which was set to zero.

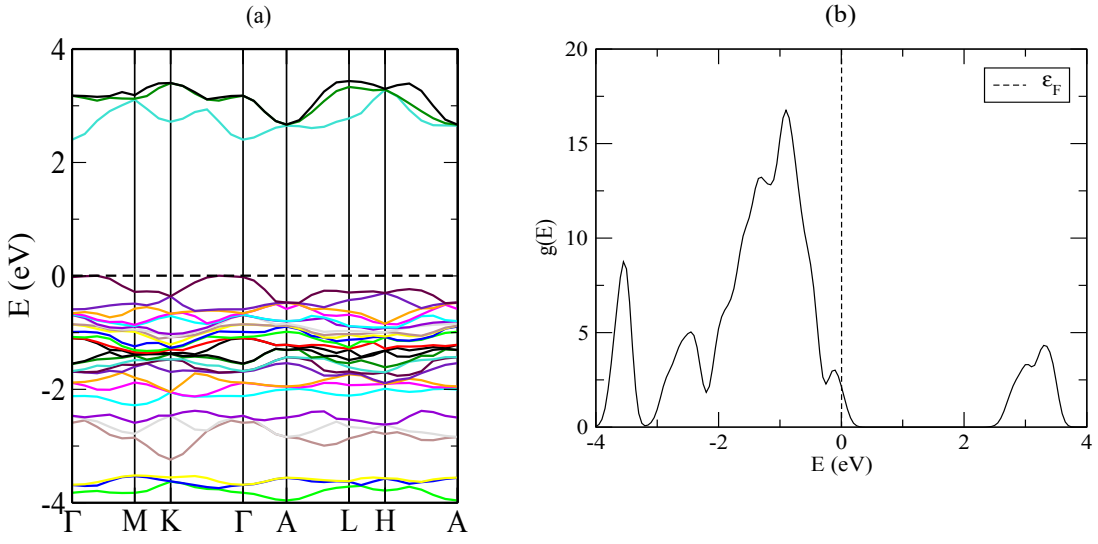

FIGURE 4.5: Calculated electronic band structure (a) and density of states (b) of $Cs_3Bi_2Br_9$. Dashed lines represent Fermi energy level, which was set to zero.

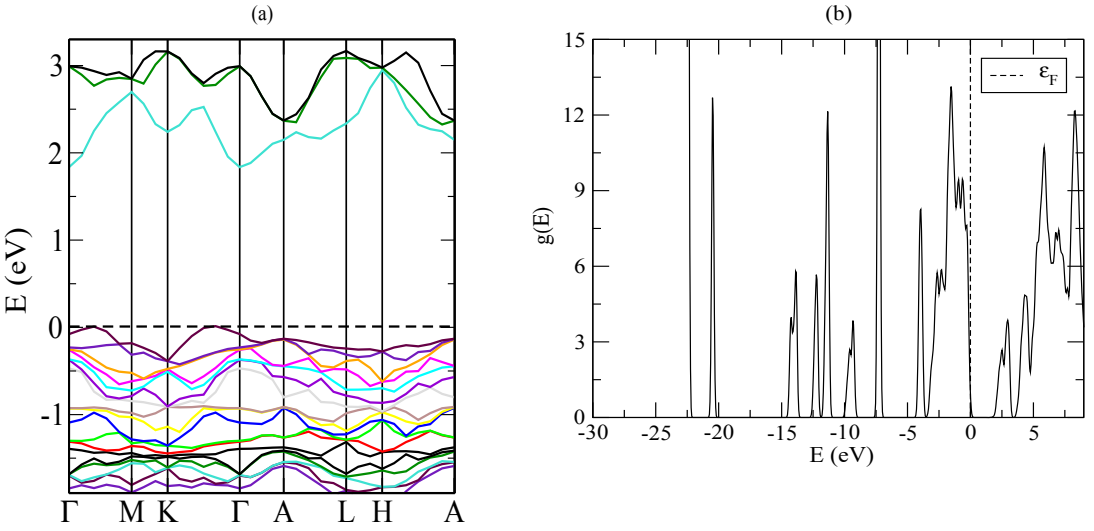

FIGURE 4.6: Calculated electronic band structure (a) and density of states (b) of $Cs_3Bi_2Br_3I_6$. Dashed lines represent Fermi energy level, which were set to zero.

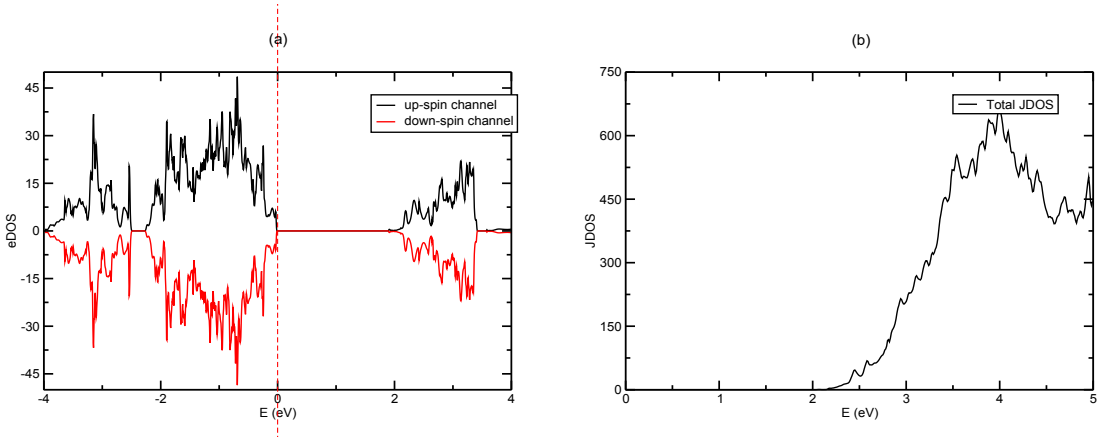

FIGURE 4.7: (a) Electronic density of states and (b) joint density of states of $Cs_3Bi_2I_9$, which were calculated using OptaDOS.

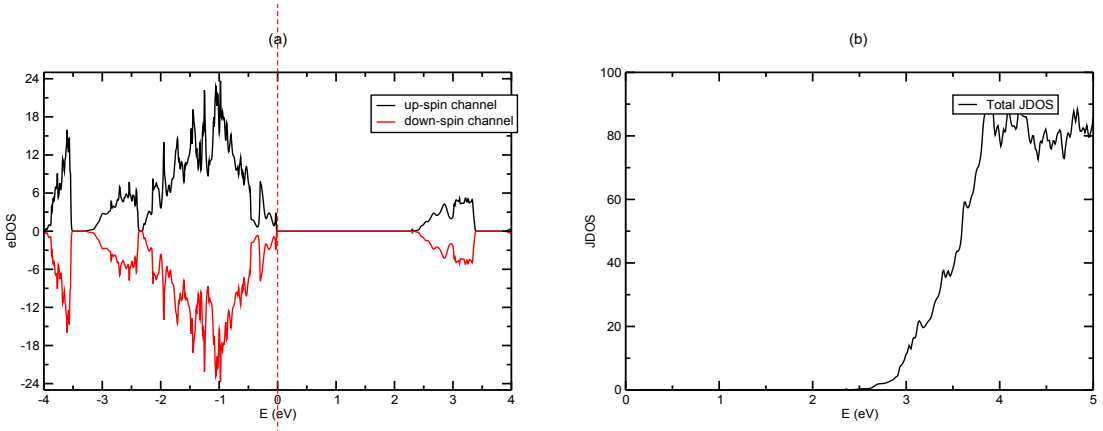

FIGURE 4.8: (a) Electronic density of states and (b) joint density of states of $Cs_3Bi_2Br_9$, which were calculated using OptaDOS.

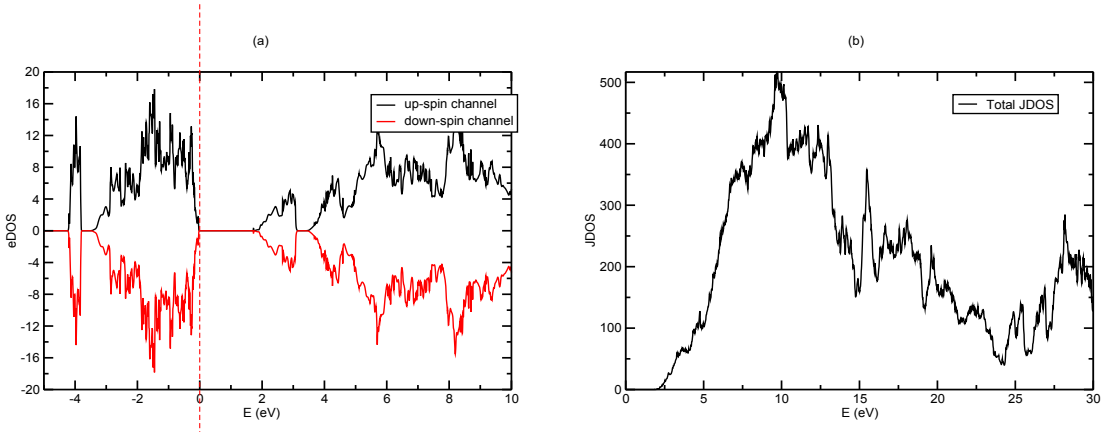

FIGURE 4.9: (a) Electronic density of states and (b) joint density of states of $Cs_3Bi_2Br_3I_6$, which were calculated using OptaDOS.

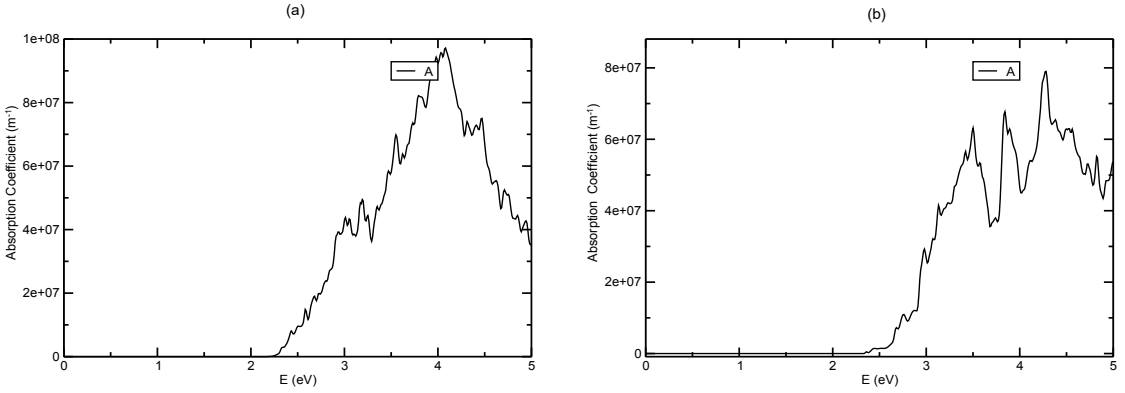

FIGURE 4.10: Calculated absorption coefficients of (a) $Cs_3Bi_2I_9$ and (b) $Cs_3Bi_2Br_9$, which are obtained by OptaDOS.

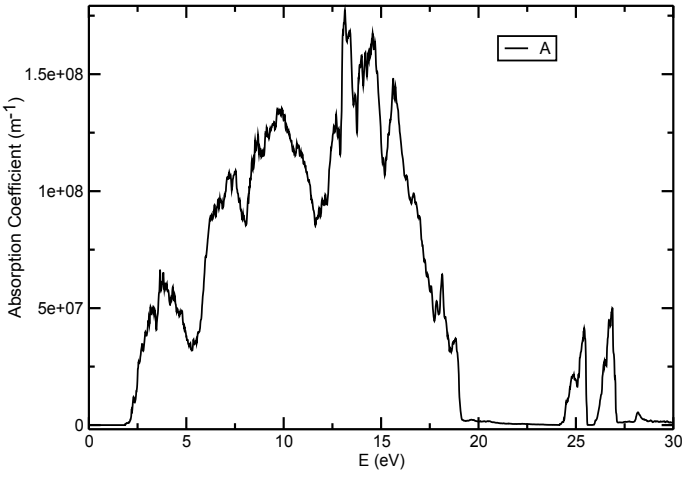

FIGURE 4.11: Calculated absorption coefficients of $Cs_3Bi_2Br_3I_6$ obtained by OptaDOS.

Chapter 5

Photovoltaic Characteristics of $Cs_3Bi_2Br_xI_{9-x}$ Perovskite Solar Cells

Perovskite solar cells (PSCs) are produced using various cations, metals, and anions in the basic chemical structure of ABX_3. It was observed that the usage of Br ions or I ions did not significantly affect the PCE of PSCs because $MAPbI_3$ solar cells and $MAPbBr_3$ solar cells performed similar PCE values, which were 3.81% and 3.13%, respectively [10]. However, it was observed that the substitution of Br^- for I^- in $MAPbI_3$ improved the stability of the cells under ambient conditions with controlled humidity [124]. Additionally, it was reported that the incorporation of $MAPbBr_3$ into $FAPbI_3$ provided the stabilisation of the perovskite phase with a uniform and dense morphology in addition to improved PCE [77].

On the other hand, the usage of bismuth as the metal part in the ABX_3 structure provided an alternative solution to overcome the toxicity issue of lead-based perovskites. Additionally, it was observed that $MA_3Bi_2I_9$ PSCs were stable in ambient air and humidity conditions [24]. Besides, the fully inorganic $Cs_3Bi_2I_9$ PSC performed higher PCE than the organic-inorganic bi-based counterparts [107].

In this study, binary halide organic bi-based perovskites with the structure of $Cs_3Bi_2Br_xI_{9-x}$ were used to produce PSCs where the x value varies from 0 to 9. Therefore, it was aimed to fabricate a solar cell with low toxicity, high stability and improved PCE.

5.1 Spectral Response

Absorption graphs of $Cs_3Bi_2I_9$ and $Cs_3Bi_2Br_9$, which were obtained by diffuse reflectance spectroscopy (DRS) and transmittance spectroscopy, are demonstrated in Figure 5.1. Figure 5.1-a illustrates the absorption spectra of the precursor solutions with 10 mmol/L concentration, whereas Figure 5.1-b shows the absorbance curves from thin films of the perovskites. There is a blue-shifted change of the absorption curves when the halogen part X of the $Cs_3Bi_2X_9$ perovskite is changed from I to Br, which is compatible with our computational absorption coefficient results. Additionally, absorption peaks go to the blue-shifted region further when the perovskites are in DMF in Figure 5.1-a.

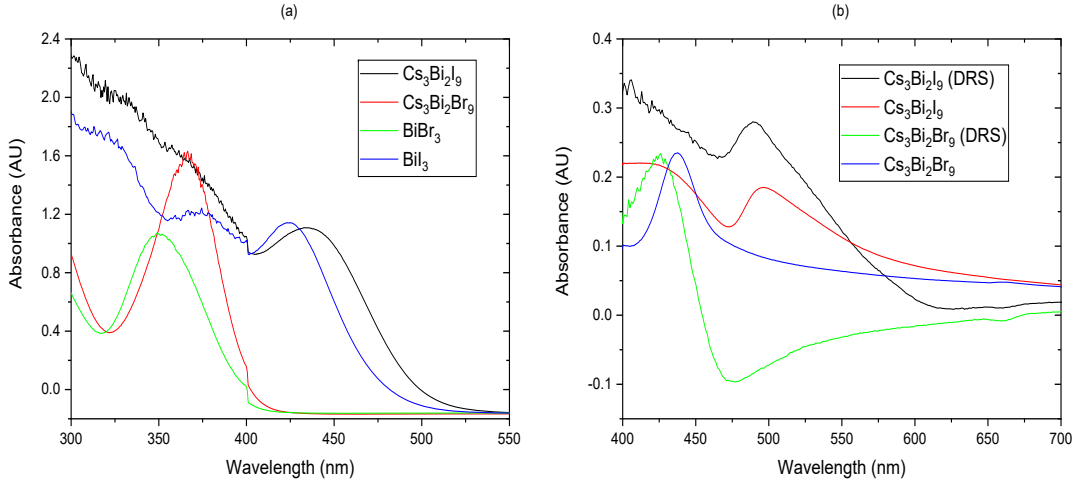

FIGURE 5.1: (a) Absorption spectra of the precursor solutions of $Cs_3Bi_2I_9$, $Cs_3Bi_2Br_9$, $BiBr_3$ and BiI_3 obtained from transmittance spectroscopy. (b) Absorption spectra of perovskite thin films from DRS and transmittance spectroscopy.

The energy band gaps for $Cs_3Bi_2I_9$ and $Cs_3Bi_2Br_9$ were experimentally estimated from the Kubelka-Munk function using the reflectance data of DRS results [125]. Figure 5.2 demonstrates the Tauc plots of the perovskites to determine their band gaps. Figure 5.2-a illustrates that the indirect band gap perovskite of $Cs_3Bi_2I_9$ has a 2.00 eV energy band gap, which is in great agreement with our calculated energy band gap of 1.99 eV by CASTEP. On the other hand, in Figure 5.2-b, the band gap of $Cs_3Bi_2Br_9$ was obtained as 2.68 eV, which is compatible with the previously reported value of 2.67 eV [126].

Figure 5.3 shows the absorbance graphs of $Cs_3Bi_2I_9$ and $Cs_3Bi_2Br_9$ with different layers. It was observed that there was not a clear difference in the curves of $Cs_3Bi_2I_9$ thin films with different layers in Figure 5.3-(a). This means that the solvent, DMF, completely solves the crystallised perovskite thin film on the ITO-glass substrate while applying another layer. As for the absorbance curves of $Cs_3Bi_2Br_9$ in Figure 5.3-(b), an increase in the number of layers induced an increase in absorbance

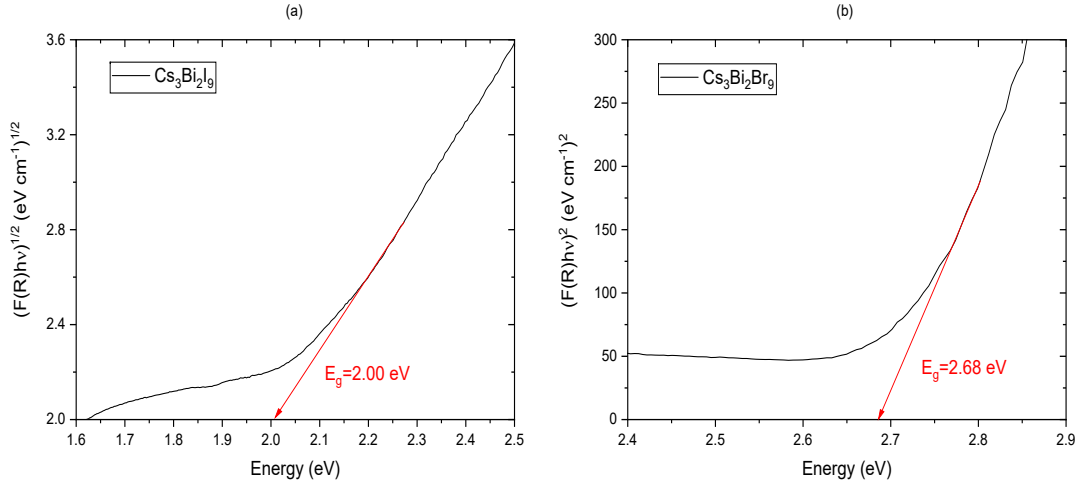

FIGURE 5.2: Tauc plots of (a) $Cs_3Bi_2I_9$ and (b) $Cs_3Bi_2Br_9$ using Kubelka-Munk function.

peaks. Therefore, it would be better to apply the perovskite of $Cs_3Bi_2Br_9$ several times to capture more light.

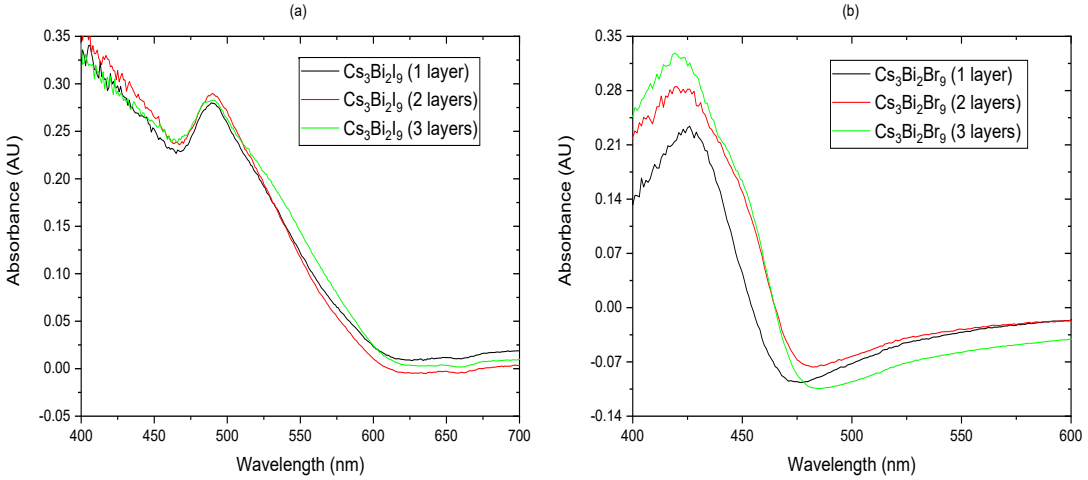

FIGURE 5.3: Absorbance spectra of (a) $Cs_3Bi_2I_9$ and (b) $Cs_3Bi_2Br_9$ with different layers

Figure 5.4 illustrates the absorbance spectra of the $Cs_3Bi_2Br_xI_{9-x}$ perovskite thin films on quartz substrates by using transmittance spectroscopy. The absorption spectra edge moved to lower wavelengths while the x value in $Cs_3Bi_2Br_xI_{9-x}$ chemical structure increased from 0 to 9. The absorption edge of $Cs_3Bi_2I_9$ was around 610 nm, whereas the absorption edge of $Cs_3Bi_2Br_9$ was around 480 nm. As for the peak intensities, there were not any continuous patterns observed while the molar ratios between I and Br changed. The highest peak intensities were obtained from the perovskites with a single halogen.

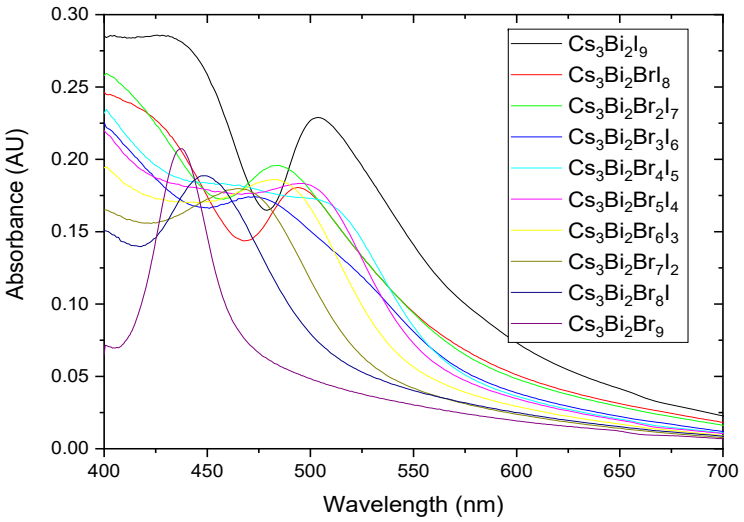

FIGURE 5.4: Absorbance spectra of $Cs_3Bi_2Br_xI_{9-x}$ where x varies from 0 to 9.

Figure 5.5 demonstrates the Tauc plots of $Cs_3Bi_2Br_xI_{9-x}$ perovskite thin films on quartz substrates. The estimated energy band gaps of the perovskites were obtained from the reflectance data of transmittance spectroscopy using the Kubelka-Munk function in Table 5.1. The energy band gaps systematically increased with varying x from 0 to 9, which was compatible with the blue-shifted pattern in the absorption edges with increasing x in $Cs_3Bi_2Br_xI_{9-x}$.

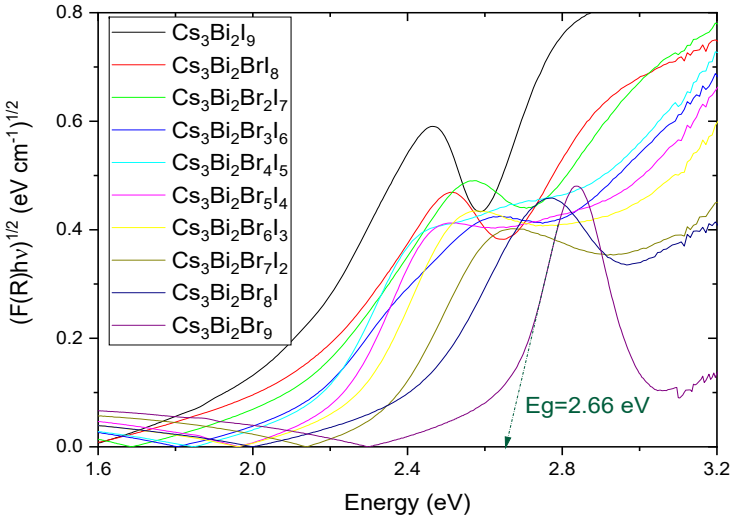

FIGURE 5.5: Tauc plots of $Cs_3Bi_2Br_xI_{9-x}$ where x is varying from 0 to 9.

Perovskites	Band gap (eV)
$Cs_3Bi_2I_9$	1.99
$Cs_3Bi_2BrI_8$	2.03
$Cs_3Bi_2Br_2I_7$	2.06
$Cs_3Bi_2Br_3I_6$	2.08
$Cs_3Bi_2Br_4I_5$	2.14
$Cs_3Bi_2Br_5I_4$	2.19
$Cs_3Bi_2Br_6I_3$	2.24
$Cs_3Bi_2Br_7I_2$	2.32
$Cs_3Bi_2Br_8I$	2.39
$Cs_3Bi_2Br_9$	2.66

TABLE 5.1: Energy band gaps of $Cs_3Bi_2Br_xI_{9-x}$ perovskites from Tauc plots

5.2 Current Density-Voltage Characteristics

The bi-based perovskite solar cells were fabricated using the architecture of ITO-glass/c-TiO_2/perovskite/spiro-MeOTAD/Au, whose preparation procedure was given in Section 3.2.4. The c-TiO_2 solution was produced using two different recipes, whose preparation method was explained in Section 3.2.2. Figure 5.6 demonstrates the J-V curves from $Cs_3Bi_2I_9$ perovskite solar cells with two different c-TiO_2 recipes. The photovoltaic characteristics of the solar cell with recipe 1 c-TiO_2 layer were recorded as PCE of 0.05%, FF of 0.16, V_{oc} of 0.69 V and J_{sc} of 0.44 mA.cm^{-2} in Figure 5.6-(a). On the other hand, the solar cell with recipe 2 c-TiO_2 layer provided PCE of 0.05% with FF of 0.23, V_{oc} of 0.61 V and J_{sc} of 0.39 mA.cm^{-2} in Figure 5.6-(b). Although the PCEs of the $Cs_3Bi_2I_9$ solar cells with two different c-TiO_2 recipes were quite like each other, recipe 2 was chosen to produce the bi-based solar cells because the microscope images of recipe 1 c-TiO_2 layer showed non-uniform film coverage in Section 3.2.2.

Figure 5.7 illustrates J-V curves of $Cs_3Bi_2Br_xI_{9-x}$ perovskite solar cells under illumination. The solar cells were produced using the cell architecture of ITO-glass/ c-TiO_2/ perovskite/spiro-OMeTAD/Au. The c-TiO_2 solution was produced using recipe 2. The photovoltaic characteristics of the solar cells were given in Table 5.2. It was observed that the V_{oc} of the solar cells increased while the x value changed from 0 to 8, which was attributed to the increase in energy band gaps with increasing x. The increase in V_{oc} with Br addition originates from the fact that the conduction band of Br is higher than that of I [10].

On the other hand, the J_{sc} of the solar cells decreased while the x value increased. The decrease in J_{sc} with increasing the x value stems from the fact that the absorption edges are blue shifted with increasing x [124]. The J-V curves in Figure 5.7 showed

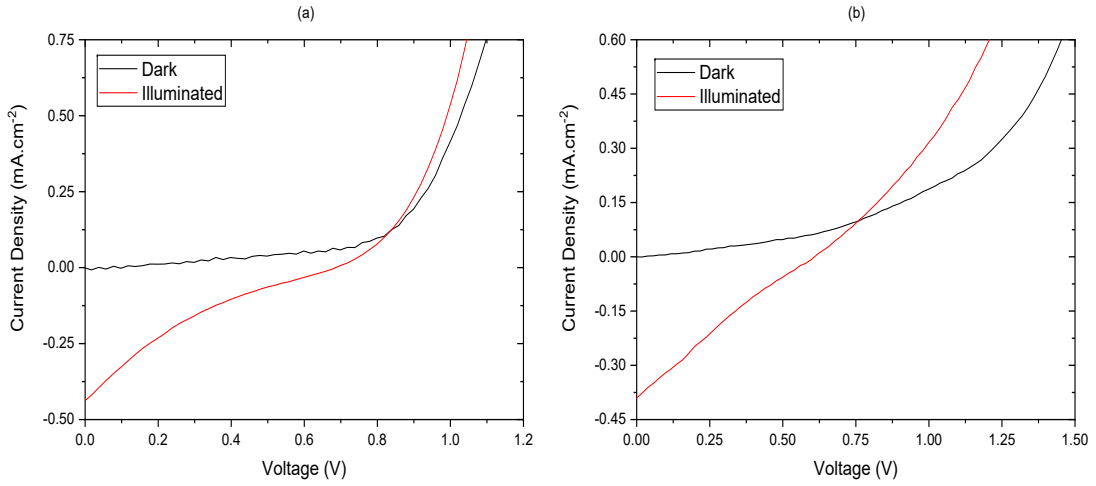

FIGURE 5.6: J-V characteristic of $Cs_3Bi_2I_9$ perovskite solar cells prepared using c-TiO_2 with recipe 1 and recipe 2.

that the highest PCE of 0.067% was obtained from the $Cs_3Bi_2Br_3I_6$ solar cell with V_{oc} of 0.684 V and J_{sc} of 0.211 mA.cm^{-2}, whereas the lowest PCE of 0.016% was recorded from the $Cs_3Bi_2Br_9$ solar cell provided the lowest J_{sc} of 0.077 mA.cm^{-2}.

In Table 5.2, the PCEs of the $Cs_3Bi_2Br_xI_{9-x}$ solar cells were obtained by taking the PSCs with the best photovoltaic performance. The error estimation of the reported efficiencies could be performed considering all data sets with different PCEs of the PSCs structured with the same configuration. The best estimation for the correct value of PCEs would be the mean of the measured values. Additionally, the uncertainty in the mean could be given by the standard error. Therefore, the best estimate of PCE for a specific PSC would be given by the mean of the measurements, and its accuracy would be given by the standard error on the mean. The PCE of the PSC would be demonstrated as mean$\pm$standard error.

Perovskites	**PCE (%)**	J_{sc} $(mA\ cm^{-2})$	V_{oc} **(V)**
$Cs_3Bi_2I_9$	0.058	0.232	0.651
$Cs_3Bi_2BrI_8$	0.051	0.226	0.653
$Cs_3Bi_2Br_2I_7$	0.053	0.226	0.674
$Cs_3Bi_2Br_3I_6$	0.067	0.211	0.684
$Cs_3Bi_2Br_4I_5$	0.056	0.185	0.753
$Cs_3Bi_2Br_6I_3$	0.051	0.173	0.746
$Cs_3Bi_2Br_7I_2$	0.039	0.148	0.755
$Cs_3Bi_2Br_8I$	0.037	0.123	0.776
$Cs_3Bi_2Br_9$	0.016	0.077	0.533

TABLE 5.2: J-V characteristics of $Cs_3Bi_2Br_xI_{9-x}$ perovskite solar cells

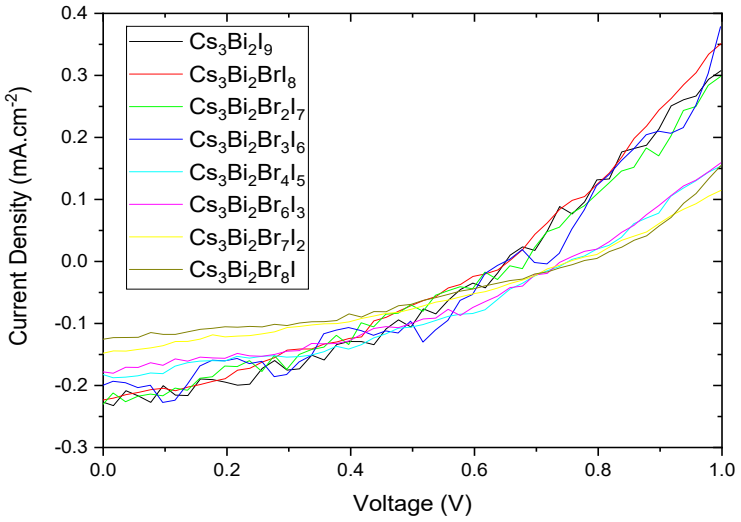

FIGURE 5.7: J-V curves of $Cs_3Bi_2Br_xI_{9-x}$ perovskite solar cells.

5.3 Discussion

This study aimed to investigate UV-vis and J-V characteristics of inorganic Bi-based perovskites of $Cs_3Bi_2Br_xI_{9-x}$ where x was varying from 0 to 9. Therefore, it was targeted to find a perovskite with optimal PV characteristics and to obtain solar cells with improved stability. According to PCE of the Bi-based PSCs, the highest efficiency was obtained from the solar cell with $Cs_3Bi_2Br_3I_6$, which inspired the theoretical investigation of that specific dual halide perovskite in terms of structural, electronic and optical properties given in Chapter 4.

The UV-vis results revealed that the energy band gap of $Cs_3Bi_2I_9$ was 2.00 eV from the Tauc plots using the Kubelka-Munk function with DRS data, which was the same as the indirect band gap value of $Cs_3Bi_2I_9$ obtained from the UV-vis spectrum in a study [120]. Additionally, the experimental band gap value of 2.00 eV was coherent with the theoretically calculated band gap of 1.99 eV using CASTEP. As for the energy band gap of $Cs_3Bi_2Br_9$, it was estimated as 2.68 eV using Tauc plots, which was consistent with the 2.67 eV energy band gap of $Cs_3Bi_2Br_9$ from Tauc plots in a study [127]. Furthermore, the Tauc plots obtained by transmittance spectroscopy data demonstrated that the energy band gaps of $Cs_3Bi_2Br_xI_{9-x}$ perovskites were varying from 1.99 eV to 2.66 eV with changing x value from 0 to 9.

The J-V results showed that the best photovoltaic performance was achieved from the solar cell produced using $Cs_3Bi_2Br_3I_6$ perovskite with the PCE of 0.067%, whereas the lowest PCE was obtained from the $Cs_3Bi_2Br_9$ solar cell with 0.016% PCE. Inorganic halide Bi-based PSCs could not achieve PCE as high as their lead-based counterparts. The highest PCE of 3.2% was obtained from a study on $Cs_3Bi_2I_9$ solar cells with CuI as

HTM so far [19]. However, the PCEs of the $Cs_3Bi_2Br_xI_{9-x}$ PSCs were much lower than expected, which was attributed low current density values of the solar cells. The low current density originated from the poor absorption of the perovskites as light absorbers [128].

5.4 Conclusion

The binary halide bi-based perovskites, $Cs_3Bi_2Br_xI_{9-x}$, were experimentally examined to seek their spectral response and J-V characteristics in solar cells in this study. UV-vis spectra of the $Cs_3Bi_2Br_xI_{9-x}$ perovskites showed that the absorption edges shifted to lower wavelengths when the molar ratio of Br increased. Additionally, the energy band gaps of the $Cs_3Bi_2Br_xI_{9-x}$ perovskites increased with rising the x value in $Cs_3Bi_2Br_xI_{9-x}$ chemical structure. Moreover, the V_{oc} values of the $Cs_3Bi_2Br_xI_{9-x}$ solar cells rose while the molar ratio of Br increased. On the other hand, the J_{sc} values of the $Cs_3Bi_2Br_xI_{9-x}$ solar cells decreased with increasing the x value. Although there were a few studies on $Cs_3Bi_2Br_xI_{9-x}$ PSCs [126, 129, 130], the Bi-based PSCs were not produced using c-TiO_2 and spiro-MeOTAD as ETM and HTM, respectively.

Chapter 6

Degradation Study of $MAPbI_3$/Tint Perovskite Solar Cells

Perovskite solar cells are produced by sandwiching a perovskite film between an ETL and HTL, so charge carriers are collected and transported to electrodes. TiO_2 can be used as an ETM because of its wide band gap, suitable conduction band alignment and great electron-transport ability [131]. In addition to c-TiO_2, mesoporous TiO_2 has gained considerable interest thanks to a striking increase in PCE from a lead-based perovskite solar cell with mesoscopic TiO_2 film [91]. Various mesoporous TiO_2 have been introduced, such as nanosheets, nanowires/nanofibers, nanorods, and nanotubes. It was shown that a lead-based perovskite solar cell with TiO_2 nanotubes performed higher PCE than PCE of the perovskite solar cell produced with TiO_2 nanoparticles [132]. In this study, $MAPbI_3$ perovskites with Tint were employed to fabricate solar cells. The production method of precursors and solar cells with Tint was given Section 3.3.

Perovskites have instability issues under the conditions of moisture, heat, light, oxygen, and electric field [21]. Here, we have introduced a treatment method using MAI to recover degraded $MAPbI_3$/Tint. In this perspective, the degradation and recovery study of the $MAPbI_3$/Tint perovskite solar cells was conducted. Firstly, the UV-vis spectra of precursors were examined, and the energy band gap of $MAPbI_3$/Tint was obtained using the Kubelka-Munk function. Additionally, FTIR spectra of the precursors were investigated. Besides, photovoltaic characteristics of $MAPbI_3$/Tint solar cells were sought before and after degradation and MAI treatment.

6.1 Spectral Response

Diffuse reflectance spectroscopy (DRS) was used to seek the optical properties of Tint, Pb/Tint, PbI_2/Tint, and $MAPbI_3$/Tint precursor powders with different molar ratios between Pb^{2+} and Tint. The UV-vis characteristics of them were given in Figure 6.1.

The absorption spectra of Tint and Pb/Tint with the different ratios were shown in Figure 6.1-(a). The absorption onset wavelength of (2) Pb/Tint was shifted to longer wavelengths compared to Tint. Additionally, a more dramatic red-shift was observed for the absorption onset wavelengths of (1) Pb/Tint and (3) Pb/Tint. The absorption edge of (1) Pb/Tint was 500 nm, while the absorption edge of Tint was 400 nm. As for absorption intensity peaks, there was not considerable difference between Tint and Pb/Tint.

Figure 6.1-(b) illustrates the absorption spectra of PbI_2/Tint powders with different molar ratios between Pb^{2+} and Tint. Although the absorption onset wavelength of 650 nm was the same for all the powders, there was a significant increase in the absorption peaks of (1) PbI_2/Tint and (3) PbI_2/Tint after 550 nm compared to (2) PbI_2/Tint.

The absorption spectra of $MAPbI_3$/Tint perovskites were demonstrated in Figure 6.1-(c). The sharp increase in absorption edges of the perovskites with Tint showed that the perovskites had direct band gap, which was coherent with the direct band gap of the $MAPbI_3$ perovskite [74]. Moreover, there was a significant increase in the absorption intensities of (1) $MAPbI_3$/Tint and (3) $MAPbI_3$/Tint compared to (2) $MAPbI_3$/Tint.

Figure 6.2-(a) shows the absorption spectra of Tint, (1) Pb/Tint, (1) PbI_2/Tint and (1) $MAPbI_3$/Tint. A considerable shift to longer wavelengths was observed in the absorption onset wavelengths of the precursors from Tint to $MAPbI_3$/Tint. The absorption edges were found as 400 nm, 500 nm, 700 nm, and 900 nm for Tint, (1) Pb/Tint, (1) PbI_2/Tint and (1) $MAPbI_3$/Tint, respectively.

The reflectance data of DRS was used to obtain Tauc plots employing Kubelka-Mulk function, and so the energy band gaps of the $MAPbI_3$/Tint perovskites were determined [125]. Accordingly, the energy band gaps of all $MAPbI_3$/Tint perovskites were estimated as 1.56 eV, which was compatible with the 1.5-1.6 eV energy band gap range of $MAPbI_3$ [77]. Figure 6.2-(b) demonstrates the Tauc plot of (1) $MAPbI_3$/Tint.

The diffuse absorbance spectra of fresh-, old-, degraded-, and treated-(1) $MAPbI_3$/Tint powders were demonstrated in Figure 6.3. It was observed that all absorption curves of the perovskites steeply increased around 800 nm, which was attributed to a direct band gap of the lead-based perovskites. The highest absorption intensity and the absorption onset wavelength were obtained from the freshly made (1) $MAPbI_3$/Tint, F-$MAPbI_3$/Tint. The diffuse absorption spectrum of the O-$MAPbI_3$/Tint showed that

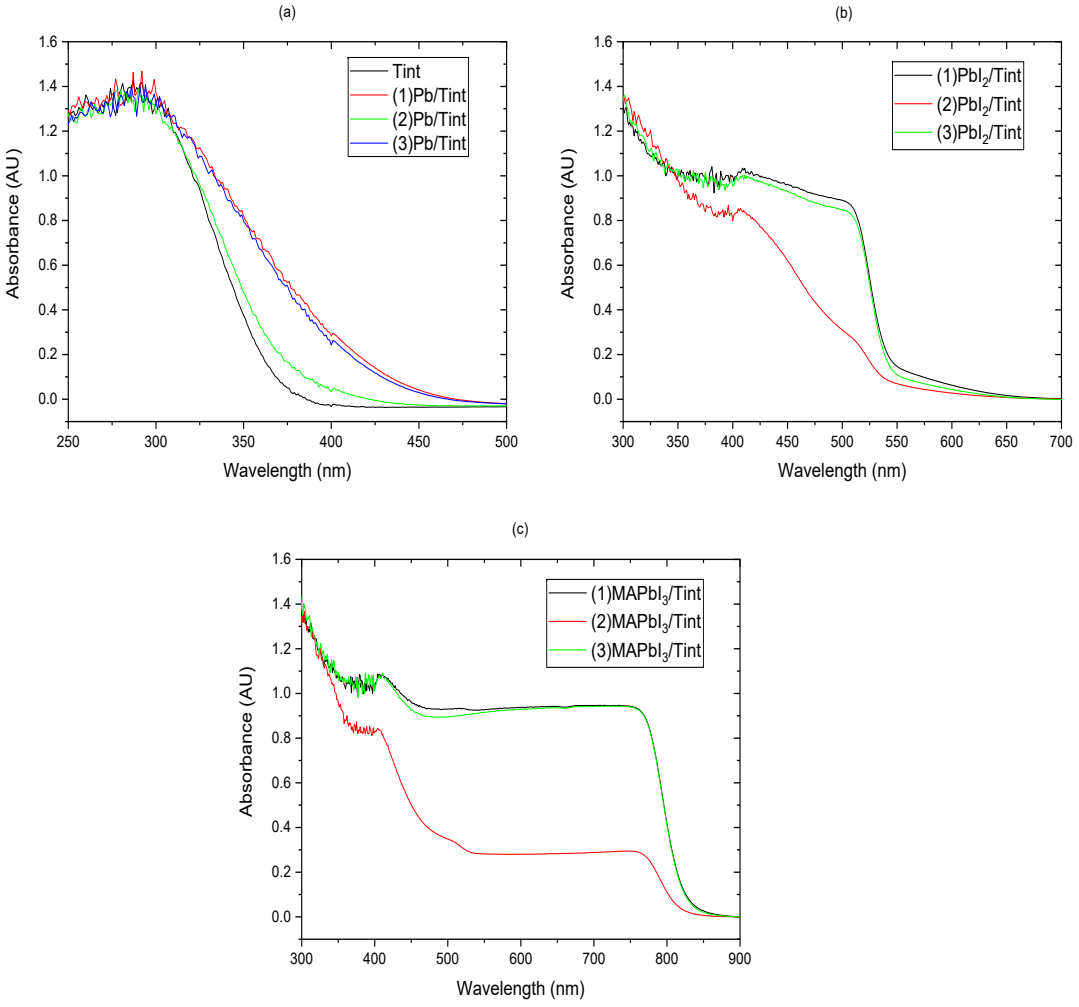

FIGURE 6.1: Absorption spectra of (a) Tint and Pb/Tint, (b) PbI_2/Tint, and (c) $MAPbI_3$/ Tint.

the absorption intensity significantly decreased, while the absorption onset slightly shifted to lower wavelengths compared to the F-$MAPbI_3$/Tint. However, a dramatic decrease in both the absorption intensity and the absorption onset wavelength was observed in degraded-(1) $MAPbI_3$/Tint, D-$MAPbI_3$/Tint. Additionally, the diffuse absorption curve of the D-$MAPbI_3$/Tint had a significant shoulder at 550 nm wavelength, which was compatible with the diffuse absorption onset wavelength of (1) PbI_2/Tint in Figure 6.2-(a). Moreover, it was observed that there was no shoulder in the absorption curves of F-$MAPbI_3$/Tint and T-$MAPbI_3$/Tint at 550 nm in Figure 6.3. The shoulder behaviour of the absorption curves was attributed to the decrease in MAI and increase in PbI_2/Tint in the $MAPbI_3$/Tint perovskite powders. After the treatment with MAI, the shoulder in the diffuse absorption curve disappeared, and the absorption intensity significantly increased. Although the absorption intensity of the treated-(1) $MAPbI_3$/Tint, T-$MAPbI_3$/Tint, did not reach the intensity of F-$MAPbI_3$/Tint, it surpassed the intensity of O-$MAPbI_3$/Tint, which

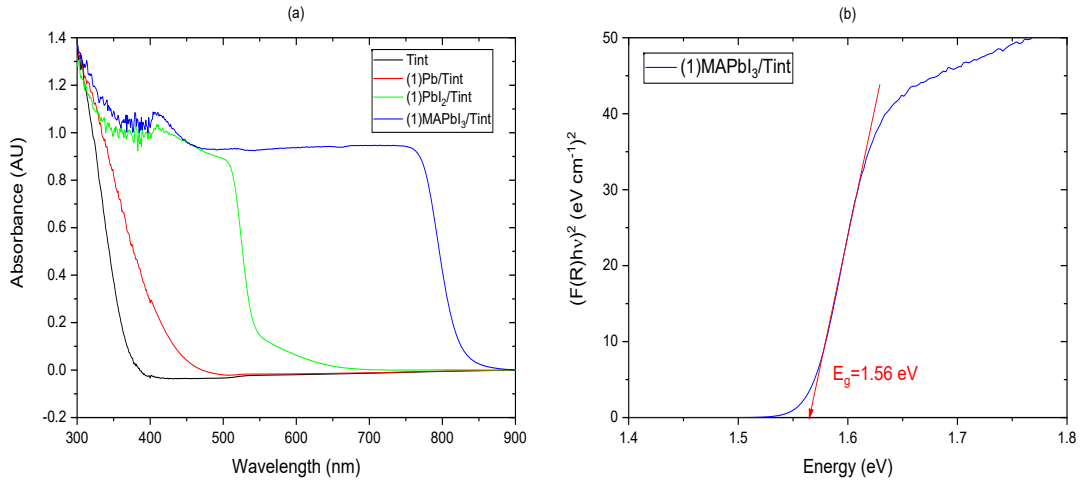

FIGURE 6.2: (a) Absorption spectra of Tint, (1) Pb/Tint, (1) PbI_2/Tint and (1) $MAPbI_3$/Tint, (b) Tauc plot of (1) $MAPbI_3$/Tint.

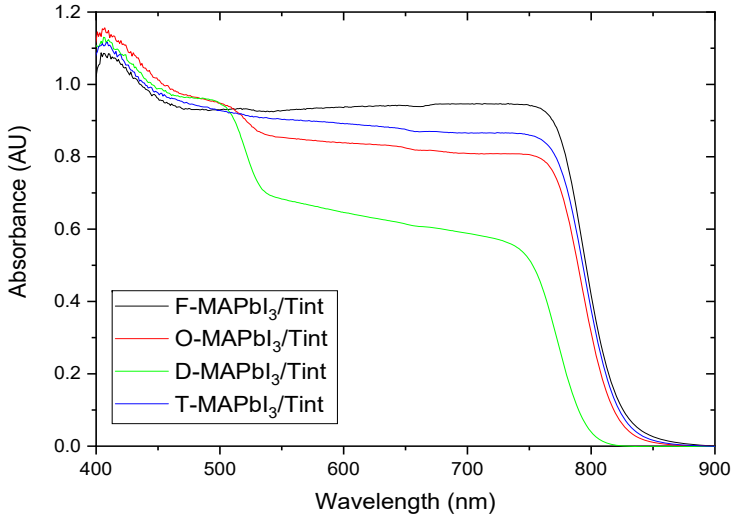

FIGURE 6.3: Absorption spectra of fresh-, old-, degraded-, treated-(1) $MAPbI_3$/Tint.

indicated a significant recovery of D-$MAPbI_3$/Tint.

Fourier-transform infrared (FTIR) spectroscopy was used to seek transmittance spectra of the Tint, Pb/Tint, PbI_2/Tint, and $MAPbI_3$/Tint precursor powders with different molar ratios between Pb^{2+} and Tint. Figure 6.4 demonstrates the FTIR spectra of the Tint, Pb/Tint, and PbI_2/Tint.

The FTIR spectra of Tint, (1) Pb/Tint, (2) Pb/Tint and (3) Pb/Tint were given in Figure 6.4-a. Two significant peaks appeared at the spectra, which were located at the wavenumbers of 3365.02 cm^{-1} and 1645.58 cm^{-1}. The first one was attributed to O-H stretching vibration because of the Tint, while the second one was attributed to H-O-H

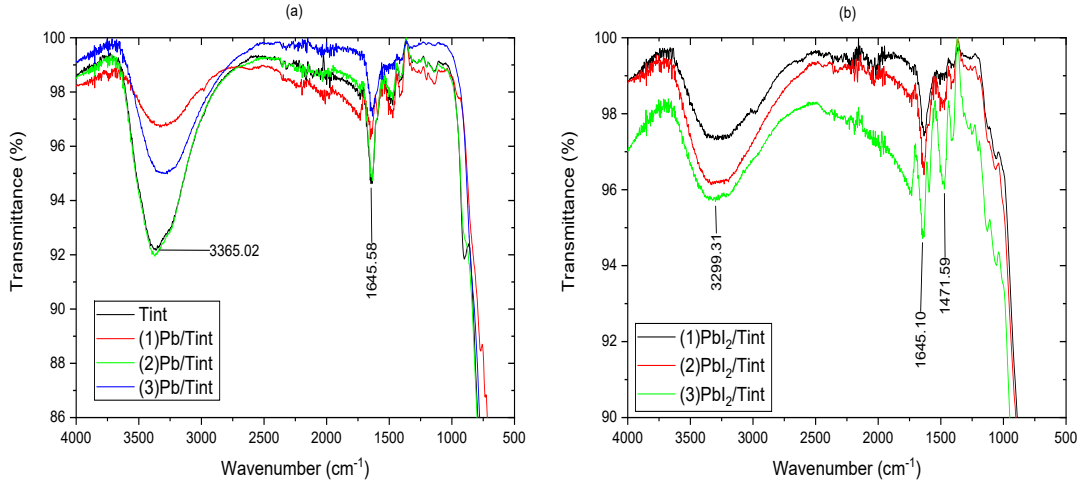

FIGURE 6.4: FTIR spectra of (a) Tint and Pb/Tint, and (b) PbI_2/Tint.

bending owing to the crystalline water in the Tint denoted $H_2Ti_3O_7.xH_2O$. Although the addition of Pb^{2+} did not cause any changes in the peak positions, the peak intensities decreased with increasing Pb^{2+} at 3365.02 cm^{-1}, which was attributed to an increase in the substitution of Pb^{2+} with H^+ during the ion-exchange process.

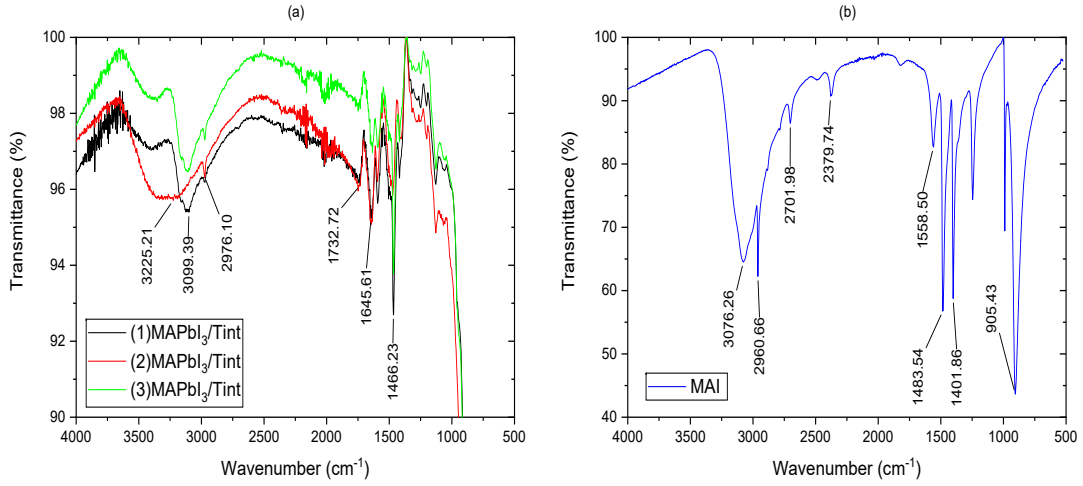

FIGURE 6.5: FTIR spectra of (a) $MAPbI_3$/Tint, and (b) MAI.

Figure 6.4-b illustrates the FTIR spectra of PbI_2/Tint precursors with different molar ratios between Pb^{2+} and Tint. The O-H stretching peak positions of PbI_2/Tint precursor powders shifted to lower wavenumbers, 3299.31 cm^{-1} after the HI addition. The crystalline water contribution remained at the same peak position. Besides, the peak intensities of (1) PbI_2/Tint were the lowest, whereas the (3) PbI_2/Tint peak intensities were the highest throughout the FTIR spectra in Figure 6.4-b.

Figure 6.5 demonstrates the FTIR spectra of (1) $MAPbI_3$/Tint, (2) $MAPbI_3$/Tint, (3) $MAPbI_3$/Tint and MAI. In Figure 6.5-a, it was observed that the MAI addition

significantly affected the peak positions and intensities of $MAPbI_3$/Tint compared to the FTIR spectra of PbI_2/Tint in Figure 6.4-b except for the peak position of H-O-H bending. In Figure 6.5-a, the broad peak of (2) $MAPbI_3$/Tint located around 3225.21 cm^{-1} was attributed to O-H stretching vibration. On the other hand, the sharp peaks of (1) $MAPbI_3$/Tint and (3) $MAPbI_3$/Tint located at 3099.39 cm^{-1} were attributed to N-H stretching vibrations, which were observed at 3076.26 cm^{-1} in Figure 6.5-b. The C-H stretching at 2960.66 cm^{-1} in Figure 6.5-b was observed at 2976.10 cm^{-1} in Figure 6.5-a. Moreover, the C-H bending vibrations were seen in the FTIR spectra of the $MAPbI_3$/Tint perovskites at 1466.23 cm^{-1}, which appeared at 1483.54 cm^{-1} in the FTIR spectra of MAI.

Figure 6.6-a illustrates the changes at the FTIR spectra of the precursor powders from the Tint to $MAPbI_3$/Tint with the 1:1 molar ratio between Pb^{2+} and Tint. The FTIR peak positions attributed to O-H sketching did not change for the Tint, (1) Pb/Tint, (1) PbI_2/Tint, whereas the peak intensities of (1) Pb/Tint and (1) PbI_2/Tint considerably decreased compared to Tint. The peak position of (1) $MAPbI_3$/Tint shifted to higher wavenumbers because of N-H stretching vibrations from MAI. Furthermore, MAI provided C-H bending and C-N stretching vibrations to the (1) $MAPbI_3$/Tint spectra at 1466.23 cm^{-1} and 904.58 cm^{-1}.

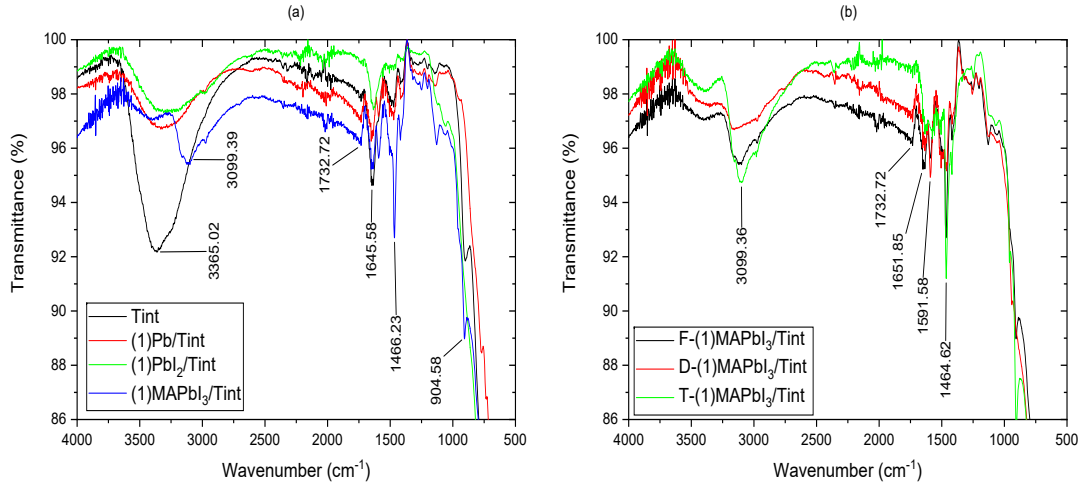

FIGURE 6.6: FTIR spectra of (a) Tint, (1) Pb/Tint, (1) PbI_2/Tint and (1) $MAPbI_3$/Tint, and (b) fresh-(1) $MAPbI_3$/Tint in addition to its degraded and treated versions.

Figure 6.6-b shows the FTIR spectra of fresh- (F-) (1) $MAPbI_3$/Tint along with degraded- (D-) and treated- (T-) (1) $MAPbI_3$/Tint. After the degradation of F-(1) $MAPbI_3$/Tint, the FTIR peak at 3099.36 cm^{-1} shifted to higher wavenumbers, and its peak intensity decreased. However, after the treatment with MAI, the T-(1) $MAPbI_3$/Tint peak position corresponding to N-H stretching vibration recovered. Besides, the peak intensity related to C-H bending vibration at 1464.62 cm^{-1} significantly increased in T-(1) $MAPbI_3$/Tint.

6.2 Current Density-Voltage Characteristics

The photovoltaic characteristics of the solar cells produced using $MAPbI_3$/Tint and PbI_2/Tint as light absorbers were investigated using J-V curves in the dark and under illumination. Additionally, the solar cells exposed to heavy humidity conditions were examined using their J-V characteristics. Moreover, the MAI was used to recover the degraded solar cells, and the photovoltaic performance of the treated solar cells was examined.

6.2.1 $MAPbI_3$/Tint Perovskite Solar Cells

The J-V characteristics of $MAPbI_3$/Tint perovskite solar cells were investigated using spiro-MeOTAD and Al as HTM and counter electrode, respectively. The lead-based perovskite solar cells were examined using $MAPbI_3$/Tint with different molar ratios between Pb^{2+} and Tint. Furthermore, the influence of an additional c-TiO_2 layer on the photovoltaic performance was searched.

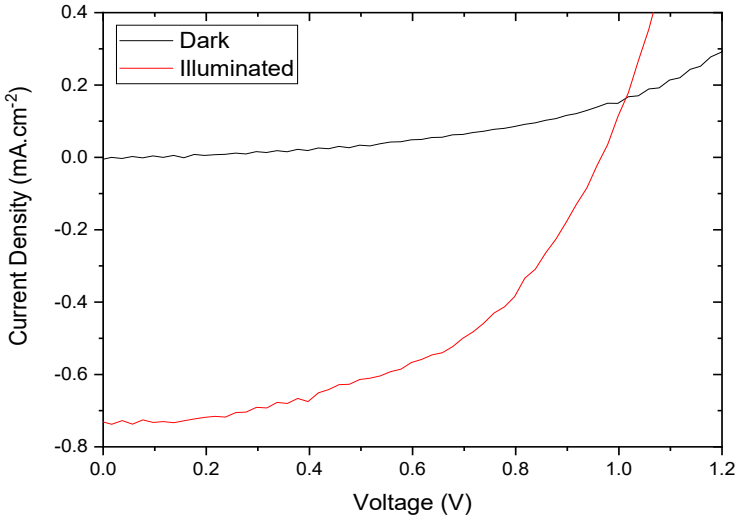

FIGURE 6.7: J-V characteristics of the perovskite solar cell with (1) $MAPbI_3$/Tint.

Figure 6.7 demonstrates the J-V curves of a solar cell with the configuration of ITO-glass/(1) $MAPbI_3$/Tint/spiro-MeOTAD/Al in the dark and under illumination. Although there is not a separate ETL in the configuration, the electrons produced at the absorber layer were successfully transported to the anode thanks to the Tint. The highest PCE obtained from the (1) $MAPbI_3$/Tint perovskite solar cell was recorded as 0.32 % with the values of J_{sc}=0.73 mA.cm^{-2}, V_{oc}=0.96 V, and FF=0.50.
Figure 6.8 illustrates J-V characteristics of the perovskite solar cells structured as ITO-glass/c-TiO_2/perovskite/spiro-MeOTAD/Al using (1) $MAPbI_3$/Tint and (3)

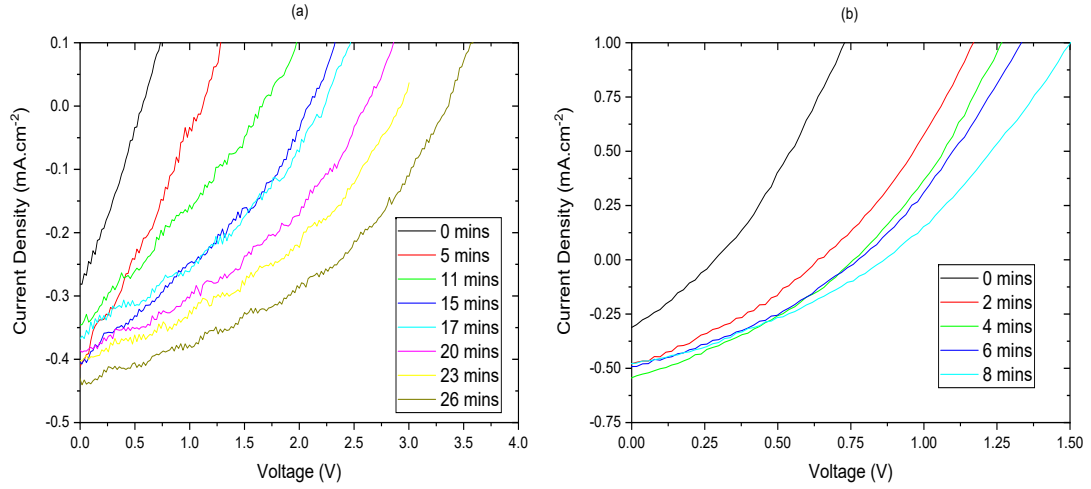

FIGURE 6.8: J-V characteristics of the perovskite solar cells with (a) (1) $MAPbI_3$/Tint and (b) (3) $MAPbI_3$/Tint measured at several minutely intervals under illumination.

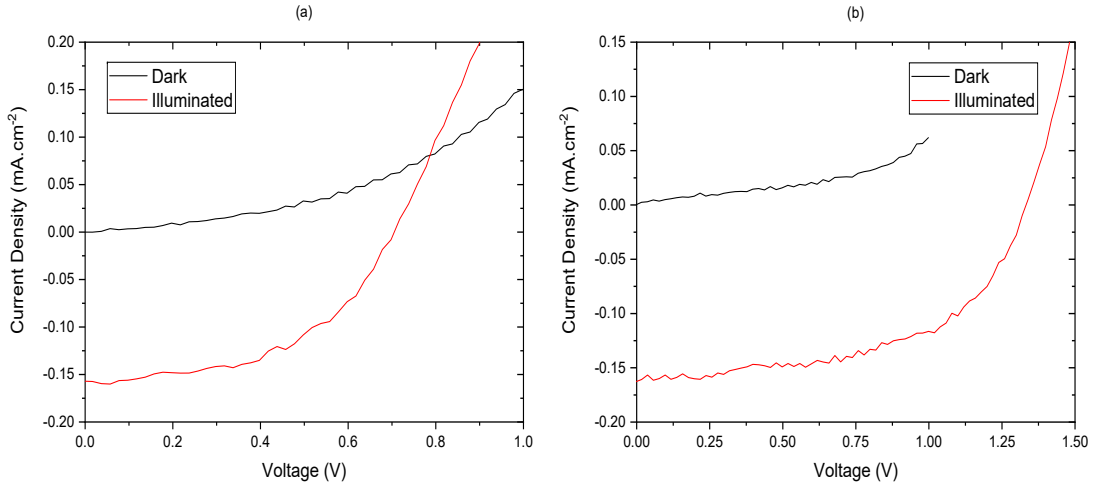

FIGURE 6.9: J-V characteristics of (1) $MAPbI_3$/Tint perovskite solar cells (a) in the absence and (b) in the presence of c-TiO_2 layer.

$MAPbI_3$/Tint under illumination. The solar cells produced using (2) $MAPbI_3$/Tint did not provide proper J-V curves, which was attributed to the low concentration of $Pb2+$ to build perovskite as the light absorber. Figure 6.8-a shows the J-V curves of the (1) $MAPbI_3$/Tint solar cell after sequential interval measurements. It was observed that the V_{oc} value of the solar cell was continuously increasing in time, whereas the J_{sc} value of the cell was varying between 0.28 and 0.44 mA.cm^{-2}. Additionally, the J-V curves of the solar cell with (3) $MAPbI_3$/Tint showed the same tendency for the V_{oc} value towards the minute interval measurements in Figure 6.8-b. However, the J_{sc} value of the cell remained the same at around 0.5 mA.cm^{-2} after 2 minutes.

Figure 6.9 demonstrates the impact of the c-TiO_2 layer in the architecture of the lead-based perovskite solar cells on their performance. Figure 6.9-a shows the J-V

curves of the (1) $MAPbI_3$/Tint solar cell without ETL in the dark and under illumination, while Figure 6.9-b illustrates the J-V curves of the (1) $MAPbI_3$/Tint solar cell with ETL. In Figure 6.9-b, the discontinuity in the J-V curve in the dark originated from an experimental mistake during the measurement, which was that the applied voltage was mistakenly set until 1 V. In the absence of ETL, the PCE of the cell was 0.05 % with J_{sc}=0.16 mA.cm^{-2}, V_{oc}=0.70 V, and FF=0.50, whereas the solar cell with ETL performed twice as much PCE of 0.10 % because of the increase in the V_{oc} value to 1.33 V. The J_{sc} and FF of the solar cell with the *c-*TiO_2 layer was found as 0.16 mA.cm^{-2} and 0.54, respectively.

There was a significant difference between the J-V characteristics of the solar cells with the same configuration, ITO-glass/(1) $MAPbI_3$/Tint/spiro-MeOTAD/Al, in Figure 6.7 and Figure 6.9-a. The results in Figure 6.7 were obtained from the cell produced immediately after the synthesis of (1) $MAPbI_3$/Tint denoted F-(1)$MAPbI_3$/Tint. The photovoltaic performance of the solar cells produced using (1) $MAPbI_3$/Tint deteriorated in time, although the (1) $MAPbI_3$/Tint powder was firmly sealed and saved in the dark. Figure 6.9-a presented the J-V characteristics of the solar cell produced using (1) $MAPbI_3$/Tint sealed several months denoted O-(1) $MAPbI_3$/Tint. The F-(1) $MAPbI_3$/Tint solar cell achieved a PCE of 0.32 %, whereas the PCE of the O-(1) $MAPbI_3$/Tint solar cell was recorded as 0.05 %, which was attributed to the decomposition of $MAPbI_3$ into MAI and PbI_2 [133].

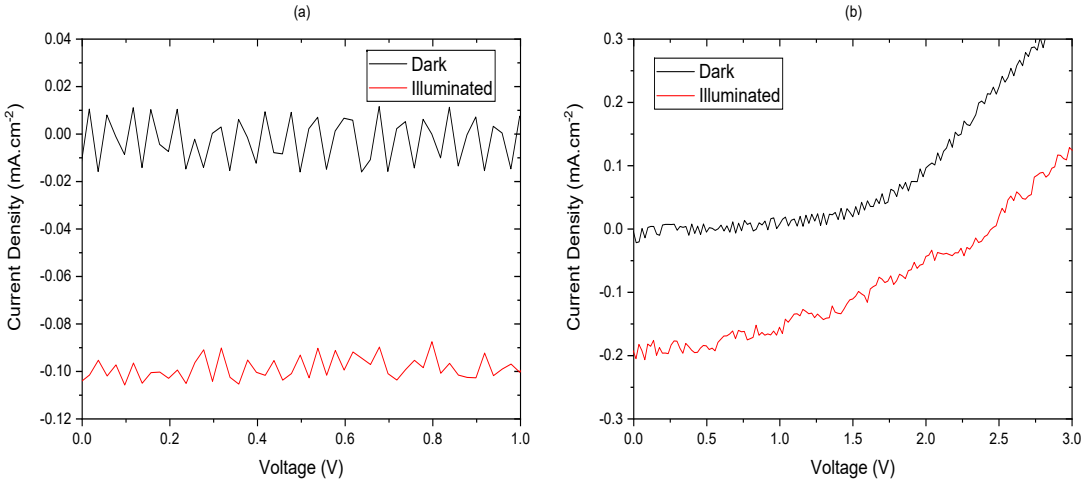

FIGURE 6.10: J-V characteristics of the perovskite solar cells with (a) D-(1) $MAPbI_3$/Tint and (b) T-(1) $MAPbI_3$/Tint.

The O-(1) $MAPbI_3$/Tint solar cell was placed in heavy humidity conditions to be degraded. The J-V characteristics of the degraded solar cell denoted as D-(1) $MAPbI_3$/Tint solar cell is given in Figure 6.10-a. Unexpectedly, the cell generated some current when it was illuminated, although it was degraded. After the MAI treatment of the degraded cell, a significant recovery was observed in the photovoltaic performance of the treated cell denoted the T-(1) $MAPbI_3$/Tint solar cell in

Figure 6.10-b. The T-(1) $MAPbI_3$/Tint solar cell achieved the PCE of 0.19 with the values of J_{sc}=0.20 mA.cm^{-2}, V_{oc}=2.45 V, and FF=0.40.

Figure 6.11 illustrates the J-V characteristics of another degraded perovskite solar cell with (1) $MAPbI_3$/Tint in the dark and under illumination. The J-V curve of the cell under illumination slightly increased when the applied voltage changed from 0 V to 10 V.

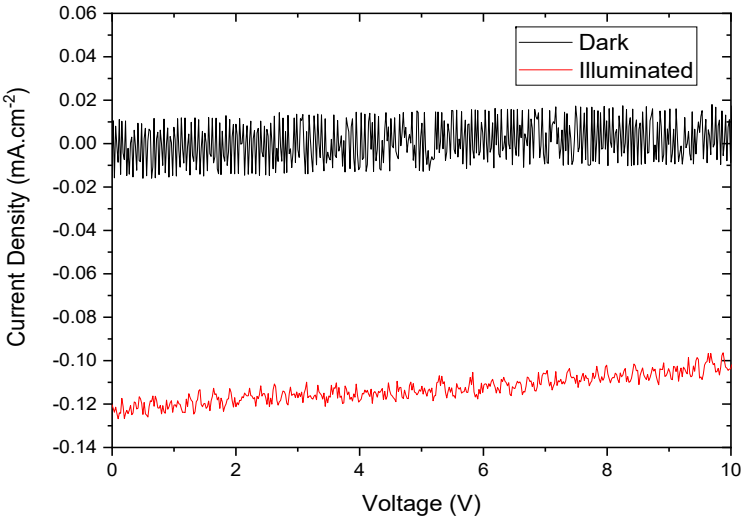

FIGURE 6.11: J-V characteristics of the D-(1) $MAPbI_3$/Tint solar cell exposed to higher voltage.

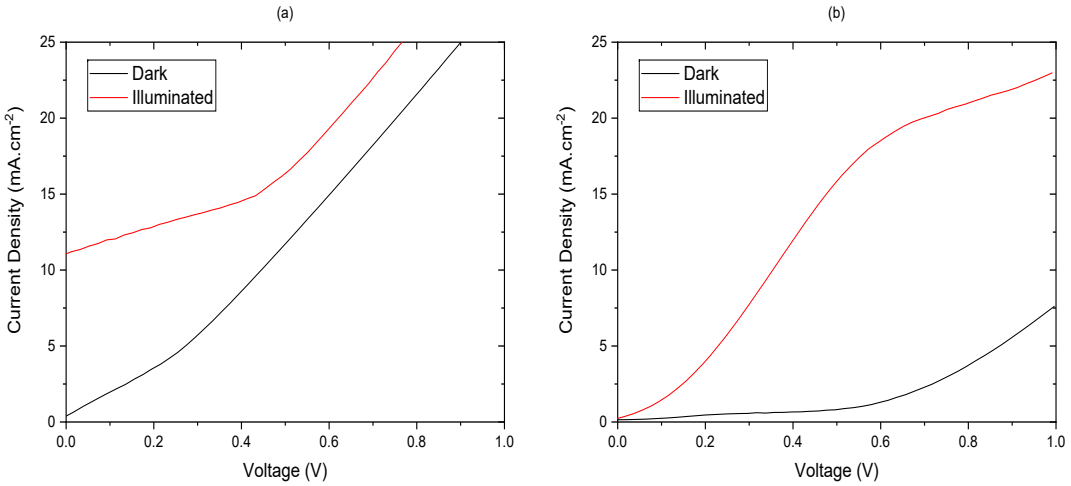

FIGURE 6.12: J-V characteristics of the (1) $MAPbI_3$/Tint solar cells with (a) Cu and (b) Ni as the counter electrode.

Additionally, the counter electrode influence on the performance of the (1) $MAPbI_3$/Tint solar cells was investigated using Cu and Ni instead of Al. The solar cells were constructed with the architecture of ITO-glass/perovskite/spiro-MeOTAD/

counter electrode. The J-V curve of the solar cell with Cu did not show a diode shape in the dark, and it gave positive current under illumination shown in Figure 6.12-a. On the other hand, the solar cell with Ni did not produce current under illumination although the diode-shaped J-V curve was observed in the dark in Figure 6.12-b.

6.2.2 PbI_2/Tint Solar Cells

The (1) PbI_2/Tint precursor was used as the light absorber to fabricate solar cells with the configuration of ITO-glass/light absorber/spiro-MeOTAD/Al. The solar cells provided current under illumination, although they were not produced using perovskites. The (1) PbI_2/Tint layer successfully absorbed the light, and separated charge carriers were collected by the terminals of the cells. Therefore, the (1) PbI_2/Tint solar cells produced current under illumination shown in Figure 6.13.

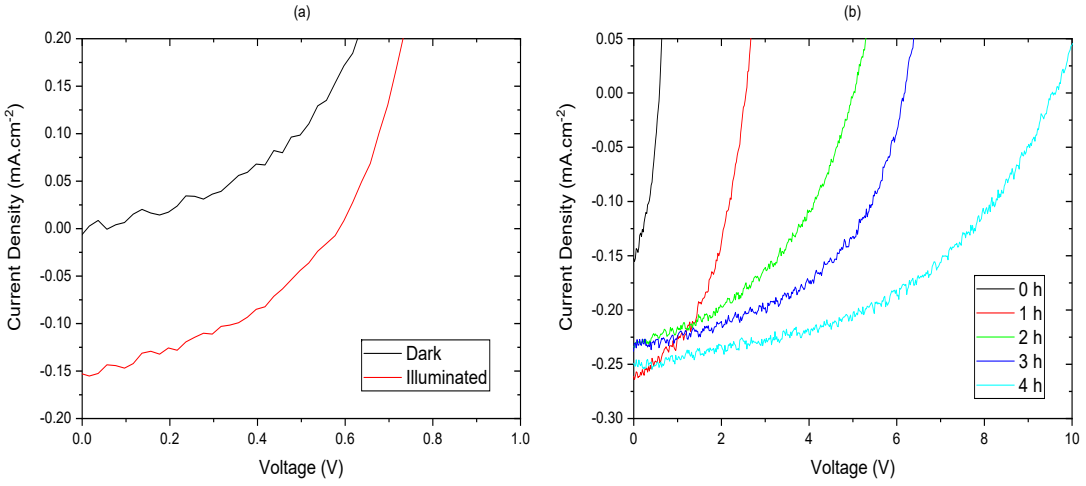

FIGURE 6.13: J-V characteristics of (1) PbI_2/Tint solar cells (a) immediately measured after the preparation and (b) hourly measured under illumination.

Figure 6.13-a demonstrates the J-V curves of a (1) PbI_2/Tint solar cell in the dark and under illumination. The solar cell provided the PCE of 0.035 % with J_{sc}=0.15 mA.cm^{-2}, V_{oc}=0.58 V and FF=0.40. The J-V curves of the solar cell were measured at hour intervals in Figure 6.13-b. The J_{sc} of the cell increased to 0.25 mA.cm^{-2} after an hour and remained almost the same after four hours. On the other hand, the V_{oc} of the cell considerably changed in time. The V_{oc} of 9.59 V was recorded at the fourth hour, whereas it was 0.58 V at the first measurement after preparation. The increase in the V_{oc} was attributed to interactions between PbI_2 and Al.

The photovoltaic characteristics of the (1) PbI_2/Tint solar cell were examined after degradation and treatment using MAI. The J-V characteristics of the degraded-(1) PbI_2/Tint and treated-(1) PbI_2/Tint solar cells were shown in Figure 6.14-a and Figure 6.14-b, respectively. The degraded cell did not provide proper J-V curves in the

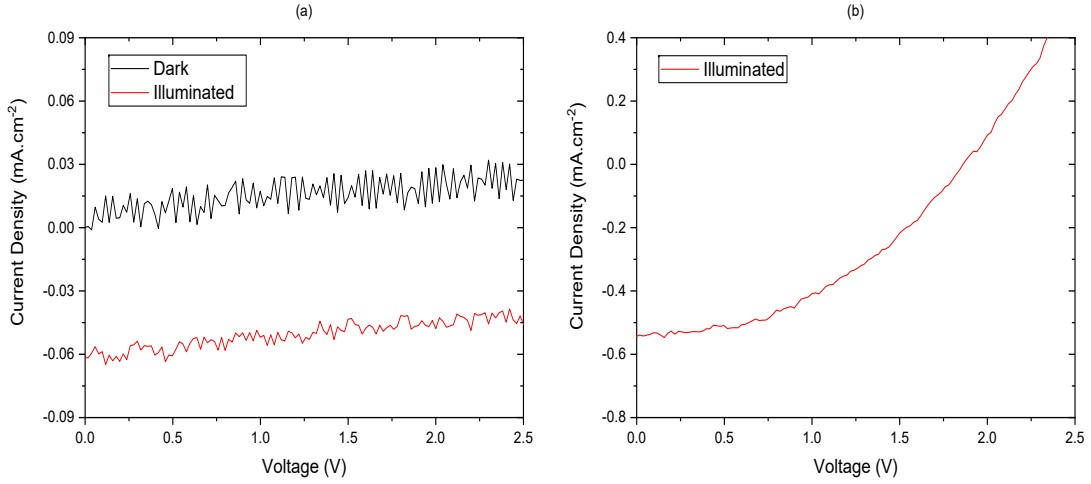

FIGURE 6.14: J-V characteristics of the solar cells with (a) degraded-(1) PbI_2/Tint and (b) treated-(1) PbI_2/Tint.

dark and under illumination. However, it unexpectedly produced some current with J_{sc}=0.06 mA.cm^{-2} under illumination similar to the D-(1) $MAPbI_3$/Tint solar cell in Figure 6.10-a. The solar cell performance of the solar cell significantly improved after the treatment with MAI in Figure 6.14-b. The treated-(1) PbI_2/Tint solar cell achieved the PCE of 0.43 % with J_{sc}=0.55 mA.cm^{-2}, V_{oc}=1.86 V, and FF=0.42.

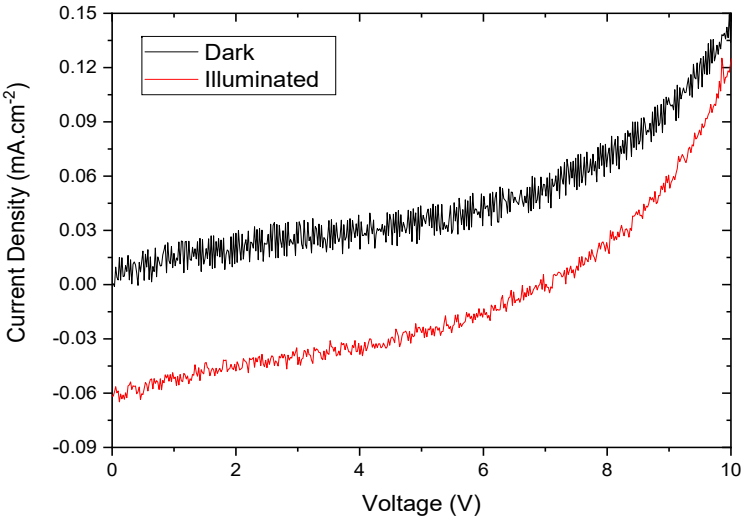

FIGURE 6.15: J-V characteristics of the degraded-(1) PbI_2/Tint solar cell exposed to higher voltage.

Figure 6.15 demonstrates the J-V curves of degraded-(1) PbI_2/Tint solar cell exposed to the external voltage from 0 V to 10 V. The V_{oc} of the cell recorded at 7.1 V, while its J_{sc} was at 0.06 mA.cm^{-2}. Therefore, the degradation caused an increase in V_{oc} and a decrease in J_{sc} compared to the (1) PbI_2/Tint solar cell in Figure 6.13-a. After the MAI

treatment, the V_{oc} of the cell decreased, whereas the J_{sc} considerably rose in Figure 6.14-b.

6.3 Discussion

Enhancements in the stability of perovskites have significant importance in fabricating PSCs with long-lasting PCE. In this study, an experimental method was introduced to recover degraded lead-based PSCs using MAI. It was suggested that MAI treatment would provide a feasible solution to improve the stability of degraded solar cells. Additionally, Tint was combined with the organic-inorganic lead-based perovskite of $MAPbI_3$ with different molar ratios to be utilised as ETM. Therefore, the need for additional ETL in the solar cell configuration was eliminated.

The absorption curves obtained from diffuse reflectance spectroscopy demonstrated that the PbI_2/Tint powders had a strong absorption increase at the wavelength of 550 nm, which was compatible with the optical absorption edge of PbI_2 at 520 nm from optical absorbance spectroscopy in a study [134]. The absorption curve of the $MAPbI_3$/Tint perovskites significantly increased around 800 nm, which was consistent with the absorption edge at ∼800 nm [135]. Additionally, the energy band gap of $MAPbI_3$/Tint was estimated as 1.56 eV from the Tauc plot using the Kubelka-Munk function, which was coherent with the 1.563 eV energy band gap of $MAPbI_3$ obtained from UV-vis absorption spectra in a study [136].

FTIR results of Tint and Pb/Tint showed that two peaks were observed at 3365.02 cm^{-1} and 1645.58 cm^{-1}, which were attributed to the crystalline water in Tint. Therefore, those two peaks originated from O-H stretching and H-O-H bending vibrations, respectively, which were compatible with the O-H stretching in the 3250-3400 cm^{-1} and H-O-H bending at 1645-1660 cm^{-1} in a study [137]. After the formation of PbI_2/Tint, the O-H stretching vibration peak position shifted to 3299.32 cm^{-1}. The FTIR spectra of $MAPbI_3$/Tint perovskites showed that the N-H stretching vibration peak position appeared at 3099.39 cm^{-1}, which were attributed to MAI contribution and consistent with the N-H stretching at 3000-3300 cm^{-1} in a study [138]. Additionally, the vibration peak at 1466.23 cm^{-1} was attributed to the C-H bending vibration and coherent with the C-H bending at 1465 cm^{-1} in a study [139].

The MAI treatment on degraded-$MAPbI_3$/Tint perovskite powders was investigated using UV-vis and FTIR spectroscopy. The UV-vis results showed that the absorption curve of the degraded-$MAPbI_3$/Tint powder had a shoulder at 550 nm, which was attributed to the formation of PbI_2/Tint as a result of MAI lost in the perovskite powder. After the MAI treatment, the shoulder at the absorption curve disappeared and the absorption curve owned the same pattern as the absorption curve of $MAPbI_3$/Tint before the degradation. As for the FTIR results, the transmittance

curves showed that MAI treatment on degraded-$MAPbI_3$/Tint perovskite powder recovered the vibration peak positions at 3099.36 cm^{-1} and 1464.62 cm^{-1}, which were corresponding to N-H stretching and C-H bending vibrations.

6.4 Conclusion

A treatment method for degraded-perovskite solar cells was introduced in this study. The Tint was used as ETM in lead-based perovskites solar cells. The precursors of Pb/Tint and PbI_2/Tint were produced, and $MAPbI_3$/Tint perovskites were synthesised to be used as the light absorber in the solar cells. The spectral response of the precursor powders was examined using UV-vis and FTIR spectroscopy, whereas photovoltaic characteristics of the solar cells were investigated using J-V curves. The diffuse absorption spectra of $MAPbI_3$/Tint showed that the lead-based perovskite had a direct band gap. Besides, the FTIR results showed the peak positions shifted lower wavelengths when the precursors changed from Pb/Tint to PbI_2/Tint and from PbI_2/Tint to $MAPbI_3$/Tint. Spectral results showed that the degraded-$MAPbI_3$/Tint precursor powders almost transformed to their original form after the MAI treatment. Moreover, J-V results showed that $MAPbI_3$/Tint solar cells provided promising PCE under illumination. Furthermore, the treated solar cells significantly recovered their initial photovoltaic properties before degradation. The treatment of MAI and the usage of Tint as ETM in PSCs were first introduced in this study.

Chapter 7

Conclusion

This PhD project aimed to fabricate perovskites with enhanced stability and to evaluate perovskite solar cells utilising computational and experimental methods. Considering the objectives of the project, inorganic halide Bi-based perovskites of $Cs_3Bi_2I_9$, $Cs_3Bi_2Br_9$ and $Cs_3Bi_2Br_3I_6$ were chosen as low-toxic perovskite materials. The structural, electronic and optical properties of the Bi-based perovskites were investigated theoretically using first principles DFT calculations via CASTEP code. Additionally, the wet-chemical synthesis method was used to produce the precursors of the solar cells, while the spin-coating, sputter-coating, and doctor-blading methods were employed to build the layers of the solar cell configurations. Furthermore, $MAPbI_3$ perovskites were combined with Tint to act as the ETM in the lead-based perovskite photovoltaic devices. Moreover, the MAI treatment technique was introduced to recover degraded lead-based perovskite solar cells. The main results of the computational and experimental studies are summarised in the following.

First-principles DFT calculations have been performed to investigate structural, electronic, and optical properties of $Cs_3Bi_2I_9$, $Cs_3Bi_2Br_9$ and $Cs_3Bi_2Br_3I_6$ by CASTEP. The crystal structure of the perovskites showed that both crystallise in the hexagonal space group. The energy band gap of $Cs_3Bi_2I_9$ was obtained as 1.99 eV and 2.00 eV by computational and experimental studies, respectively. The band gap energy of $Cs_3Bi_2Br_9$ was estimated as 2.42 eV by CASTEP, while it was found as 2.68 eV by Tauc plots. Therefore, the band gaps of $Cs_3Bi_2I_9$ from computational and experimental studies are coherent. However, there is a slight difference between the calculated band gap of $Cs_3Bi_2Br_9$ and the value obtained from DRS data. CASTEP code underestimated the energy band gap of $Cs_3Bi_2Br_9$, which can be overcome using a c-double crystal structure of $Cs_3Bi_2Br_9$ as it was used for $Cs_3Bi_2I_9$.

As for the experimental characterisation of the Bi-based perovskites of $Cs_3Bi_2Br_xI_{9-x}$, where x is varying from 0 to 9, the UV-vis spectroscopy was used to elicit the spectral response of the inorganic halide perovskites. Besides, photovoltaic characteristics of

the perovskite solar devices were investigated using an Ossila solar cell I-V test system. The Tauc plots of $Cs_3Bi_2Br_xI_{9-x}$ perovskites showed that their energy band gaps increased with increasing the x value. Additionally, J-V characteristics of the $Cs_3Bi_2Br_xI_{9-x}$ solar cells demonstrated that the perovskite solar cell with $Cs_3Bi_2Br_3I_6$ performed the highest PCE of 0.067% compared to the other Bi-based cells.

The impact of MAI treatment on the photovoltaic characteristics of $MAPbI_3$/Tint solar cells has been investigated. The UV-vis characteristics of Tint, Pb/Tint, PbI_2/Tint, and $MAPbI_3$/Tint have been investigated using diffuse reflectance spectroscopy. The J-V curves of the $MAPbI_3$/Tint solar cells have been obtained for degraded and treated cells in addition to the cells with freshly prepared and previously prepared $MAPbI_3$/Tint. The results have shown that MAI treatment significantly recovered both the diffuse absorbance response of $MAPbI_3$/Tint and J-V characteristics of the $MAPbI_3$/Tint solar cells.

7.1 Publication Plan

It is expected that the findings of this PhD study will yield two research articles on organic and inorganic perovskite solar devices. Two drafts of the articles have been prepared and submitted to the main supervisor for revision. It is expected that they will become suitable for submission and publication in a few months.

The title of the first article draft is 'First-principles calculations on structural, electronic, and optical properties of $Cs_3Bi_2X_9$ (X=Br, I)'. The abstract of the draft is 'Bi-based perovskites are promising materials to be used as light absorbers in solar cells because they provide higher stability and lower toxicity compared to lead-based counterparts. Thus, they have attracted the attention of researchers in the realm of photovoltaic devices. In this study, two inorganic Bi-based perovskites, $Cs_3Bi_2I_9$ and $Cs_3Bi_2Br_9$, have been investigated in terms of their structural, electronic, and optical properties using first-principles calculations with Cambridge Serial Total Energy Package (CASTEP). Additionally, the UV-vis characteristics of the perovskites have been examined using diffuse reflectance spectroscopy (DRS) and transmittance spectroscopy. Results showed that the computational results for CASTEP were coherent with the experimental results.'.

As for the second article, the title of the second article draft is 'The investigation into MAI treatment on $MAPbI_3$ solar cells with titanate nanotubes'. The abstract of the second article draft is 'We have investigated the effect of MAI treatment on the photovoltaic characteristics of $MAPbI_3$ solar cells with titanate nanotubes. The UV-Vis characteristics of the precursor powders with titanate nanotubes have been reported. Besides, the current density-voltage characteristics of the $MAPbI_3$ solar cells have been examined before and after the MAI treatment on degraded cells. The results

reveal that the MAI treatment recovers the optical and photovoltaic properties of the $MAPbI_3$ with titanate nanotubes.'.

7.2 Future Work

In this study, three different Bi-based perovskites, $Cs_3Bi_2I_9$, $Cs_3Bi_2Br_9$, and $Cs_3Bi_2Br_3I_6$, were theoretically examined in terms of crystal structure, electronic band structure, density of states, joint density of states, and absorption coefficient with the help of DFT via CASTEP. In the next stage of the computational study, the other low-toxic binary halide Bi-based perovskites, in which bromine substitution for iodine is performed, will be investigated using CASTEP. Therefore, the theoretical results of $Cs_3Bi_2Br_xI_{9-x}$ perovskites, where x varies from 0 to 9, will be compared to the experimental results of this study.

The spectral results of the Bi-based perovskites were obtained from UV-vis spectroscopy and showed that energy band gaps of the perovskites were compatible with the findings in the literature. Nevertheless, the performance of produced Bi-based PSCs was lower compared to the ones in the literature. The reason for the poor photovoltaic performance might be problems in the preparation procedure of the precursors. XPS will be used to check if the precursors are prepared as intended. Thus, XPS will be a useful tool to control Br substitution in $Cs_3Bi_2Br_xI_{9-x}$.

Additionally, the energy band alignment between adjacent layers in the solar cell architecture has great importance in facilitating charge carrier movement. The disagreement between the conduction band minima and/or valence band maxima of the precursors might have caused the poor performance. An energy level diagram will be outlined to examine if electron and hole movements face any obstacles related to conflicts in band levels of adjacent layers. UPS will be used to investigate the valence band edges of the precursors. Furthermore, the organic hole transport material, spiro-MeOTAD, was used in the preparation of Bi-based PSCs. The inorganic hole transport materials of CuI and $CuSCN$ will be utilised in addition to spiro-MeOTAD. Energy band edges of the inorganic counterparts will be determined by employing UPS.

The production techniques have great importance for the fabrication of solar cells with high performance. The commonly used spin-coating method was used to build all layers in the Bi-based PSCs architecture except the counter electrode layer, which was performed via the sputter-coating method. Additionally, the doctor-blading method was used to fabricate $MAPbI_3$/Tint perovskites solar devices. The cell production details will be revised to improve the photovoltaic performance. Besides, SEM will be used to observe film coverage quality and film thickness of PSCs. Therefore, the

morphology of the layers will be investigated to facilitate charge carrier movement and improve PV performance.

References

[1] N. Panwar, S. Kaushik, and S. Kothari, "Role of renewable energy sources in environmental protection: A review," *Renewable and sustainable energy reviews*, vol. 15, no. 3, pp. 1513–1524, 2011.

[2] V. Sebestyén, "Renewable and sustainable energy reviews: Environmental impact networks of renewable energy power plants," *Renewable and Sustainable Energy Reviews*, vol. 151, p. 111626, 2021.

[3] A. Angelis-Dimakis, M. Biberacher, J. Dominguez, G. Fiorese, S. Gadocha, E. Gnansounou, G. Guariso, A. Kartalidis, L. Panichelli, I. Pinedo *et al.*, "Methods and tools to evaluate the availability of renewable energy sources," *Renewable and sustainable energy reviews*, vol. 15, no. 2, pp. 1182–1200, 2011.

[4] S. Sen and S. Ganguly, "Opportunities, barriers and issues with renewable energy development–a discussion," *Renewable and Sustainable Energy Reviews*, vol. 69, pp. 1170–1181, 2017.

[5] S. K. Dash, S. Chakraborty, and D. Elangovan, "A brief review of hydrogen production methods and their challenges," *Energies*, vol. 16, no. 3, p. 1141, 2023.

[6] A. I. Osman, L. Chen, M. Yang, G. Msigwa, M. Farghali, S. Fawzy, D. W. Rooney, and P.-S. Yap, "Cost, environmental impact, and resilience of renewable energy under a changing climate: a review," *Environmental Chemistry Letters*, vol. 21, no. 2, pp. 741–764, 2023.

[7] M. Tawalbeh, A. Al-Othman, F. Kafiah, E. Abdelsalam, F. Almomani, and M. Alkasrawi, "Environmental impacts of solar photovoltaic systems: A critical review of recent progress and future outlook," *Science of The Total Environment*, vol. 759, p. 143528, 2021.

[8] O. A. Al-Shahri, F. B. Ismail, M. Hannan, M. H. Lipu, A. Q. Al-Shetwi, R. Begum, N. F. Al-Muhsen, and E. Soujeri, "Solar photovoltaic energy optimization methods, challenges and issues: A comprehensive review," *Journal of Cleaner Production*, vol. 284, p. 125465, 2021.

[9] A. Olabi and M. A. Abdelkareem, "Renewable energy and climate change," *Renewable and Sustainable Energy Reviews*, vol. 158, p. 112111, 2022.

[10] A. Kojima, K. Teshima, Y. Shirai, and T. Miyasaka, "Organometal halide perovskites as visible-light sensitizers for photovoltaic cells," *Journal of the american chemical society*, vol. 131, no. 17, pp. 6050–6051, 2009.

[11] Q. Tai, K.-C. Tang, and F. Yan, "Recent progress of inorganic perovskite solar cells," *Energy & Environmental Science*, vol. 12, pp. 2375–2405, 2019.

[12] Y. Ma and Q. Zhao, "A strategic review on processing routes towards scalable fabrication of perovskite solar cells," *Journal of Energy Chemistry*, vol. 64, pp. 538–560, 2022.

[13] N.-G. Park and K. Zhu, "Scalable fabrication and coating methods for perovskite solar cells and solar modules," *Nature Reviews Materials*, vol. 5, no. 5, pp. 333–350, 2020.

[14] Z. Li, T. R. Klein, D. H. Kim, M. Yang, J. J. Berry, M. F. Van Hest, and K. Zhu, "Scalable fabrication of perovskite solar cells," *Nature Reviews Materials*, vol. 3, no. 4, pp. 1–20, 2018.

[15] F. Fu, J. Li, T. C.-J. Yang, H. Liang, A. Faes, Q. Jeangros, C. Ballif, and Y. Hou, "Monolithic perovskite-silicon tandem solar cells: from the lab to fab?" *Advanced materials*, vol. 34, no. 24, p. 2106540, 2022.

[16] R. Pandey, S. Bhattarai, K. Sharma, J. Madan, A. K. Al-Mousoi, M. K. Mohammed, and M. K. Hossain, "Halide composition engineered a non-toxic perovskite–silicon tandem solar cell with 30.7% conversion efficiency," *ACS Applied Electronic Materials*, 2023.

[17] F. Huang, M. Li, P. Siffalovic, G. Cao, and J. Tian, "From scalable solution fabrication of perovskite films towards commercialization of solar cells," *Energy & Environmental Science*, vol. 12, no. 2, pp. 518–549, 2019.

[18] G. E. Eperon, S. D. Stranks, C. Menelaou, M. B. Johnston, L. M. Herz, and H. J. Snaith, "Formamidinium lead trihalide a broadly tunable perovskite for efficient planar heterojunction solar cells," *Energy & Environmental Science*, vol. 7, pp. 982–988, 2014.

[19] F. Bai, Y. Hu, Y. Hu, T. Qiu, X. Miao, and S. Zhang, "Lead-free, air-stable ultrathin cs3bi2i9 perovskite nanosheets for solar cells," *Solar energy materials and solar cells*, vol. 184, pp. 15–21, 2018.

[20] Y. Wang, M. I. Dar, L. K. Ono, T. Zhang, M. Kan, Y. Li, L. Zhang, X. Wang, Y. Yang, X. Gao, Y. Qi, M. Grätzel, and Y. Zhao, "Thermodynamically stabilized

$\beta - CsPbI_3$-based perovskite solar cells with efficiencies $> 18\%$," *Science*, vol. 365, pp. 591–595, 2019.

[21] S. Yang, S. Chen, E. Mosconi, Y. Fang, X. Xiao, C. Wang, Y. Zhou, Z. Yu, J. Zhao, Y. Gao *et al.*, "Stabilizing halide perovskite surfaces for solar cell operation with wide-bandgap lead oxysalts," *Science*, vol. 365, no. 6452, pp. 473–478, 2019.

[22] Z. Li, M. Yang, J.-S. Park, S.-H. Wei, J. J. Berry, and K. Zhu, "Stabilizing perovskite structures by tuning tolerance factor: formation of formamidinium and cesium lead iodide solid-state alloys," *Chemistry of Materials*, vol. 28, no. 1, pp. 284–292, 2016.

[23] C. J. Bartel, C. Sutton, B. R. Goldsmith, R. Ouyang, C. B. Musgrave, L. M. Ghiringhelli, and M. Scheffler, "New tolerance factor to predict the stability of perovskite oxides and halides," *Science advances*, vol. 5, no. 2, p. eaav0693, 2019.

[24] M. Lyu, J.-H. Yun, M. Cai, Y. Jiao, P. V. Bernhardt, M. Zhang, Q. Wang, A. Du, H. Wang, G. Liu *et al.*, "Organic–inorganic bismuth (iii)-based material: A lead-free, air-stable and solution-processable light-absorber beyond organolead perovskites," *Nano Research*, vol. 9, pp. 692–702, 2016.

[25] P. Gao, M. Grätzel, and M. K. Nazeeruddin, "Organohalide lead perovskites for photovoltaic applications," *Energy & Environmental Science*, vol. 7, pp. 2448–2463, 2014.

[26] N.-G. Park, "Organometal perovskite light absorbers toward a 20% efficiency low-cost solid-state mesoscopic solar cell," *The Journal of Physical Chemistry Letters*, vol. 4, pp. 2423–2429, 2013.

[27] S. A. Veldhuis, P. P. Boix, N. Yantara, M. Li, T. C. Sum, N. Mathews, and S. G. Mhaisalkar, "Perovskite materials for light-emitting diodes and lasers," *Advanced Materials*, vol. 28, pp. 6804–6834, 2016.

[28] T. C. Sum and N. Mathews, "Advancements in perovskite solar cells photophysics behind the photovoltaics," *Energy & Environmental Science*, vol. 7, pp. 2518–2534, 2014.

[29] Y. Chen, L. Zhang, Y. Zhang, H. Gao, and H. Yan, "Large-area perovskite solar cells–a review of recent progress and issues," *RSC advances*, vol. 8, no. 19, pp. 10 489–10 508, 2018.

[30] J.-P. Correa-Baena, A. Abate, M. Saliba, W. Tress, T. J. Jacobsson, M. Grätzel, and A. Hagfeldt, "The rapid evolution of highly efficient perovskite solar cells," *Energy & Environmental Science*, vol. 10, pp. 710–727, 2017.

[31] T. A. Berhe, W.-N. Su, C.-H. Chen, C.-J. Pan, J.-H. Cheng, H.-M. Chen, M.-C. Tsai, L.-Y. Chen, A. A. Dubale, and B.-J. Hwang, "Organometal halide

perovskite solar cells degradation and stability," *Energy & Environmental Science*, vol. 9, pp. 323–356, 2016.

[32] M. A. Green, A. Ho-Baillie, and H. J. Snaith, "The emergence of perovskite solar cells," *Nature Photonics*, vol. 8, pp. 506–514, 2014.

[33] P. J. Hasnip, K. Refson, M. I. J. Probert, J. R. Yates, S. J. Clark, and C. J. Pickard, "Density functional theory in the solid state," *Philosophical Transactions of The Royal Society A*, vol. 372, no. 20130270, 2014.

[34] S. J. Clark, M. D. Segall, C. J. Pickard, P. J. Hasnip, M. I. J. Probert, K. Refson, and M. C. Payne, "First principles methods using castep," *Zeitschrift für Kristallographie*, vol. 220, pp. 567–570, 2005.

[35] M. D. Segall, P. J. D. Lindan, M. J. Probert, C. J. Pickard, P. J. Hasnip, S. J. Clark, and M. C. Payne, "First-principles simulation: ideas, illustrations and the castep code," *Journal of Physics: Condensed Matter*, vol. 14, pp. 2717–2744, 2002.

[36] W. Kohn and L. J. Sham, "Self-consistent equations including exchange and correlation effects," *Physical Review*, vol. 140, no. 4A, pp. 1133–1138, 1965.

[37] T. Markvart, *Solar electricity*. John Wiley & Sons, 2000, vol. 6.

[38] D. Neamen, *Semiconductor physics and devices*. McGraw-Hill, Inc., 2002.

[39] G. Parker, *Introductory semiconductor device physics*. CRC Press, 2004.

[40] M. Grundmann, *Physics of semiconductors*. Springer, 2010, vol. 11.

[41] A. Goetzberger, J. Knobloch, and B. Voss, "Crystalline silicon solar cells," *New York*, pp. 114–118, 1998.

[42] A. Fahrenbruch and R. Bube, *Fundamentals of solar cells: photovoltaic solar energy conversion*. Elsevier, 2012.

[43] M. A. Green, "Solar cells: operating principles, technology, and system applications," *ph*, 1982.

[44] D. Abou-Ras, T. Kirchartz, and U. Rau, *Advanced characterization techniques for thin film solar cells*. Wiley Online Library, 2011, vol. 2.

[45] F. Gao, *Advanced nanomaterials for solar cells and light emitting diodes*. Elsevier, 2019.

[46] S. M. Sze and K. K. Ng, *Physics of semiconductor devices*. John wiley & sons, 2006.

[47] M. D. Archer and M. A. Green, *Clean electricity from photovoltaics*. World Scientific, 2001, vol. 1.

[48] E. L. Wolf, *Nanophysics of solar and renewable energy*. John Wiley & Sons, 2012.

[49] T. Markvart, A. McEvoy, and L. Castaner, *Practical handbook of photovoltaics: fundamentals and applications*. Elsevier, 2003.

[50] J. L. Liu and S. Bashir, "Advanced nanomaterials and their applications in renewable energy," 2015.

[51] N.-G. Park, T. Miyasaka, and M. Grätzel, "Organic-inorganic halide perovskite photovoltaics," *Cham, Switzerland: Springer*, 2016.

[52] I. Yahyaoui, *Advances in renewable energies and power technologies: volume 1: solar and wind energies*. Elsevier, 2018.

[53] S. Kalogirou, *McEvoy's handbook of photovoltaics: fundamentals and applications*. Academic Press, 2017.

[54] A. McEvoy, L. Castaner, and T. Markvart, *Solar cells: materials, manufacture and operation*. Academic Press, 2012.

[55] W. S. Yang, J. H. Noh, N. J. Jeon, Y. C. Kim, S. Ryu, J. Seo, and S. I. Seok, "High-performance photovoltaic perovskite layers fabricated through intramolecular exchange," *Science*, vol. 348, no. 6240, pp. 1234–1237, 2015.

[56] J. Seo, S. Park, Y. C. Kim, N. J. Jeon, J. H. Noh, S. C. Yoon, and S. I. Seok, "Benefits of very thin pcbm and lif layers for solution-processed p-i-n perovskite solar cells," *Energy & Environmental Science*, vol. 7, pp. 2642–2646, 2014.

[57] I. Hussain, H. P. Tran, J. Jaksik, J. Moore, N. Islam, and M. J. Uddin, "Functional materials, device architecture, and flexibility of perovskite solar cell," *Emergent Materials*, vol. 1, pp. 133–154, 2018.

[58] W. Chen, Y. Wu, Y. Yue, J. Liu, W. Zhang, X. Yang, H. Chen, E. Bi, I. Ashraful, M. Grätzel, and L. Han, "Efficient and stable large-area perovskite solar cells with inorganic charge extraction layers," *Science*, vol. 350, no. 6263, pp. 944–948, 2015.

[59] X. Li, D. Bi, C. Yi, J.-D. Dècoppet, J. Luo, S. M. Zakeeruddin, A. Hagfeldt, and M. Grätzel, "A vacuum flash-assisted solution process for high-efficiency large-area perovskite solar cells," *Science*, vol. 353, no. 6294, pp. 58–62, 2016.

[60] M. Liu, M. B. Johnston, and H. J. Snaith, "Efficient planar heterojunction perovskite solar cells by vapour deposition," *Nature*, vol. 501, pp. 395–398, 2013.

[61] H. Zhou, Q. Chen, G. Li, S. Luo, T. bing Song, H.-S. Duan, Z. Hong, J. You, Y. Liu, and Y. Yang, "Interface engineering of highly efficient perovskite solar cells," *Science*, vol. 345, no. 6196, pp. 542–546, 2014.

[62] D. Liu and T. L. Kelly, "Perovskite solar cells with a planar heterojunction structure prepared using room-temperature solution processing techniques," *Nature Photonics*, vol. 8, pp. 133–138, 2014.

[63] M. M. Lee, J. Teuscher, T. Miyasaka, T. N. Murakami, and H. J. Snaith, "Efficient hybrid solar cells based on meso-superstructured organometal halide perovskites," *Science*, vol. 338, pp. 643–647, 2012.

[64] J. You, L. Meng, T.-B. Song, T.-F. Guo, Y. M. Yang, W.-H. Chang, Z. Hong, H. Chen, H. Zhou, Q. Chen, Y. Liu, N. D. Marco, and Y. Yang, "Improved air stability of perovskite solar cells via solution-processed metal oxide transport layers," *Nature Nanotechnology*, vol. 11, pp. 75–81, 2016.

[65] H. S. Jung and N.-G. Park, "Perovskite solar cells From materials to devices," *Nano Small Micro*, vol. 11, no. 1, pp. 10–25, 2015.

[66] G. Xing, N. Mathews, S. Sun, S. S. Lim, Y. M. Lam, M. Grätzel, S. Mhaisalkar, and T. C. Sum, "Long-range balanced electronand hole-transport lengths in organic-inorganic $(CH_3NH_3)PbI_3$," *Science*, vol. 342, pp. 344–347, 2013.

[67] J. A. Christians, R. C. M. Fung, and P. V. Kamat, "An inorganic hole conductor for organo-lead halide perovskite solar cells. improved hole conductivity with copper iodide," *Journal of the American Chemical Society*, vol. 136, pp. 758–764, 2014.

[68] J. H. Heo, S. H. Im, J. H. Noh, T. N. Mandal, C.-S. Lim, J. A. Chang, Y. H. Lee, H. jung Kim, A. Sarkar, M. K. Nazeeruddin, M. Grätzel, and S. I. Seok, "Efficient inorganic-organic hybrid heterojunction solar cells containing perovskite compound and polymeric hole conductors," *Nature Photonics*, vol. 7, pp. 486–491, 2013.

[69] L. Etgar, P. Gao, Z. Xue, Q. Peng, A. K. Chandiran, B. Liu, M. K. Nazeeruddin, and M. Grätzel, "Mesoscopic $CH_3NH_3PbI_3/TiO_2$ heterojunction solar cells," *Journal of the American Chemical Society*, vol. 134, pp. 17 396–17 399, 2012.

[70] N. J. Jeon, J. H. Noh, Y. C. Kim, W. S. Yang, S. Ryu, and S. I. Seok, "Solvent engineering for high-performance inorganic-organic hybrid perovskite solar cells," *Nature Materials*, vol. 13, pp. 897–903, 2014.

[71] Q. Chen, H. Zhou, Z. Hong, S. Luo, H.-S. Duan, H.-H. Wang, Y. Liu, G. Li, and Y. Yang, "Planar heterojunction perovskite solar cells via vapor-assisted solution process," *Journal of the American Chemical Society*, vol. 136, pp. 622–625, 2014.

[72] M. Xiao, F. Huang, W. Huang, Y. Dkhissi, Y. Zhu, J. Etheridge, A. Gray-Weale, U. Bach, Y.-B. Cheng, and L. Spiccia, "A fast deposition-crystallization procedure for highly efficient lead iodide perovskite thin-film solar cells," *Angewandte Chemie*, vol. 53, pp. 9898–9903, 2014.

[73] W. Nie, H. Tsai, R. Asadpour, J.-C. Blancon, A. J. Neukirch, G. Gupta, J. J. Crochet, M. Chhowalla, S. Tretiak, M. A. Alam, H.-L. Wang, and A. D. Mohite, "High-efficiency solution-processed perovskite solar cells with millimeter-scale grains," *Science*, vol. 347, no. 6221, pp. 522–525, 2015.

[74] C. C. Stoumpos, C. D. Malliakas, and M. G. Kanatzidis, "Semiconducting tin and lead iodide perovskites with organic cations: phase transitions, high mobilities, and near-infrared photoluminescent properties," *Inorganic chemistry*, vol. 52, no. 15, pp. 9019–9038, 2013.

[75] Y. Ogomi, A. Morita, S. Tsukamoto, T. Saitho, N. Fujikawa, Q. Shen, T. Toyoda, K. Yoshino, S. S. Pandey, T. Ma, and S. Hayase, "$CH_3NH_3Sn_xPb_{(1-x)}I_3$ perovskite solar cells covering up to 1060 nm," *The Journal of Physical Chemistry Letters*, vol. 5, pp. 1004–1011, 2014.

[76] F. Hao, C. C. Stoumpos, R. P. H. Chang, and M. G. Kanatzidis, "Anomalous band gap behavior in mixed sn and pb perovskites enables broadening of absorption spectrum in solar cells," *Journal of the American Chemical Society*, vol. 136, pp. 8094–8099, 2014.

[77] N. J. Jeon, J. H. Noh, W. S. Yang, Y. C. Kim, S. Ryu, J. Seo, and S. I. Seok, "Compositional engineering of perovskite materials for high-performance solar cells," *Nature*, vol. 517, pp. 476–480, 2015.

[78] J. P. C. Baena, L. Steier, W. Tress, M. Saliba, S. Neutzner, T. Matsui, F. Giordano, T. J. Jacobsson, A. R. S. Kandada, S. M. Zakeeruddin, A. Petrozza, A. Abate, M. K. Nazeeruddin, M. Grätzel, and A. Hagfeldt, "Highly efficient planar perovskite solar cells through band alignment engineering," *Energy & Environmental Science*, vol. 8, pp. 2928–2934, 2015.

[79] W. S. Yang, B.-W. Park, E. H. Jung, N. J. Jeon, Y. C. Kim, D. U. Lee, S. S. Shin, J. Seo, E. K. Kim, J. H. Noh, and S. I. Seok, "Iodide management in formamidinium-lead-halide-based perovskite layers for efficient solar cells," *Science*, vol. 356, pp. 1376–1379, 2017.

[80] J. M. Frost, K. T. Butler, F. Brivio, C. H. Hendon, M. van Schilfgaarde, and A. Walsh, "Atomistic origins of high-performance in hybrid halide perovskite solar cells," *Nano Letters*, vol. 14, pp. 2584–2590, 2014.

[81] T. Baikie, Y. Fang, J. M. Kadro, M. Schreyer, F. Wei, S. G. Mhaisalkar, M. Grätzel, and T. J. White, "Synthesis and crystal chemistry of the hybrid perovskite $(CH_3NH_3)PbI_3$ for solid-state sensitised solar cell applications," *Journal of Materials Chemistry A*, vol. 1, pp. 5628–5641, 2013.

[82] W.-J. Yin, T. Shi, and Y. Yan, "Unusual defect physics in $CH_3NH_3PbI_3$ perovskite solar cell absorber," *Applied Physics Letters*, vol. 104, no. 063903, 2014.

[83] N.-G. Park, "Perovskite solar cells: an emerging photovoltaic technology," *Materials today*, vol. 18, no. 2, pp. 65–72, 2015.

[84] G. Kieslich, S. Sun, and A. K. Cheetham, "Solid-state principles applied to organic–inorganic perovskites: new tricks for an old dog," *Chemical Science*, vol. 5, no. 12, pp. 4712–4715, 2014.

[85] N. K. Noel, S. D. Stranks, A. Abate, C. Wehrenfennig, S. Guarnera, A.-A. Haghighirad, A. Sadhanala, G. E. Eperon, S. K. Pathak, M. B. Johnston, A. Petrozza, L. M. Herza, and H. J. Snaith, "Lead-free organic-inorganic tin halide perovskites for photovoltaic applications," *Energy & Environmental Science*, vol. 7, pp. 3061–3068, 2014.

[86] S. D. Stranks and H. J. Snaith, "Metal-halide perovskites for photovoltaic and light-emitting devices," *Nature Nanotechnology*, vol. 10, pp. 391–402, 2015.

[87] J. Burschka, N. Pellet, S.-J. Moon, R. Humphry-Baker, P. Gao, M. K. Nazeeruddin, and M. Grätzel, "Sequential deposition as a route to high-performance perovskite-sensitized solar cells," *Nature*, vol. 499, no. 7458, pp. 316–319, 2013.

[88] M. Saliba, T. Matsui, J.-Y. Seo, K. Domanski, J.-P. Correa-Baena, M. K. Nazeeruddin, S. M. Zakeeruddin, W. Tress, A. Abate, A. Hagfeldt, and M. Grätzel, "Cesium-containing triple cation perovskite solar cells improved stability, reproducibility and high efficiency," *Energy & Environmental Science*, vol. 9, pp. 1989–1997, 2016.

[89] M. Grätzel, "The light and shade of perovskite solar cells," *Nature Materials*, vol. 13, pp. 838–842, 2014.

[90] M. Saliba, T. Matsui, K. Domanski, J.-Y. Seo, A. Ummadisingu, S. M. Zakeeruddin, J.-P. Correa-Baena, W. R. Tress, A. Abate, A. Hagfeldt, and M. Grätzel, "Incorporation of rubidium cations into perovskite solar cells improves photovoltaic performance," *Science*, vol. 354, no. 6309, pp. 206–209, 2016.

[91] H.-S. Kim, C.-R. Lee, J.-H. Im, K.-B. Lee, T. Moehl, A. Marchioro, S.-J. Moon, R. Humphry-Baker, J.-H. Yum, J. E. Moser *et al.*, "Lead iodide perovskite sensitized all-solid-state submicron thin film mesoscopic solar cell with efficiency exceeding 9%," *Scientific reports*, vol. 2, no. 1, p. 591, 2012.

[92] A. Mei, X. Li, L. Liu, Z. Ku, T. Liu, Y. Rong, M. Xu, M. Hu, J. Chen, Y. Yang, M. Grätzel, and H. Han, "A hole-conductor-free, fully printable mesoscopic perovskite solar cell with high stability," *Science*, vol. 345, no. 6194, pp. 295–298, 2014.

[93] K. M. McCall, C. C. Stoumpos, O. Y. Kontsevoi, G. C. Alexander, B. W. Wessels, and M. G. Kanatzidis, "From 0d cs3bi2i9 to 2d cs3bi2i6cl3: dimensional expansion induces a direct band gap but enhances electron–phonon coupling," *Chemistry of Materials*, vol. 31, no. 7, pp. 2644–2650, 2019.

[94] B. Chabot and E. Parthe, "Cs3sb2i9 and cs3bi2i9 with the hexagonal cs3cr2cl9 structure type," *Acta Crystallographica Section B: Structural Crystallography and Crystal Chemistry*, vol. 34, no. 2, pp. 645–648, 1978.

[95] F. Lazarini, "Caesium enneabromodibismuthate (iii)," *Acta Crystallographica Section B: Structural Crystallography and Crystal Chemistry*, vol. 33, no. 9, pp. 2961–2964, 1977.

[96] A. J. Morris, R. J. Nicholls, C. J. Pickard, and J. R. Yates, "Optados: A tool for obtaining density of states, core-level and optical spectra from electronic structure codes," *Computer Physics Communications*, vol. 185, no. 5, pp. 1477–1485, 2014.

[97] E. Moshfeghi and M. H. Entezari, "Enhancement of the photovoltaic performance of perovskite solar cells via sono-synthesis of al-doped tio2 as the electron transport layer," *International Journal of Energy Research*, vol. 46, no. 15, pp. 23 465–23 479, 2022.

[98] J.-H. Im, I.-H. Jang, N. Pellet, M. Grätzel, and N.-G. Park, "Growth of ch3nh3pbi3 cuboids with controlled size for high-efficiency perovskite solar cells," *Nature nanotechnology*, vol. 9, no. 11, pp. 927–932, 2014.

[99] J. Qin, Z. Zhang, W. Shi, Y. Liu, H. Gao, and Y. Mao, "The optimum titanium precursor of fabricating tio2 compact layer for perovskite solar cells," *Nanoscale research letters*, vol. 12, no. 1, pp. 1–9, 2017.

[100] T. Singh, A. Kulkarni, M. Ikegami, and T. Miyasaka, "Effect of electron transporting layer on bismuth-based lead-free perovskite (ch3nh3) 3 bi2i9 for photovoltaic applications," *ACS applied materials & interfaces*, vol. 8, no. 23, pp. 14 542–14 547, 2016.

[101] P. Docampo, J. M. Ball, M. Darwich, G. E. Eperon, and H. J. Snaith, "Efficient organometal trihalide perovskite planar-heterojunction solar cells on flexible polymer substrates," *Nature communications*, vol. 4, no. 1, pp. 1–6, 2013.

[102] D. V. Bavykin, J. M. Friedrich, A. A. Lapkin, and F. C. Walsh, "Stability of aqueous suspensions of titanate nanotubes," *Chemistry of materials*, vol. 18, no. 5, pp. 1124–1129, 2006.

[103] L. Song, L. Cao, J. Li, W. Liu, F. Zhang, L. Zhu, and G. Su, "Lead titanate nanotubes synthesized via ion-exchange method: Characteristics and formation

mechanism," *Journal of Alloys and Compounds*, vol. 509, no. 20, pp. 6061–6066, 2011.

[104] Y. Chan Choi, S. W. Lee, H. J. Jo, D.-H. Kim, and S.-J. Sung, "Controlled growth of organic–inorganic hybrid ch3nh3pbi3 perovskite thin films from phase-controlled crystalline powders," *RSC advances*, 2016.

[105] Y. Deng, E. Peng, Y. Shao, Z. Xiao, Q. Dong, and J. Huang, "Scalable fabrication of efficient organolead trihalide perovskite solar cells with doctor-bladed active layers," *Energy & Environmental Science*, vol. 8, no. 5, pp. 1544–1550, 2015.

[106] S. F. Hoefler, G. Trimmel, and T. Rath, "Progress on lead-free metal halide perovskites for photovoltaic applications: a review," *Monatshefte für Chemie-Chemical Monthly*, vol. 148, pp. 795–826, 2017.

[107] B.-W. Park, B. Philippe, X. Zhang, H. Rensmo, G. Boschloo, and E. M. Johansson, "Bismuth based hybrid perovskites a3bi2i9 (a: methylammonium or cesium) for solar cell application," *Advanced materials*, vol. 27, no. 43, pp. 6806–6813, 2015.

[108] I. O. Ali, D. P. Joubert, and M. S. Suleiman, "First-principles calculations of the electronic and optical properties of ch3nh3pbi3 for photovoltaic applications," *Materials Today: Proceedings*, vol. 5, no. 4, pp. 10 570–10 576, 2018.

[109] S. Wang, J. Qiao, Y. Xu, X. Guo, and C. Nan, "First-principles study on ch3nh3pbi3 materials for perovskite solar cells," *Physica B: Condensed Matter*, vol. 550, pp. 347–353, 2018.

[110] N. M. Rahman, M. Adnaan, D. Adhikary, M. Islam, and M. K. Alam, "First-principles calculation of the optoelectronic properties of doped methylammonium lead halide perovskites: A dft-based study," *Computational Materials Science*, vol. 150, pp. 439–447, 2018.

[111] B. Saparov, F. Hong, J.-P. Sun, H.-S. Duan, W. Meng, S. Cameron, I. G. Hill, Y. Yan, and D. B. Mitzi, "Thin-film preparation and characterization of cs3sb2i9: a lead-free layered perovskite semiconductor," *Chemistry of Materials*, vol. 27, no. 16, pp. 5622–5632, 2015.

[112] B. Ghosh, S. Chakraborty, H. Wei, C. Guet, S. Li, S. Mhaisalkar, and N. Mathews, "Poor photovoltaic performance of cs3bi2i9: an insight through first-principles calculations," *The journal of physical chemistry C*, vol. 121, no. 32, pp. 17 062–17 067, 2017.

[113] K. M. McCall, C. C. Stoumpos, S. S. Kostina, M. G. Kanatzidis, and B. W. Wessels, "Strong electron–phonon coupling and self-trapped excitons in the defect halide perovskites a3m2i9 (a= cs, rb; m= bi, sb)," *Chemistry of Materials*, vol. 29, no. 9, pp. 4129–4145, 2017.

[114] A. J. Lehner, D. H. Fabini, H. A. Evans, C.-A. Hébert, S. R. Smock, J. Hu, H. Wang, J. W. Zwanziger, M. L. Chabinyc, and R. Seshadri, "Crystal and electronic structures of complex bismuth iodides a 3bi2i9 (a= k, rb, cs) related to perovskite: aiding the rational design of photovoltaics," *Chemistry of Materials*, vol. 27, no. 20, pp. 7137–7148, 2015.

[115] M. Belabbas, N. Marbouh, O. Arbouche, and A. Hussain, "Optoelectronic properties of the novel perovskite materials lipb (cl: Br: I) 3 for enhanced hydrogen production by visible photo-catalytic activity: Theoretical prediction based on empirical formulae and dft," *International Journal of Hydrogen Energy*, vol. 45, no. 58, pp. 33 466–33 477, 2020.

[116] C. Liu, Z. Wang, W. Xiong, H. Zhong, and S. Yuan, "Effect of vertical strain and in-plane biaxial strain on type-ii mosi2n4/cs3bi2i9 van der waals heterostructure," *Journal of Applied Physics*, vol. 131, no. 16, 2022.

[117] T. Van Mourik, M. Bühl, and M.-P. Gaigeot, "Density functional theory across chemistry, physics and biology," p. 20120488, 2014.

[118] S. Devasia, S. Shaji, D. A. Avellaneda, J. A. A. Martinez, and B. Krishnan, "In situ crystallization of 0d perovskite derivative cs3bi2i9 thin films via ultrasonic spray," *Journal of Alloys and Compounds*, vol. 893, p. 162294, 2022.

[119] K.-H. Hong, J. Kim, L. Debbichi, H. Kim, and S. H. Im, "Band gap engineering of cs3bi2i9 perovskites with trivalent atoms using a dual metal cation," *The Journal Of Physical Chemistry C*, vol. 121, no. 1, pp. 969–974, 2017.

[120] M. Pazoki, M. B. Johansson, H. Zhu, P. Broqvist, T. Edvinsson, G. Boschloo, and E. M. Johansson, "Bismuth iodide perovskite materials for solar cell applications: electronic structure, optical transitions, and directional charge transport," *The Journal of Physical Chemistry C*, vol. 120, no. 51, pp. 29 039–29 046, 2016.

[121] M. Shi, G. Li, W. Tian, S. Jin, X. Tao, Y. Jiang, E. A. Pidko, R. Li, and C. Li, "Understanding the effect of crystalline structural transformation for lead-free inorganic halide perovskites," *Advanced Materials*, vol. 32, no. 31, p. 2002137, 2020.

[122] C. J. Krajewska, S. R. Kavanagh, L. Zhang, D. J. Kubicki, K. Dey, K. Gałkowski, C. P. Grey, S. D. Stranks, A. Walsh, D. O. Scanlon *et al.*, "Enhanced visible light absorption in layered cs 3 bi 2 br 9 through mixed-valence sn (ii)/sn (iv) doping," *Chemical Science*, vol. 12, no. 44, pp. 14 686–14 699, 2021.

[123] J. Jin, L. N. Quan, M. Gao, C. Chen, P. Guo, and P. Yang, "Octahedral distortion and excitonic behavior of cs3bi2br9 halide perovskite at low temperature," *The Journal of Physical Chemistry C*, vol. 127, no. 7, pp. 3523–3531, 2023.

[124] J. H. Noh, S. H. Im, J. H. Heo, T. N. Mandal, and S. I. Seok, "Chemical management for colorful, efficient, and stable inorganic–organic hybrid nanostructured solar cells," *Nano letters*, vol. 13, no. 4, pp. 1764–1769, 2013.

[125] P. Makuła, M. Pacia, and W. Macyk, "How to correctly determine the band gap energy of modified semiconductor photocatalysts based on uv–vis spectra," pp. 6814–6817, 2018.

[126] B.-B. Yu, M. Liao, J. Yang, W. Chen, Y. Zhu, X. Zhang, T. Duan, W. Yao, S.-H. Wei, and Z. He, "Alloy-induced phase transition and enhanced photovoltaic performance: The case of cs 3 bi 2 i 9- x br x perovskite solar cells," *Journal of materials chemistry A*, vol. 7, no. 15, pp. 8818–8825, 2019.

[127] Y. Liu, Y. Gao, J. Zhi, R. Huang, W. Li, X. Huang, G. Yan, Z. Ji, and W. Mai, "All-inorganic lead-free nio x/cs3bi2br9 perovskite heterojunction photodetectors for ultraviolet multispectral imaging," *Nano Research*, vol. 15, no. 2, pp. 1094–1101, 2022.

[128] A. Tooghi, D. Fathi, and M. Eskandari, "High-performance perovskite solar cell using photonic–plasmonic nanostructure," *Scientific Reports*, vol. 10, no. 1, p. 11248, 2020.

[129] D. Liu, B.-B. Yu, M. Liao, Z. Jin, L. Zhou, X. Zhang, F. Wang, H. He, T. Gatti, and Z. He, "Self-powered and broadband lead-free inorganic perovskite photodetector with high stability," *ACS applied materials & interfaces*, vol. 12, no. 27, pp. 30 530–30 537, 2020.

[130] S. Bonomi, P. Galinetto, M. Patrini, L. Romani, and L. Malavasi, "Optical and structural property tuning in physical vapor deposited bismuth halides cs3bi2 (i1–x br x) 9 (0 x 1)," *Inorganic Chemistry*, vol. 60, no. 18, pp. 14 142–14 150, 2021.

[131] J. Y. Kim, J.-W. Lee, H. S. Jung, H. Shin, and N.-G. Park, "High-efficiency perovskite solar cells," *Chemical Reviews*, vol. 120, no. 15, pp. 7867–7918, 2020.

[132] A. M. Elseman, A. H. Zaki, A. E. Shalan, M. M. Rashad, and Q. L. Song, "Tio2 nanotubes: an advanced electron transport material for enhancing the efficiency and stability of perovskite solar cells," *Industrial & Engineering Chemistry Research*, vol. 59, no. 41, pp. 18 549–18 557, 2020.

[133] D. Wang, M. Wright, N. K. Elumalai, and A. Uddin, "Stability of perovskite solar cells," *Solar Energy Materials and Solar Cells*, vol. 147, pp. 255–275, 2016.

[134] A. Merdasa, A. Kiligaridis, C. Rehermann, M. Abdi-Jalebi, J. Stober, B. Louis, M. Gerhard, S. D. Stranks, E. L. Unger, and I. G. Scheblykin, "Impact of excess lead iodide on the recombination kinetics in metal halide perovskites," *ACS Energy Letters*, vol. 4, no. 6, pp. 1370–1378, 2019.

[135] Z. Song, S. C. Watthage, A. B. Phillips, B. L. Tompkins, R. J. Ellingson, and M. J. Heben, "Impact of processing temperature and composition on the formation of methylammonium lead iodide perovskites," *Chemistry of Materials*, vol. 27, no. 13, pp. 4612–4619, 2015.

[136] B. Slimi, M. Mollar, I. B. Assaker, I. Kriaa, R. Chtourou, and B. Marí, "Perovskite fa1-xmaxpbi3 for solar cells: films formation and properties," *Energy Procedia*, vol. 102, pp. 87–95, 2016.

[137] S. U. Rege and R. T. Yang, "A novel ftir method for studying mixed gas adsorption at low concentrations: H2o and co2 on nax zeolite and γ-alumina," *Chemical engineering science*, vol. 56, no. 12, pp. 3781–3796, 2001.

[138] F. Sahli, N. Miaz, N. Salsi, C. Bucher, A. Schafflutzel, Q. Guesnay, L. Duchêne, B. Niesen, C. Ballif, and Q. Jeangros, "Vapor transport deposition of methylammonium iodide for perovskite solar cells," *ACS Applied Energy Materials*, vol. 4, no. 5, pp. 4333–4343, 2021.

[139] Y. Yang, T. Chen, D. Pan, J. Gao, C. Zhu, F. Lin, C. Zhou, Q. Tai, S. Xiao, Y. Yuan *et al.*, "Mapbi3/agarose photoactive composite for highly stable unencapsulated perovskite solar cells in humid environment," *Nano Energy*, vol. 67, p. 104246, 2020.